Doctoral Thesis

μ-PIC gaseous area detector for small-angle X-ray scattering experiments

Kaori Hattori

Department of Physics, Graduate School of Science, Kyoto University
January, 2009

Abstract

A detector with such properties, a two-dimensional counting detector based on a micro-pixel gas chamber (μ-PIC), is described.

Small-angle X-ray scattering (SAXS) is useful for investigating structures on a scale of 1-100 nm. It has a wide range of applications in biology, material science, and the study of soft condensed matter. The SAXS measurements are becoming increasingly popular in this field. The narrow dynamic range of the imaging detectors currently in use has limited the resolution of many experiments. Now integrated-type area detectors, Imaging plates (IPs) and CCDs, are widely used. Due to internal noise, the accuracy of these detectors are limited. Therefore, a new detector that provides high-resolution measurements is desired. In theory, photon-counting type detectors is free from the internal noise and its accuracy is limited by only statistical error. Therefore, they would attain higher resolution than the integrated-type detectors. Then, the photon-counting type detectors would be able to measure low-intensity scattering and widen the application field.

The application of the μ-PIC detector to high-resolution SAXS, its performance, and refinements of the detector system, are reported. We have developed the X-ray area detector based on the μ-PIC , which is a photon-counting type detector. The μ-PIC is a micro-pattern gaseous detector with a pitch of 400 μm fabricated by printed circuit board technology. In the present work, a μ-PIC with an active area of 100×100 mm was used. To reduce the number of channels, a strip readout is used and a position encoding system reconstructs the positions of incident X-rays. The μ-PIC has only 256×2 channels readout though it has 256×256 pixels ($= 6.6 \times 10^4$). This paper will focus on refinements of the position encoding system because it plays a key role in the high-resolution SAXS experiments.

With the refined encoding system, solution scattering experiments were carried out. The performance was investigated at the RIKEN structural biology beamline (BL45XU-SAXS station) at SPring-8, Japan. We successfully showed that a solute scattering curve maintained linearity in a range of $> 10^6$. This range is wider by an order of magnitude than that observed by the IPs and the widest one achieved by X-ray area detectors. The wide dynamic range is essential to observe weak scattering and enhance the resolution of measurements. In this way, we showed that the μ-PIC detector has an ability to perform the high-resolution SAXS measurements. We also showed that the position resolution was enhanced using charges. The position resolution was refined and was $\sigma = 93.6$ μm. Scattering curves observed by the new μ-PIC system and an imaging plate agreed well. The pixel pitch of the IP was 100 μm.

The improved position encoding system was applied to a Compton camera that consists of a Time Projection Chamber (TPC) read by the μ-PIC and scintillators surrounding the TPC. Then, three-dimensional fine tracks of cosmic muons and Compton-recoil electrons generated by 662 keV gamma-ray were observed within the TPC. The new encoding system doubled the hits of these tracks. Using charges generated by recoil electrons, the system is expected to provide a stronger criterion used for determining Compton-scattered points than that currently used. Then, the angular resolution of the camera would be enhanced.

This μ-PIC area detector also functions as a thermal neutron imaging detector. The μ-PIC detector successfully measured small-angle neutron scattering (SANS) and observed a Bragg peak. Using a knife edge test, a fine position resolution of < 1 mm was obtained while conventional detectors used for thermal neutron scattering have a position resolution of a few mm.

Contents

Chapter 1

Introduction

Nowadays, X-ray scattering is widely used to investigate a wide range of substances, such as crystals, industrial materials, and biological macromolecules.

1.1 Principles of X-ray scattering

In this section, we will treat the principles of pure elastic scattering by a sample [1]. We consider the scattering of a plane monochromatic wave of X-rays. Once electrons in the sample interact with the X-rays, they generate secondary spherical waves. Figure 1.1 shows a schematic view of the scattering.

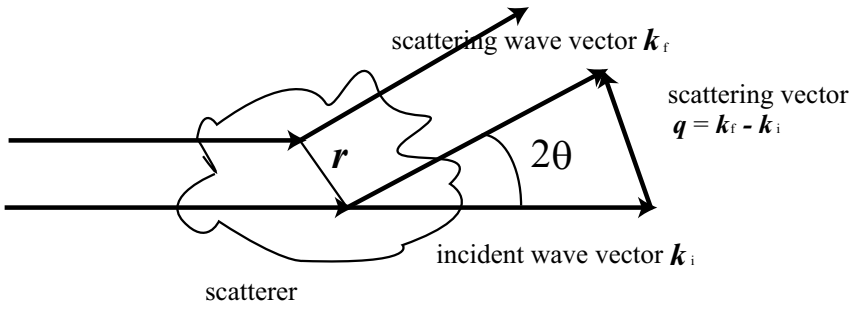

Figure 1.1: Schematic view of X-ray scattering.

The phase difference of the secondary wave is represented by $\boldsymbol{r} \cdot \boldsymbol{q}$ as a function of a position, $\boldsymbol{r}$, where $\boldsymbol{q} = \boldsymbol{k}_\mathrm{f} - \boldsymbol{k}_\mathrm{i}$ and $\boldsymbol{k}_\mathrm{i}$ and $\boldsymbol{k}_\mathrm{f}$ are the incident and scattering wave vectors with $|\boldsymbol{k}_\mathrm{i}| = |\boldsymbol{k}_\mathrm{f}| = 2\pi/\lambda$, λ denoting the wavelength. The resultant scattering wave is a superposition of scattering waves generated by the sample whose electron density is given by $\rho(\boldsymbol{r})$. Then the scattering is represented by

$$F(\boldsymbol{q}) = \int_V \rho(\boldsymbol{r}) \exp(-i\boldsymbol{q} \cdot \boldsymbol{r}) \mathrm{d}\boldsymbol{r}, \tag{1.1}$$

$F(\boldsymbol{q})$ is called a structure factor. A scattering intensity generated by the sample per volume unit $I(\boldsymbol{q})$ is given by

$$I(\boldsymbol{q}) = \frac{F(\boldsymbol{q}) F^*(\boldsymbol{q})}{V}. \tag{1.2}$$

The scattering intensity may be rewritten in the form

$$I(\boldsymbol{q}) = \int_V \gamma(\boldsymbol{r}) \exp(-\boldsymbol{q} \cdot \boldsymbol{r}) \mathrm{d}\boldsymbol{r}, \tag{1.3}$$

where

$$\gamma(\boldsymbol{r}) = \frac{1}{V}\int_V \rho(\boldsymbol{r}')\rho(\boldsymbol{r}+\boldsymbol{r}')\mathrm{d}\boldsymbol{r}'. \tag{1.4}$$

Expression (1.3) represents a Fourier transform of $\gamma(\boldsymbol{r})$ that is a self-correlation function of the electron density $\rho(\boldsymbol{r})$. In a case of an isotropic sample, equation (1.3) is given by

$$I(\boldsymbol{q}) = \int_0^\infty 4\pi r^2\gamma(r)\frac{\sin qr}{qr}\mathrm{d}\boldsymbol{r}. \tag{1.5}$$

1.2 Small-angle X-ray scattering (SAXS)

The "small-angle X-ray scattering" (SAXS) method is applied to disordering objects [2]. The diffraction pattern is diminishing as objects are disordered. The scale of the structure in the low-ordered samples is much larger than crystals. Thus, it is sufficient for low-ordered samples to observe a central part of the diffraction pattern. This leads to the SAXS method, which is useful to study low-ordered samples.

To obtain enough information on the inhomogeneities with a typical size D, the measurements of the scattering curve up to approximately $q = 1/D$ is required, where $q = 4\pi\sin\theta/\lambda$. The size of 1-100 nm corresponds to the angular region up to $2\theta = 0.8 - 8$ degrees at wavelength $\lambda = 1.54$ Å (the X-ray Cu K_α line). SAXS is a promising tool for investigating such structural scales, especially for determining the shape and size distribution of the particles, and the electron density fluctuation of the system. The fields investigated successfully by this method are biology and material science. Recently, studies of soft condensed matter using this method has been popular. Thus, various characteristics of disperse systems can be studied with small-angle scattering techniques.

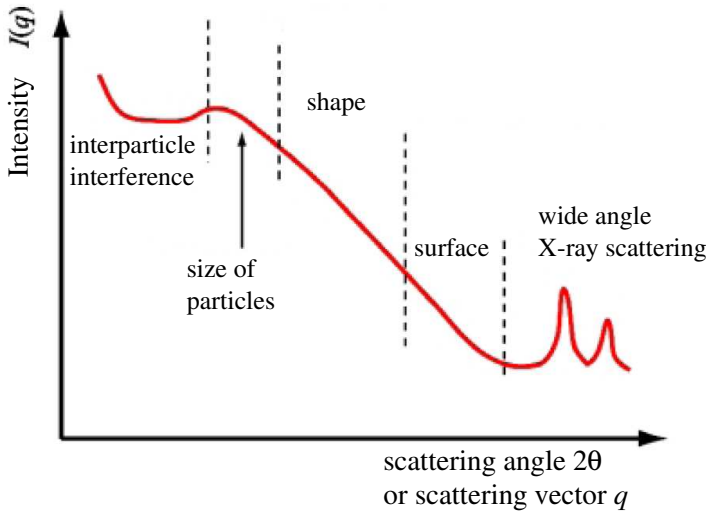

Figure 1.2: Typical information on particle sample in small angular region

1.2.1 Small-angle scattering curves

We now consider the behavior of the intensity of scattering, $I(q)$ as shown in Fig.1.2.

Guinier plot

In the vicinity of $q = 0$,

$$\frac{\sin qr}{qr} = 1 - \frac{q^2r^2}{3!} + \frac{q^4r^4}{5!} - \cdots. \tag{1.6}$$

Then, equation (1.5) is given by

$$\ln I(q) = \ln I(0) - \frac{1}{3}R_g^2 q^2, \tag{1.7}$$

where R_g is the radius of gyration expressed by

$$R_g^2 = \frac{\int_0^\infty r^2\rho(r)\mathrm{d}r}{\int_0^\infty \rho(r)\mathrm{d}r}. \tag{1.8}$$

Since the scattering intensity is proportional to q^2 in the vicinity of $q = 0$, R_g can be determined from the $\ln I(q)$ vs q^2 plot (the Guinier plot). Guinier approximation neglects higher order of qR_g. Therefore, it is valid mainly in the interval $qR_g < 1$. A sphere of radius D is determined by the equation of $R_g = \sqrt{\frac{3}{5}}D$.

Shape of particles

In the angular region of $qR_g >> 1$, the scattering intensity depends on the shape of the particles. To simplify calculations, we deal with scattering from spheres of radius D. We assume that the electron density in the sphere is constant and the density of spheres is low. Then the intensity is given by

$$I(q) = \frac{4\pi}{q}\int_0^D r\gamma(r)\sin(qr)\mathrm{d}r. \tag{1.9}$$

$\gamma(D)$ is equal to 0 due to the low density and $\rho(\boldsymbol{r}+D\boldsymbol{e})$ where $\boldsymbol{e}$ is a unit vector. The derivative of $\gamma(D)$ is also equal to 0 at $r = D$. Considering them, we perform integration by parts twice and obtain

$$I(q) = \frac{4\pi}{q^3}\int_0^D [r\gamma(r)]''\sin(qr)\mathrm{d}r. \tag{1.10}$$

This may be rewritten in the form

$$I(q) = \frac{4\pi}{q^4}(-2\gamma'(0) + cos(qD)D\gamma''(D) - \int_0^D [r\gamma(r)]'''\cos(qr)\mathrm{d}r). \tag{1.11}$$

The third term tends to 0 as q tends to infinity. In general, γ'' is 0 and the second term can be neglected. Therefore, only the first term contributes to the intensity in the angular region of $qR_g >> 1$. It can be concluded that the scattering intensity of spherical particles are proportional to q^{-4}. The scattering intensities of rod-like particles and lamellar particles, are proportional to q^{-1}, q^{-2}, respectively, which are valid around $q = 1/D$.

The Porod law

Considering the behavior of $I(q)$ as q tends to infinity, the asymptotic trend of $I(q)$ is proportional to q^{-4}

$$\lim_{q\to\infty} I(q) \propto \frac{1}{q^4}\frac{S}{V}, \tag{1.12}$$

where V and S are a volume and a surface area of scatterers, respectively. Thus a specific surface area S/V can be obtained. This law known as the Porod law holds only in the case of particles for which the scattering density distribution is a continuous smooth function.

1.2.2 Requirements for X-ray detectors

Thus the scattering intensity frequently changes by several orders of magnitude within a narrow range of values of q. This suggests that a wide dynamic range of the intensity is essential for detectors of the scattering radiation. This also implies necessity of high-angle resolution in the study of disperse systems. Since the range of a camera length that is a distance between a sample and the detector is constrained by instrumentation, the spatial resolution of the detectors should be high (< 100 μm). The large active area is a supplementary advantage for the high-angle region. It should be noted that stability operation for a long duration and under intense X-ray radiation is also crucial for detectors intended for synchrotron radiation.

1.2.3 Solution scattering

SAXS measurements is also a powerful tool to study solution scattering, which allows the determination of the structure of objects under investigation without crystallization. Since many biological samples dissolve in solvent, measurements of solution scattering is an ideal method to investigate their nature. Moreover, it takes a long duration, sometimes several years, to achieve crystal growth. Thus the ability to make measurements without crystallization is very helpful.

For application to the solution scattering, there are more strict requirements for X-ray detectors than those mentioned above. To obtain a solution scattering curve, one should measure the scattering pattern of solvent and solution. The scattering from the solution includes the background and the scattering from solvent. Therefore, the scattering from the solute can be determined by subtracting the solvent scattering curve from the solution curve. This is a general method for investigating SAXS.

The local counting rate with the solution scattering is sometimes about 100 times higher than that with the solvent only. Thus, it is crucial for the detectors to respond proportional to incoming photons in a wide range. From now we refer the proportionality as linearity. In addition, the difference of the scattering curve between the solution and the solvent is usually very small at wide scattering angles. To obtain the solute curve with a wide dynamic range, correct measurements of this small difference is essential. For this reason, solution scattering measurements are one of the most difficult method for structure determination. This fact implies that once a detector attains successful results in solution scattering measurements, it can be applied to almost all fields of X-ray structure determination.

1.3 X-ray detectors for SAXS techniques

These days there are a great number of models and devices used for small-angle scattering studies. In this section, features of several detectors are summarized. Basically, detectors of the scattering radiation are classified into two categories: counting and integration-type detectors.

In the early 80s, position-sensitive gas proportional counters (PSPC) were used for SAXS experiments in most synchrotron radiation facilities and laboratories. The PSPC is a one-dimensional photon-counting-type gaseous detector. Its counting rate was limited to $10^4 - 10^5$ counts per second, which is limited by the speed of its electronics. Third-generation synchrotron radiation sources have been available since the mid-90s, and the use of high-intensity and high-brilliance X-ray beams has begun. Most counting-type detectors have no tolerance for operating under such conditions.

Gaseous detectors have also been employed as a two-dimensional X-ray position encoding instrument ([3] and the references therein). A classical example can be observed in X-ray protein crystallography, wherein two-dimensional multi-wire proportional counters (MWPC) were being used in many synchrotron radiation facilities in the 1980s [4]. However, limitations in counting rates and position resolutions prevented their further usage in this field.

To satisfy requirements in third-generation synchrotron radiation sources, an imaging plate [5] and Charge-coupled device (CCD)-based area X-ray detectors [6] [7] have found wide use as an

integration-type X-ray detector for SAXS experiments and macromolecular crystallography. They are free from counting limitations due to electronics and are thus suitable for radiation with intense X-rays. Overviews of the CCD-detectors are also given in [8].

However, an integration-type X-ray detector has an intrinsic limitation in the signal-to-noise ratio of its data caused by internal noise such as readout noise and dark current in the CCD, except for quantum fluctuation of the signal. Another disadvantage of the detectors is low time resolution given in Tab. 1.1. Time-resolved measurements allow one to reveal dynamics of materials. Some kinds of experiments can be repeated and then its accuracy could be enhanced. The detail of the time-resolved measurements will be described in the subsequent chapter.

From the experimantal requirements, photon-counting-type detectors such as gaseous detectors and silicon pixel detectors have been developed. They have dramatically improved the signal-to-noise ratio and the time resolution.

A novel photon counting area detector, the micro strip gas chamber (MSGC) [9] [10], with a fine position resolution of 100 μm was being studied. Recently, novel gaseous detectors such as MICROMEGAS [11] and RAPID [12] [13] have been developed, and have helped meet the challenges of crystallography in high X-ray flux environments. Also, another type of photon counting area detector, silicon pixel detectors have proved stable operation under radiation with intense X-rays.

Now we treat with an imaging plate and and CCD detectors which are integration-type detectors. We also deal with two counting-type gaseous detectors, the RAPID and the MSGC, and a counting-type silicon detector, the PILATUS [14]. The features of the detectors are summarized in Table 1.1. In general, the maximum count of each pixel is limited by the size of the counters. Therefore, a dynamic range often refers to the maximum count. In this paper, a dynamic range represents a range where a linearity in the detector response is confirmed.

1.3.1 Imaging Plate (IP)

The imaging plates are integration-type detectors. They are similar to photographic film but they have replaced conventional X-ray film in most laboratories because of their advantages. They are at least 10 times more sensitive than X-ray film. The dynamic range of the IPs is much wider (10^{5-6}) while the X-ray film has a narrow dynamic range of 10^2.

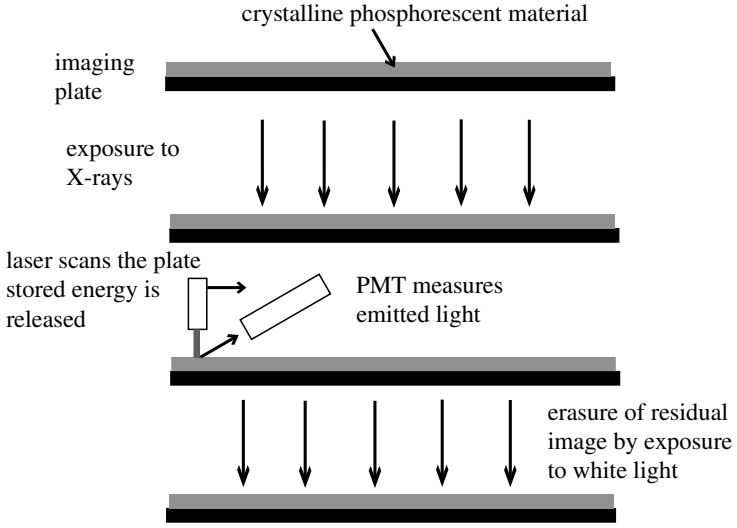

Figure 1.3: Principle of the imaging plate.

The IPs have a thin layer of an photostimulable phosphor, BaF(Br,I):E^{2+}, where X-rays are absorbed. The principle of the imaging plate is shown in Fig.1.3. X-rays excite electrons in the phosphor to higher energy levels. The excited electrons emit light in the visible wavelength region very soon as normal fluorescent. However, the part of the energy is stored in the phosphor by electrons trapped in color centers. It is emitted only slowly for the duration of more than several days. This stored energy is released when light is illuminated. Mainly a red laser is employed for scanning the phosphor and the stored energy is released as blue light. The red light is removed by a filter and the blue light is observed with a photomultiplier (PMT). The number of the emitted photons is proportional to that of absorbed X-ray photons. The spatial resolution mainly depends on the reading system.

Table 1.1: Summary of X-ray area detectors

Parameter	**Imaging Plate**	**X-ray Image Intensifier / CCD**	**fiber optic taper / CCD**	**PILATUS**
Type	integrated	integrated	integrated	photon counting
Absorber	phosphor	phosphor	phosphor	silicon
Spatial Resolution	50-200 μm	$\sim$100 μm	$\sim$100 μm	172 μm
Max. counting Rates (local)	10^8cps/mm^2	10^{6-7}cps/mm^2	10^8cps/mm^2	5×10^6cps/mm^2
Dynamic Range	10^{5-6}	10^{3-4}	10^{3-4}	10^6
Dynamic Range (for solute scattering)	$> 10^6$	10^{3-4}	10^{3-4}	no data
Time Resolution	$>$ a few 100 ms	$>$ 1 ms	$>$1 ms	10 ms

Parameter	**RAPID**	**MSGC**	**μ-PIC**
Type	photon counting	photon counting	photon counting
Absorber	gas	gas	gas
Spatial Resolution	375 μm (FWHM)	100 μm	220 μm (FWHM)
Max. counting Rates (local)	10^6cps/mm^2	10^7cps/mm^2	10^7cps/mm^2
Dynamic Range	infinite	infinite	infinite
Dynamic Range (for solute scattering)	no data	10^6	$> 10^6$
Time Resolution	100 ns	$>$20 ns	$>$10 ns

At present, the pixel size of 50 - 200 μm is available. After reading which takes a few minutes the plates need to be erased by exposure to intense white light. Then, the plates can be reused. Therefore, the imaging plates are favorable for measurements of static objects. However, it is not suitable for continuous operations and time resolved experiments.

1.3.2 Charge-coupled device (CCD)-based area detectors

Another integrated-type detector found wide use is a CCD-based detector. The CCD detectors consist of components such as phosphors, fiber optics, image intensifiers and a CCD. Figure 1.4 shows typical CCD detector systems. Incident X-rays are converted to visible light by phosphors and then transmitted through fiber optics, occasionally amplified by the intensifiers. The positions are recorded by the CCDs.

The CCDs are directly sensitive to X-rays and applied to astrophysics. However, the effective area of available CCDs are too small. The CCDs are suffered from radiation damage, and have too low X-ray stopping power. Therefore a phosphor screen is employed to absorb the X-rays in large area and coupled to a CCD. To enhance a position resolution, the screen of long, thin, optically isolated columns of luminescent material has been fabricated as shown in Fig.1.5. The phosphor columns are deposited on fiber optics which transform scintillation light to an adjacent component.

Since the area of the phosphor screen is larger than that of the CCD, demagnification of phosphor image is done by a fiber-optic taper or an image intensifier.

fiber-optic taper/CCD

A fused fiber-optic bundle consisting of a coherent bundle of glass-fiber light guides is often used because of easy-handling. Photons from the phosphor screen are collected through the bundle and thus the image can be demagnified. A distortion and a non-uniformity are always found in the demagnified image and lead to necessity for corrections.

Image intensifier/CCD

The system is schematically represented in Fig.1.4. In this detector, the incident X-rays are collected on a fluorescent screen. X-ray photons are transformed into visible photons by CsI located on the screen. Then the visible photons are transformed into electrons by photo cathodes. The resultant electrons are accelerated by the electric field applied in an image intensifier and end with another fluorescent screen. The amount of photons emitted at the fluorescent screen is proportional to the energy of the incident electron. Therefore the accelerated electrons produces more photons than primary photons generated in the phosphor screen. The amplified photons are registered into the CCD.

In a case of a large demagnification ratio, number of photons registered to the CCD is low, and thus intensification is useful. Since the intensifiers are expensive and fragile, the use should be avoided whenever possible. The introduction of low noise CCDs decreases necessity of the image intensifiers.

The cooled CCDs with low noise and low-time resolution are used for measurements of static objects. On the other hand, the CCDs of high noise and high frame rates are used for time resolved measurements. Even in the case of the cooled CCDs, readout noise contributes to their narrow dynamic range of 10^{3-4}.

Some CCDs designed for the operation at high frame rates have two kinds of pixels: normal pixels and shaded pixels. After one frame exposure, charge accumulated in the normal pixels is transformed to the shaded pixels. The charge in the shaded pixels is registered during the next frame. In this method, all pixels should be read within a frame. Therefore, it restricts the time resolution of the detector, which has reached 1 msec.

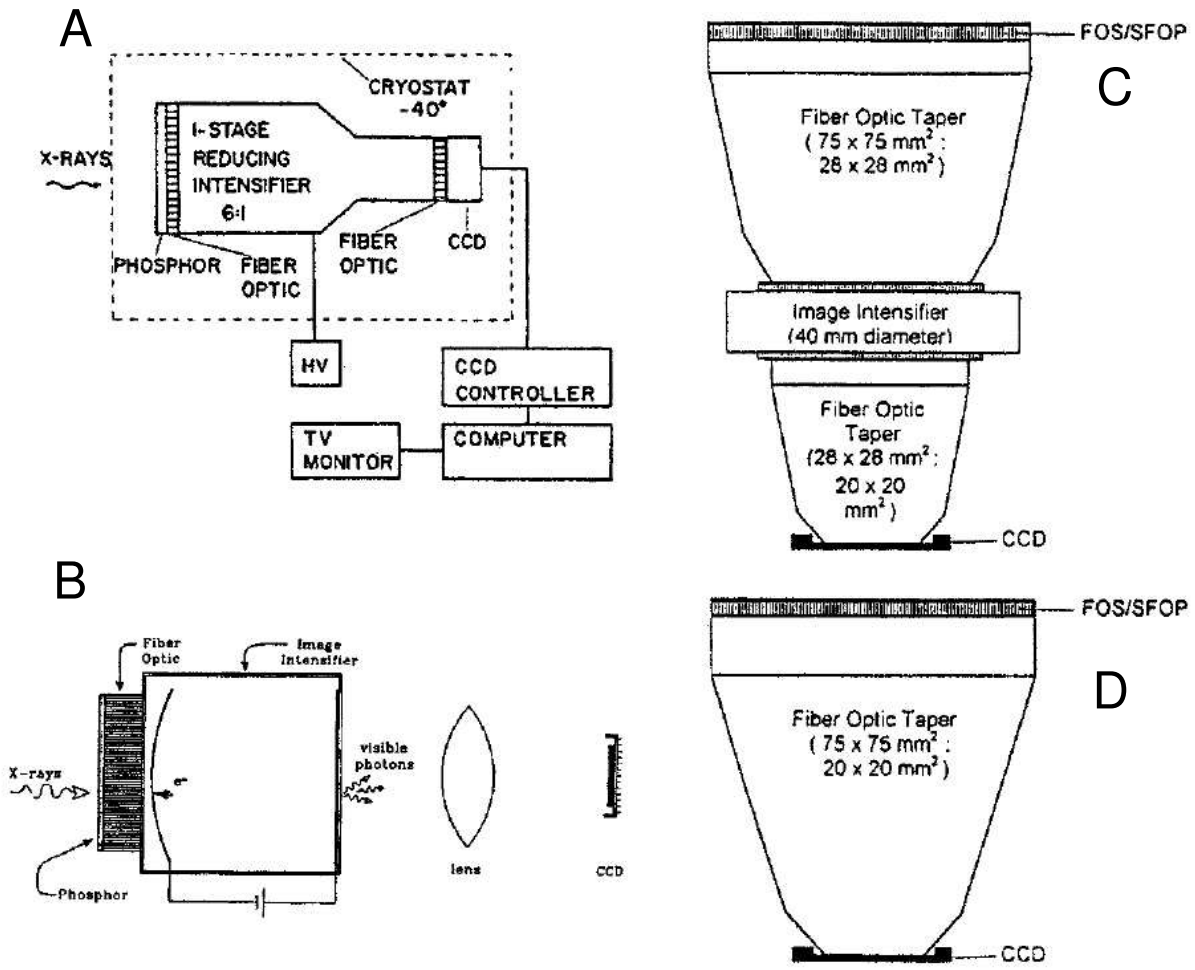

Figure 1.4: Schematics of CCD detectors [8]. (A) Combination of phosphor screen, an image intensifier, and CCD; (B) Combination of phosphor screen, an image intensifier, and a lens coupled to a CCD; (C) Combination of phosphor or scintillating fiber-optics screen, a fiber-optic taper, an image intensifier, a second taper and the CCD; (D) Combination of phosphor or scintillating fiber-optics screen, a fiber-optic taper and the CCD.

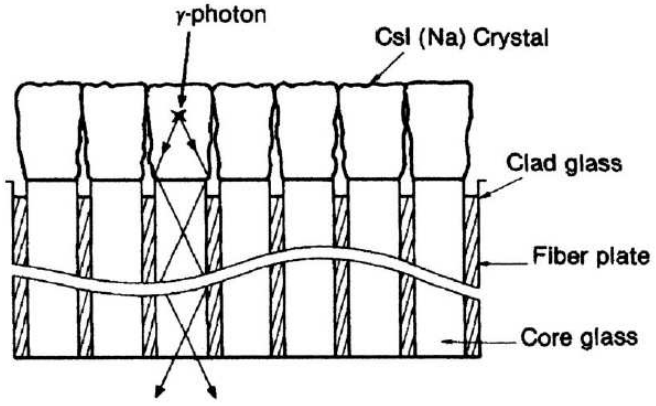

Figure 1.5: Schematic of CsI(Na) phosphor columns grown on an fiber-optic plate [8].

1.3.3 Silicon pixel detector (PILATUS)

The PILATUS detector (pixel apparatus for the SLS) is another type of photon counting detectors. It is a silicon pixel array detector based on the CMOS hybrid pixel technology. Figure 1.6 shows a schematic of the silicon pixel array detector. Figure 1.7 (a) displays a side view of the PILATUS detector. In the semiconductor sensor, incident X-rays liberate electrons and the electrons generate many electron-hole pairs along their track. The charge is transferred to the ASIC CMOS chips via a small indium bump bond shown in Fig. 1.7(c). Each pixel comprises a preamplifier, a comparator and a counter. In the sensor, X-rays are transformed to charge enforced by the preamplifiers. The comparator generates a digital signal if the charge exceeds a threshold. The detector equips counters where number of digital signals per pixel is stored. The maximum count of this detector is 10^6, which is determined by the 20-bit counters. The maximum counting rate is 1.5 MHz/pixel/s. As shown in Fig. 1.7 (b), the counter occupies most of the pixel area.

This readout method is free from readout noise and dark current. The readout time is 3 ms and the frame rate ranges from 10 Hz to 100 Hz. During the readout, the detector is insensitive to incident X-rays. It is a disadvantage to time resolved measurements and continuous measurements. Main advantage of the silicon detectors is a high quantum efficiency. The efficiency attains 50 % even at 16 keV while that of gaseous detectors falls rapidly in such high energy region. Another advantage is a good spatial resolution determined by the pixel size of 0.172 mm.

At present, three kinds of PILATUS detector systems have been developed, the PILATUS 100K, 1M, and 6M. The PILATUS 100K detector is a single module consisting of 487 x 195 pixels. The active area is over $84\times34\text{mm}^2$. The PILATUS 2M detector consists of 3×7 modules with 1475×1467 pixels. The total active area is $254\times252\text{mm}^2$. The PILATUS 6M detector consists of 5×12 modules with 2463×2527 pixels. The total active area is $424 \times 435\text{mm}^2$. The detector has attained many advantages in comparison with the integrated-type X-ray area detectors. However, the cost of the PILATUS is unrealistic for uses at a laboratory. Thus a photon counting detector with reasonable cost is eagerly awaited. This requirement leads to a detector with a simpler structure and readout.

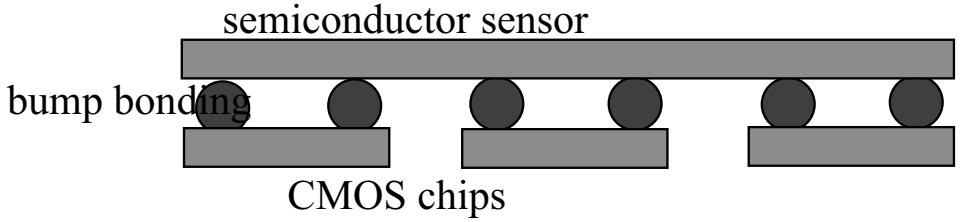

Figure 1.6: Schematic of a silicon pixel array detector.

1.3.4 Refined ADC Per Input Detector system (RAPID)

The RAPID detector is one of photon counting-type detectors. It consits of a fine-pitch MWPC and a multi-channel readout system. The MWPC has 256×256 anode wires with a pitch of 750 μm. An anode to cathode gap is 500 μm as illustrated in Fig.1.8. The RAPID used the narrow-anode to cathode gap to overcome the space charge effects in wire chambers which limits the local counting rates. This enhances the local counting rates in the RAPID detector to approximately 10^6 photons/mm^2/s. The local rate of the delay line readout MWPCs were limited to 3×10^3 counts s^{-1} mm $^{-2}$ and the global rate to 10^6 counts s^{-1} [16].

When an incident X-ray liberates an electron trapped by a gas atom, the liberated electron causes the formation of clouds of ions and electrons in the gas. The electron clouds drift toward the anode wires along an electric field applied across the gas volume. Then amplification is applied by accelerating the electron clouds in an electric field around the anode wires. The resultant electrons

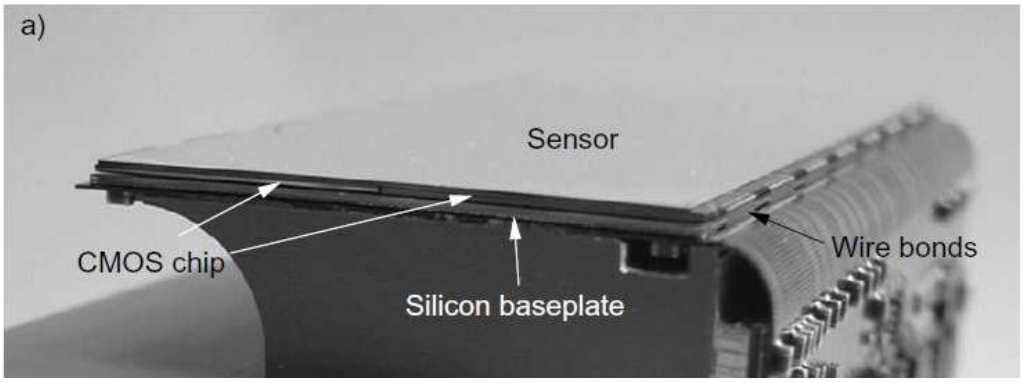

(a) Side view of the PILATUS detector.

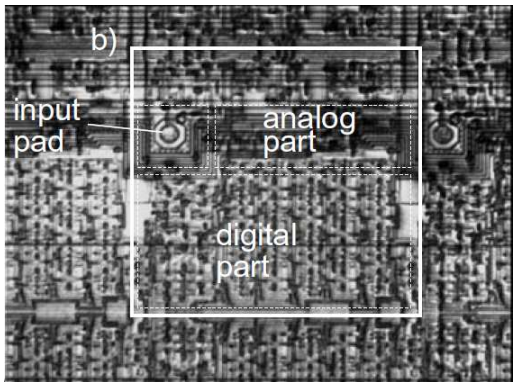

(b) Magnification of a single pixel. A bump pad is next to the analog part. A digital counter occupies most of the pixel area.

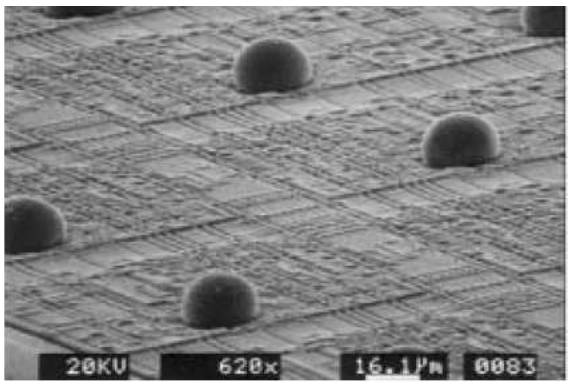

(c) Each silicon pixel sensor is electrically connected to a readout chip via a small indium bump bond.

Figure 1.7: The PILATUS detector [15].

are collected by the anode wires. Ions formed through the amplification are collected by the cathode placed below the anode wires. Since there is no material absorbing ions between the anode wires and the window, ion feedback could be observed. Therefore, signals from the anode wires and cathode wires should coincide. The signals in coincidence allows interpolation of two-dimensional position of the incident X-ray.

Each wire of the detector is instrumented with a preamplifier and an Analogue to Digital Converter (ADC). The ADCs collect the signals from the most closet four channels surrounding an incident X-ray. Then calculation of the position of the event is performed independently in X and Y and the two co-ordinates combined to reconstruct the position of the X-ray. The number of pixels is 1024×1024 in typical use. The resulting position, the charge/energy value, and time are stored in a histogramming memory. The spatial resolution of 384 μm is better than the pixel pitch because of position interpolation. The readout is a complex and huge system. The fast ADC and the position interpolation system are need to be operated with cooling water.

The photon-counting detectors including the RAPID is free from noise accompanied by readout. This outstanding feature of the photon-counting detectors provides repeated measurements. Then, low-intensity signals can be detected as the result of the sum of data. The disadvantage of the RAPID is a low tolerance for high-counting rate environments. The RAPID can detect all X-rays at 20 MHz when the distribution of the incident X-rays are approximately uniform. However, localized incident X-rays (1 MHz/mm^2) causes the counting loss even if the global counting rates are less than 20 MHz. The RAPID has not been easy to handle and thus further improvements are necessary. For common use, performance characteristics of detectors must be the same. However, wire chambers with the same design often show different performance. The RAPID using wires has the same feature that prevents the RAPID from wide spread.

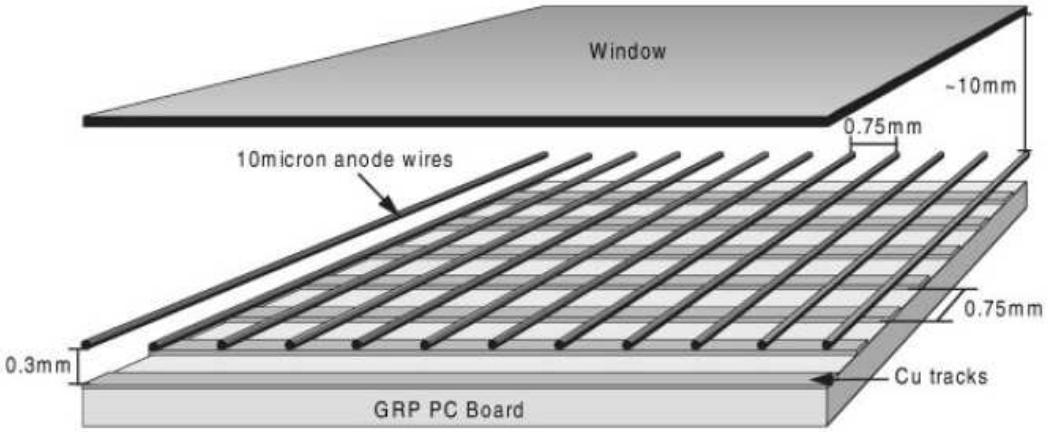

Figure 1.8: Schematic of the 2D micro-gap detector

1.3.5 Micro Stip Gas Chamber (MSGC)

The MSGC shown in Fig.1.9 is designed from the basis of the MWPC. The structure of the MSGC is similar to the RAPID while the MSGC has thin conductor strips printed on a substrate. The potential of the anode is positive relative to the two adjacent cathode strips. The pitches of anodes and cathodes are 200 μm, respectively. The narrowly spaced strips prevent the space charge effects seen in wire chambers. To yield two-dimensional images backstrips with a 200 μm pitch are arranged on the opposite side of the 20-μm thick substrate. Each strip is instrumented with an amplifier and

a discriminator. The discriminated signals are used for calculation of the position of an incident X-ray.

The MSGC features a fine spatial resolution in comparison with the RAPID. The spatial resolution was 50 μm using ADCs, similar to the RAPID. Without the ADCs, it was 100 μm. A solute scattering curve determined by subtracting the solution curve from the solution curve attained a good linearity in the wide range of 10^6 [17]. Thus, the MSGC has proved the advantages of photon-counting detectors. However, operation at a sufficient gas gain of $> 10^3$ causes discharges between the anodes and the cathodes. It is impossible to apply a high voltage to the MSGC once it was damaged by serious discharges. To solve this problem, a preamplifier such as a capillary plate [18] and a Gas Electron Multiplier (GEM) [19] has been installed above the MSGC. However, the instability problem has not solved yet. Therefore the need of a new gaseous photon counting detector with a good position resolution, a wide dynamic range and a stable operation has been arisen.

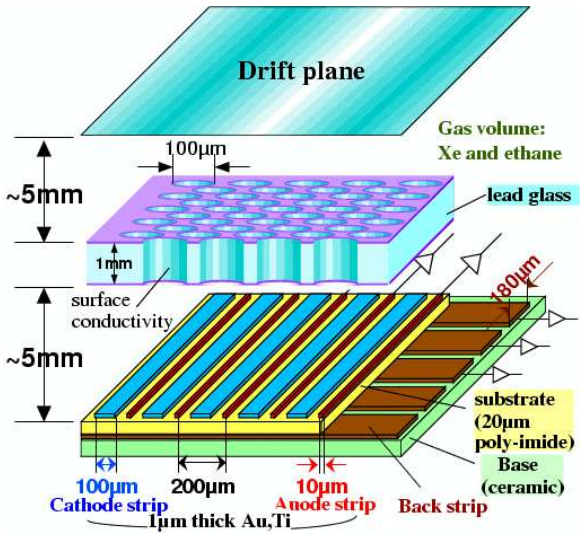

Figure 1.9: Schematic of the MSGC. Above the MSGC a preamlifier such as a capillary plate is installed due to supply a gas gain.

1.4 X-ray area detector based on μ-PIC

This study is aiming at providing powerful methods for structural determination, especially in SAXS field. SAXS measurements can be conducted using low-intensity X-ray source such as X-ray tubes but the use of third-generation synchrotron radiation sources is popular. Since the third-generation synchrotron radiation sources produce intense X-rays, measurement time can be shorten and dynamics of samples can be observed. However, radiation damage is a serious problem. To avoid radiation damage, there is a necessity of structural analysis of biological macromolecules and materials for industrial use conducted in a few minutes.

High-precision measurements are desired to analyze structure of materials containing light elements. Intensity of scattered X-rays by samples is roughly proportional to the electron density and thus atomic number Z. Thus, the contribution of the light elements to the scattering is small. Another reason for the request of the high-precision measurements is the feature of SAXS curves decreasing exponentially as q increases. Thus, precise observations of very low-intensity scattering patterns are crucial for the high-precision measurements. A detector that ensures linearity in a wide range can provide the high-precision measurements. At present, the IPs have observed scattering curves with the widest dynamic range of about 10^6. However, a solute scattering curve determined by subtracting a solvent curve from a solution curve maintain linearity in a range of about 10^5. It implies that accuracy of X-ray counts recorded by the IPs is 5 orders of magnitude. Our goal is to obtain solvent scattering maintaining linearity in a range of 10^{6-7} and thus accuracy of X-ray counts must be 6-7 orders of magnitude. The photon-counting type detectors are suitable for the high-precision experiments because fluctuation in X-ray counts is limited to statistical error.

The MSGC proved the advantages of the photon-counting detectors but it have not exhibited enough performances to withstand high-counting rates environments. It is not in practical use at present. As refinement of the MSGC, we have been developing an X-ray area detector based on

a micro-pixel gas chamber (μ-PIC) that is a micro-pattern gaseous detector [20]. The μ-PIC has totally different pixel structure from the MSGC and is robust for discharges. The performance of the μ-PIC will be described in the next chapter.

The X-ray area detector based on the μ-PIC is photon-counting type. Theoretically a dynamic range of the μ-PIC is infinite. Only cosmic muons and electronic noise contribute the background. The electronic noise can be easily eliminated because this system samples signals exceeding a threshold. The counting rates of the cosmic muons is limited to a few cps. Therefore, the contribution of the background is quite small and statistical uncertainty is dominant. This feature allows to measure low-intensity diffraction spots and scattering pattern precisely and will lead to high-precision measurements.

The μ-PIC has strip readout and charges are converted to digital signals. In consequence, the system is simple and then is able to deal with high-counting rates X-rays. Because of the simplicity, the cost of the μ-PIC detector system is much cheaper than the PILATUS that is another photon-counting detector.

To apply an X-ray detector to SAXS measurements, it needs to meet severe requirements mentioned above. Once a detector successfully proves its usefulness in this field, it can be applied to another field such as measurements using X-ray tubes whose intensity is much weaker. In theory, the background of photon-counting type detectors is quite low and do not depend on exposure time. Thus, they are suitable for a long-term exposure. They can be applied straightforward to the laboratory measurements once they show fine performance in high-counting rate environments.

1.5 Time resolved X-ray detectors

Recently time resolved measurements of SAXS has been attractive and expected to reveal a wide range of new phenomena. In spite of lots of efforts for a long duration, a time resolved X-ray detector applied to a wide range of fields has not been invented yet. At present, one should choose a detector suitable for each experiment and adjustments of the detector to the experiment are sometimes necessary.

Time resolved experiments are conducted using fast shutters or time resolved X-rays detectors. The fast shutters can open in a short period and control their timings. The time-resolved scattering pattern is observed with successive periods of measurements. Therefore the number of photons scattered in each experiment is quite small and an integrated-type detector with a high detection efficiency is employed for recording all incident photons. This method requires repetition of measurements and thus the range of the application is quite narrow. Especially, it limits use of biological material because of radiation damage. To use fresh object in each experiment one should prepare large amount of the object under investigation. To solve these problems X-ray detectors with a fine time resolution and capability of performing continuous measurements have been desired.

The photon courting-type detector is favorable for the time resolved experiments because it can easily associate the arrival time with the position of the incident X-ray. The MSGC and RAPID have already succeeded in it. In addition, they have no dead time due to readout. Thus they allow one to investigate the change of the scattering pattern continuously in a single measurement. However, the instability of these detectors avoids a wide range of uses. The μ-PIC developed at our laboratory encodes successively the position and the time of the incident X-rays. Thus, it is possible to arrange time-resolved measurements without dead time. Details of time-resolved measurements performed by the μ-PIC will be dealt with in the subsequent chapter.

Chapter 2

X-ray area detector based on μ-PIC

In this chapter, the characteristics of the μ-PIC , such as the structure of the detector and the principle of X-ray detection will be described. I will also discuss how the μ-PIC functions as an X-ray area detector. Currently, the X-ray area detector based on the μ-PIC is being developed with the aim of accurate observation of SAXS at third generation synchrotron facilities. The μ-PIC had been used mainly in low-counting rate environments before the application to the X-ray detector was started. Therefore, refinements to the system are required for operation in the high-counting rate environment of the third generation synchrotron facilities. These refinements will be considered in subsequent chapters.

2.1 The detector system based on μ-PIC

A μ-PIC is a micro-pattern gaseous detector fabricated by printed circuit board technology. The printed circuit board technology easily introduces an extension of the size of the detector. Figure 2.1 represents its schematic structure and Fig. 2.2 shows the pixel structure of the μ-PIC . An anode electrode structure surrounded by cathode rings prevents discharges in the μ-PIC [21] [22]. This structure makes the μ-PIC more robust against discharges than the MSGC.

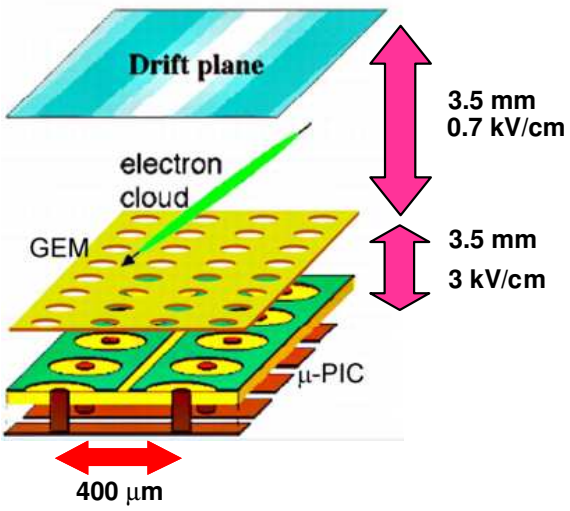

Figure 2.1: The schematic of the X-ray area detector based on the μ-PIC . Above the μ-PIC the GEM is installed and operated at a low gas gain.

Anode and cathode strips on the μ-PIC are formed orthogonally on a polyimide substrate with a pitch of 400 μm. We employed a strip readout to reduce the number of channels. As shown in Fig. 2.2, anodes are located in the center of each pixel and connected by a strip under a 100-μm thick substrate fabricated by an electric plating process. Figure 2.3 shows electric field around a pixel of the μ-PIC , calculated by Maxwell3D. A positive potential is applied to the anodes, and the cathodes are grounded, and then a strong electric field develops around the anodes. Electrons produced by charged particles drift along the electric field applied across the gas volume and reach at the anodes located in the center of the μ-PIC pixels. The electrons drift in the strong electric field around the anodes and produce avalanches. Thus, the electrons are amplified and detectable by electronics connected to the μ-PIC .

In the present work, a μ-PIC with an active area of 100×100 mm was used (manufactured by Dai Nippon Printing Co. Ltd.). Owing to the strip structure, the μ-PIC has 256×2 channels readout while it has 256×256 pixels ($= 6.6 \times 10^4$). The system where each strip is instrumented with an amplifier and a discriminator is simple and thus provides fast readout. Figures 2.4(a) and (b) show an overview and internal picture of the μ-PIC detector system. The electrode geometry was optimized by a three-dimensional simulation [23] [24]. The gas gain of the μ-PIC as a function of the voltage applied to the anodes is shown in Fig. 2.6. The maximum gain of 2×10^4 was achieved. Stable operation was achieved for more than 1000 h at a gas gain of 6000, with an Ar-C_2H_6 (90:10) gas mixture. The uniformity is an important issue for X-ray area detectors. The gain map is shown in Fig. 2.7 where the gas gain uniformity was $\sim 5\%$ (RMS) [25]. A two-dimensional position resolution of 120 μm rms, discussed in a subsequent section, was obtained for continuum X-rays around 10 keV with a Xe-C_2H_6 (70:30) gas mixture. A larger μ-PIC with an active area of 300 mm×300 mm has also provided a stable operation for over one month.

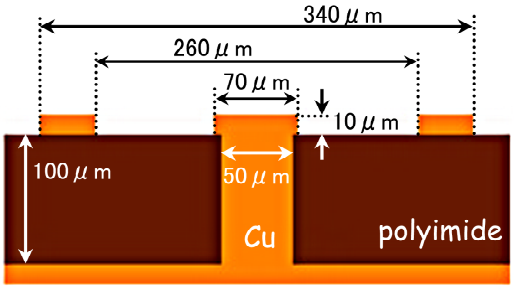

Figure 2.2: Schematic cross-section of the pixel structure of the μ-PIC .

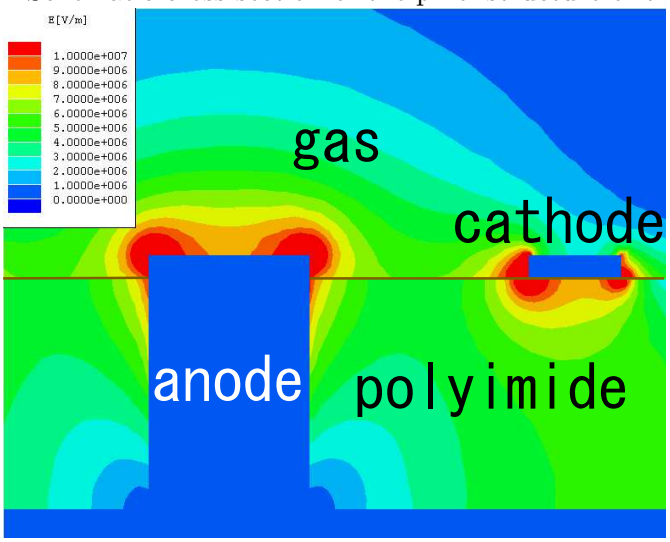

Figure 2.3: Electric field around a pixel of the μ-PIC . It was calculated by Maxwell3D. Electrons produced by charged particles drift along the electric field applied across the gas volume and reach at the anodes located in the center of the μ-PIC pixels. The electron drift in the strong electric field around the anodes and produce avalanches.

The principle of X-ray detection is almost the same as that of RAPID mentioned in the previous chapter. An X-ray photon is stopped in a gas (cf. Xe 70% C_2H_6 30%, Xe/Ar/CO_2), followed by induction of an electron, which creates electron clouds in the gas. The electron clouds then drift toward the GEM installed above the μ-PIC. The GEM consists of a polyimide insulator and copper electrodes. The copper electrodes are formed on both sides of the polyimide insulator, with holes of 50 μm diameter and a pitch of 140 μm. When a voltage is applied between these electrodes,

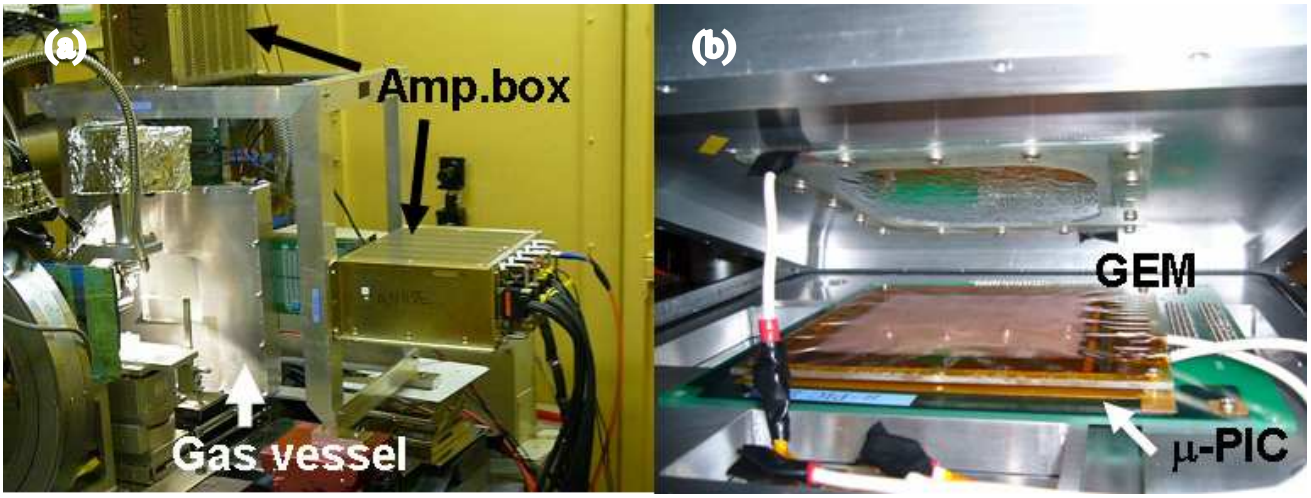

Figure 2.4: (a)Overview and (b)internal picture of the μ-PIC detector system.

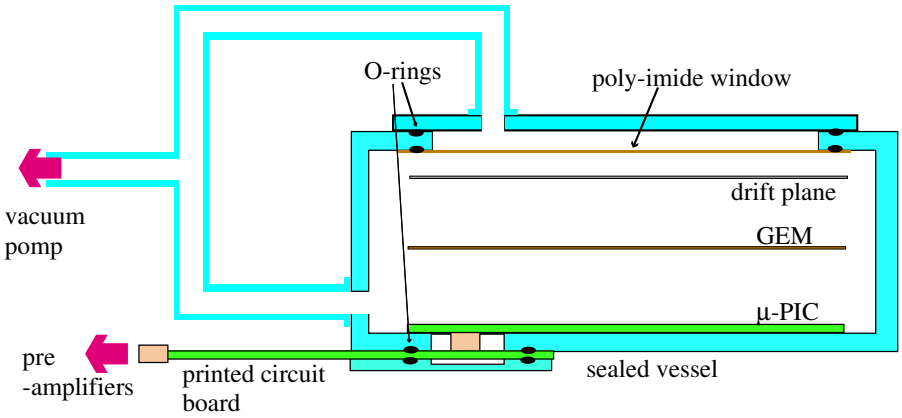

Figure 2.5: To protect the polyimide window, it is covered when the air is removed.

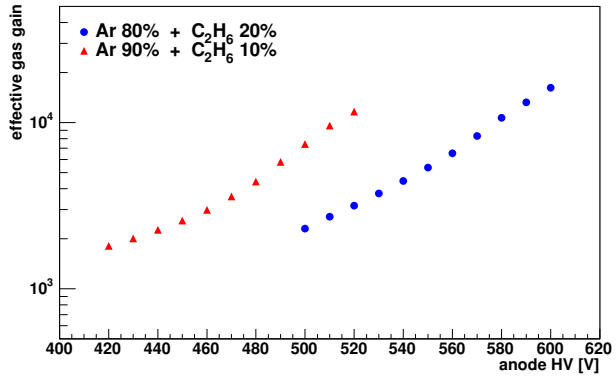

Figure 2.6: Gas gain of the μ-PIC as a function of the voltage applied to the anodes.

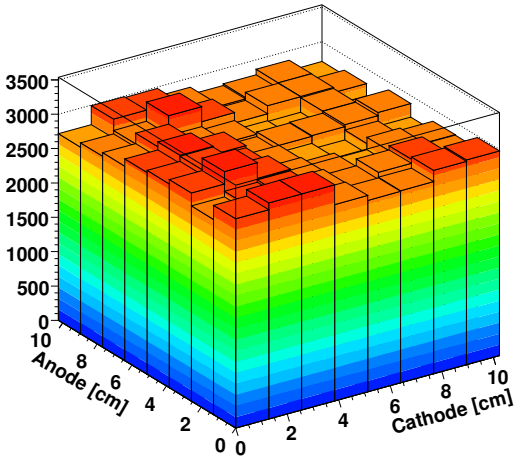

Figure 2.7: Gain map of the μ-PIC .

electrons are multiplied while passing through the holes. The electrons from the GEM drift toward the anodes on the μ-PIC and create avalanches around the anodes. The GEM, introducing a gain of 2 - 3, is temporarily installed due to lack of a gas gain of the μ-PIC. After enhancing the gas gain of the μ-PIC , the GEM will be removed. The GEM is positioned 3.5 mm from the μ-PIC and also 3.5 mm from the entrance window. We employed a GEM manufactured by Scienergy Co. Ltd. Japan. The electric field applied across the induction region was 3 kV/cm, and that across the drift region was 0.7 kV/cm, as shown in Fig. 2.1. The μ-PIC was operated at 2×10^3, the GEM at 3, and the total gain was about 5×10^3

The detector is contained in a sealed aluminium vessel with a polyimide entrance window of 0.1-mm thickness. The use of the polyimide limits 8-keV X-ray absorption at the entrance window to 10 %. The detector is filled with a Xe-C_2H_6 (70:30) gas mixture at a pressure of 1 atm. The vessel is designed to withstand a gas pressure of 1 atm in order to create a vacuum inside the vessel before filling it with gas. This operation shorten a time to renew gas inside the vessel. Since the creation of a vacuum reduces outgas after filling a sealed vessel with gas, this operation is necessary for a long-duration operation. We used Araldite to adhere the polyimide window to the vessel. Thus the entrance window may come loose when one side of the window remains at 1 atm and the other side is exposed to a vacuum. When the air is removed, the window is covered by an aluminium cap shown in Fig.2.5 and thus both sides of the window are kept under a vacuum. After filling the vessel with gas the cap is removed. The detector works stably for more than one month without renewing gas supply. The gas gains of the μ-PIC and the GEM decline by 10-20% after one month operation, but remain well above a threshold.

2.2 Readout system

Signal extension board

To connect all electrodes of the μ-PIC to the amplifiers outside the gas vessel, we developed the signal-extension printed circuit board shown in Fig. 2.8. It connects the μ-PIC inside the vessel to IC-amplifiers placed outside. In general, signals generated inside a sealed vessel are sent to electronics located outside through field-through connectors arranged at a wall of the vessel. The connectors using a large space are not suitable for 512-ch readout of the μ-PIC . On contrary, the extension board with only two connectors saves a space and provides a compact system. The extension board was held securely between the upper gas vessel and the bottom plate with O-rings, as shown in Fig. 2.5. On the board, resistors of 1 MΩ that function as dumping ones, jumpers and capacitors of 100 pF are arranged. Figure 2.9 shows a circuit diagram of the signal extension board. Each strip is connected to the high voltage supply via a resistor of 1 MΩ and a jumper. Each strip is also instrumented to readout via a capacitor of 100 pF and thus the high voltage applied to the μ-PIC is cut by the capacitor. The jumpers would be removed when one needs to isolate electronically a strip involving a discharging electrode. After the bad strip is isolated the μ-PIC can be operated without alteration of the detector properties. On the other hand, the resistors of 1 M Ω are arranged to reduce damage caused by discharges. The effects of a few missing strips on profiles of SAXS is negligible. On average, a few strips per detector are removed during one year operation. In the case of GEMs, once they incur serious damage caused by discharges, they need to be replaced with new ones. Therefore the μ-PIC is easy to handle and has attained a tolerance for long duration operation.

2.2.1 Amplifier-shaper-discriminator (ASD) chips

The data-acquisition system consists of amplifier-shaper-discriminator (ASD) chips [27], a position encoding module [28], and a memory module on a VME bus. Each ASD chip contains four channels of amplifiers and discriminators. A block diagram of the data acquisition system is shown in Fig.2.10. The output charges of the 256+256 channels are pre-amplified, shaped, and discriminated

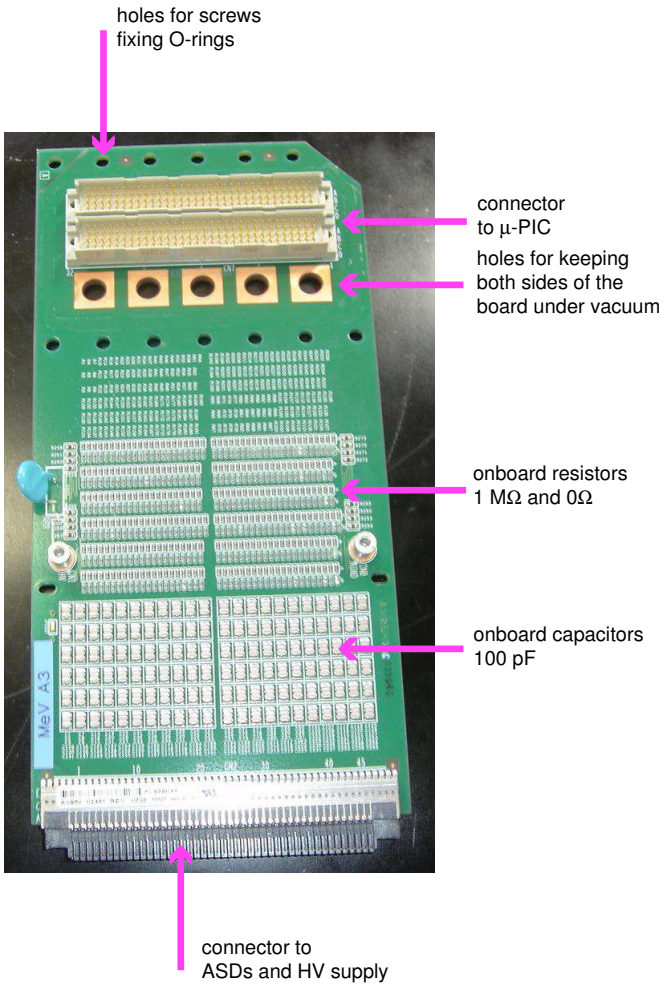

Figure 2.8: The signal-extension printed circuit board has connectors to μ-PIC , onboard resistors of 1 MΩ and jumpers, capacitors of 100 pF, and a connector to ASDs and high voltage supply. The jumpers are arranged for isolation of a strip involving a discharging electrode.

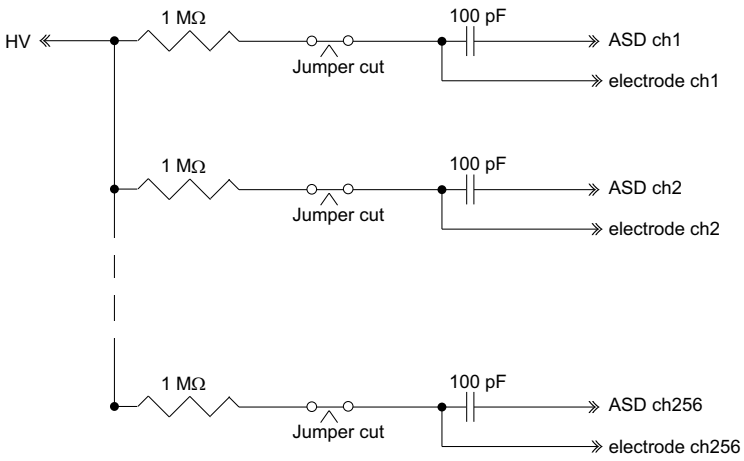

Figure 2.9: The circuit diagram of the signal extension board connecting the μ-PIC and the ASDs. Each strip is connected to high voltage supply via a resistor of 1 MΩ and a jumper.

in parallel by the ASD chips with a decay time constant of 80 ns. ASD chips with a decay time constant of 16 ns are also available. However, the decay time of 16 ns is short to integrate all electron clouds drifting toward the μ-PIC and thus their gain is sometimes insufficient to meet needs of some applications such as X-ray detectors and Time Projection Chambers (TPCs) observing Minimum Ionization Particles (MIPs). Therefore we used the ASD with decay time constant of 80 ns. A common reference threshold voltage was supplied to each of the ASD chips.

The time constant of signals integrated by the ASD chips was also determined by the integration time of charges generated in the μ-PIC . The oscillograms in Fig.2.11 show the resultant signal at the analog and digital outputs of the ASD with decay time constant of 80 ns against impulse inputs ranging from 0.1 pC to 0.4 pC. Figure 2.12 demonstrates the signal shape at the analog outputs of the ASDs with decay time constant of 80 ns and 16 ns. For plots of Fig. 2.12, the ASDs were connected to the μ-PIC irradiated with 5.9 keV X-rays. It should be noted that the time constant of the ASD analog output slowed down when it is connected to the μ-PIC . This fact implies that the time constant of signals generated by the μ-PIC is obviously slow. The charges generated by the μ-PIC are converted to the digital signals by comparators contained in the ASD chips in order to simplify the subsequent readout system. The timing chart with the analog output and the digital output of a channel contained in an ASD chip is shown in Fig. 2.13.

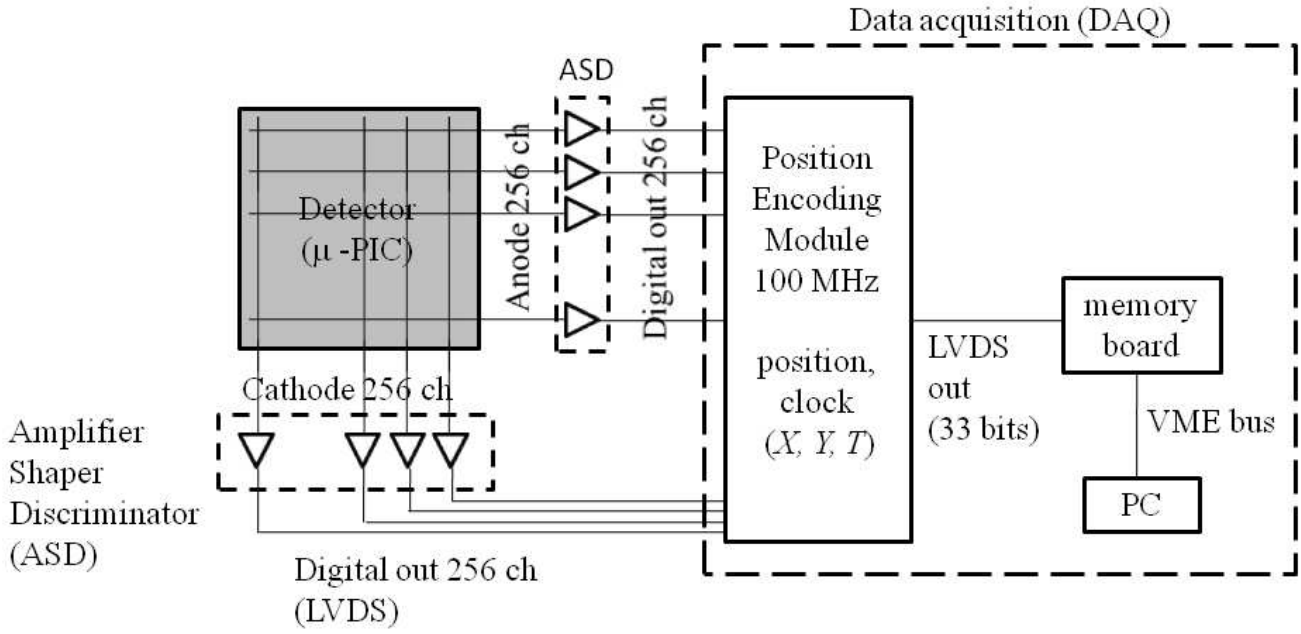

Figure 2.10: A block diagram of the data acquisition system.

2.2.2 Time walk at comparator output

Since digital signals are generated by the comparators at the instant, when the analog signals cross the threshold, the ASDs exhibit time walk for variations in the amplitudes of the analog signals. Figure. 2.14 shows the propagation delay at the comparator output as a function of input charge. The ASD with a decay time constant of 16 ns was used. Overall time walk is less than 4 ns when the input charges are in the range of 0.05 pC to 2 pC.

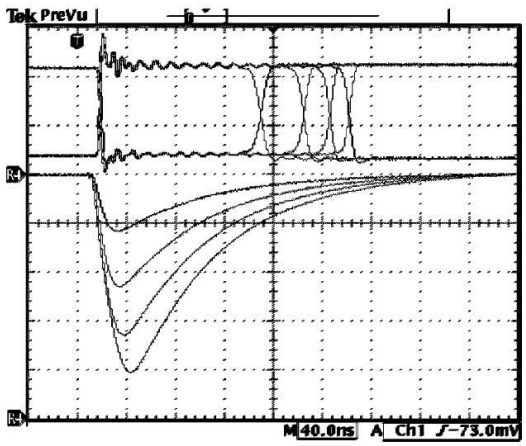

Figure 2.11: Resultant signal at the analog and LVDS digital outputs of an ASD against impulse inputs ranging from 0.1 pC to 0.4 pC. Decay time constant of the ASD is 80 ns. The grid cell is of 40-ns × 50-mV size[27].

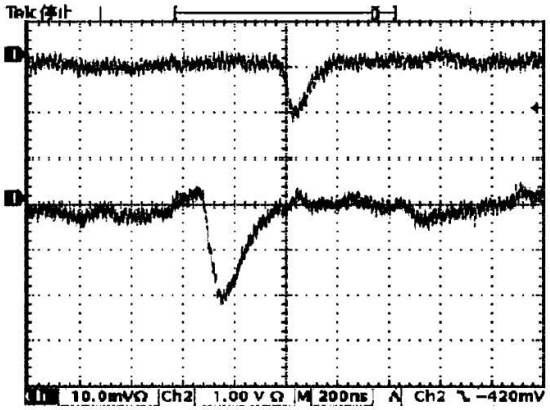

Figure 2.12: Signal waveform at the analog outputs of the ASDs with decay time constant of 80 ns (lower) and 16 ns (upper). The ASDs amplified signals from the μ-PIC irradiated with 5.9 keV X-rays.

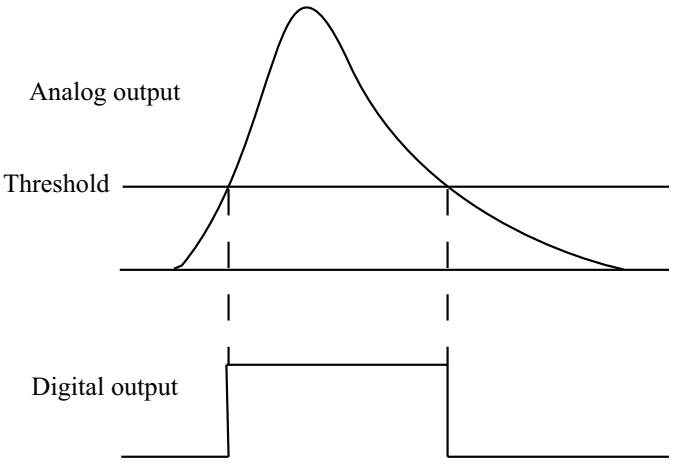

Figure 2.13: Timing chart with the analog output and the digital output of a channel contained in an ASD chip. The rising edge is sampled by the position encoding module.

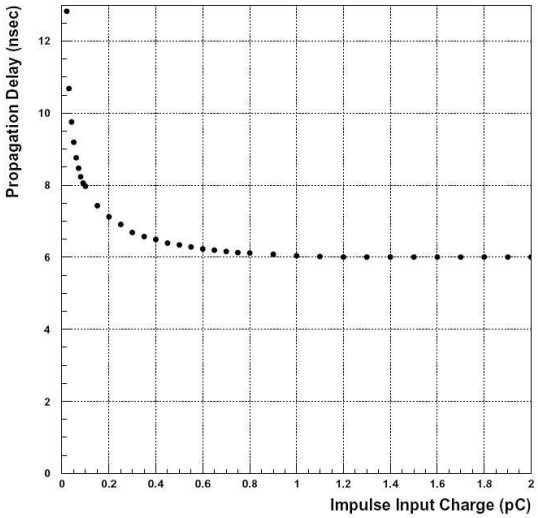

Figure 2.14: Propagation delay at comparator output as a function of input charge. An ASD with a decay time constant of 16 ns was used. Overall time walk is less than 4 ns when input charges are in the range of 0.05 pC to 2 pC.

2.2.3 Encoding module

All discriminated digital signals are sent to the position encoding module consisting of Field Programmable Gate Arrays (FPGA) with an internal clock of 100 MHz, allowing the recording of the anode and cathode coincident position= (X, Y) and the time (T) to the memory module. Figure 2.15 shows a schematic of the encoding system. The position encoding is performed in the following steps:

1. *Edge detection* The FPGAs sample digital signals from the ASDs at their rising edge shown in Fig. 2.13. Because only the rising edges are monitored, each channel is insensitive to any subsequent signals while the signal from the μ-PIC exceeds the threshold.

2. *Synchronization* The timing of the signal is synchronized with the internal clock of the FPGAs.

3. *Coincidence* When the synchronized signals originating from the anodes and the cathodes coincide in a clock interval (10 ns), the two dimensional position time-stamped with a resolution of 10 ns, is calculated. We used the coincident signals to improve signal-to-noise ratio. The time resolution is determined by the internal clock of the FPGAs (10 ns).

4. *Position encoding* If two or more channels generate signals within a clock of 10 ns, the average of the channels for the maximum and minimum coordinates is calculated. If the difference between the maximum and minimum coordinates is more than eight, the events are discarded. The range of electrons liberated by 10-keV X-rays in a gas is much shorter than 3.2 mm (corresponding to 8 channels $\times$0.4 mm). Therefore most events having a wider width than 8 channels are considered to involve noise.

5. *Data Readout* The resultant data are buffered in a FIFO on the encoding module unless the FIFO overflows with data. Then the data are output to the memory board at a rate of 50 MHz and stored. The memory board can hold 8.7 Mevents. Taking into account the transfer rate to the memory board, the FIFO overflows at counting rates of more than 50 MHz and as a consequence, a part of the data are lost.

Thus, the position encoding is completely executed by digital processing. This method dramatically increased the limit on counting rates to >1 Mcps, while conventional methods based on analogue pulse processing, such as delay lines and charge division, have achieved a counting rate of several hundreds of kcps. Moreover, the simple digital readout contributes much to the stability of the detector system and the convenience for users.

2.2.4 ASD reference threshold

In this experiment, the ASD reference threshold voltage was set to 25 mV, which corresponds to about 7×10^4 electrons (= 0.01 pC). This value is determined by both the gain of the ASD chips (0.3 pC/V) and the buffer amplification for the ASD comparator ($\times$7). This number of electrons corresponds to the energy deposition of about 0.17 keV X-ray photons in Xe gas, when the gas gain is 10^4.

An X-ray photon of 13.8 keV generates about 600 primary electrons in Xe gas, which distribute over approximately 4 strips in the μ-PIC . These electrons are amplified to 6×10^6 by the μ-PIC and the GEM. Then, the number of amplified electrons deposited is 1.5×10^6 per strip on average, which corresponds to 3keV. Considering a Gaussian-like distribution for an electron cloud, a 5 keV energy deposit is expected on at least one strip. Despite of the large uncertainty of gains and non-uniformity (a few 10% at maximum), the threshold allows sufficient margin for counting loss. The background counts reached a few cps due to cosmic-ray muons and electrical noise. This counting rate is much lower than the counting rates of X-rays. Thus, the background counts were negligible in the experiments performed at SPring-8.

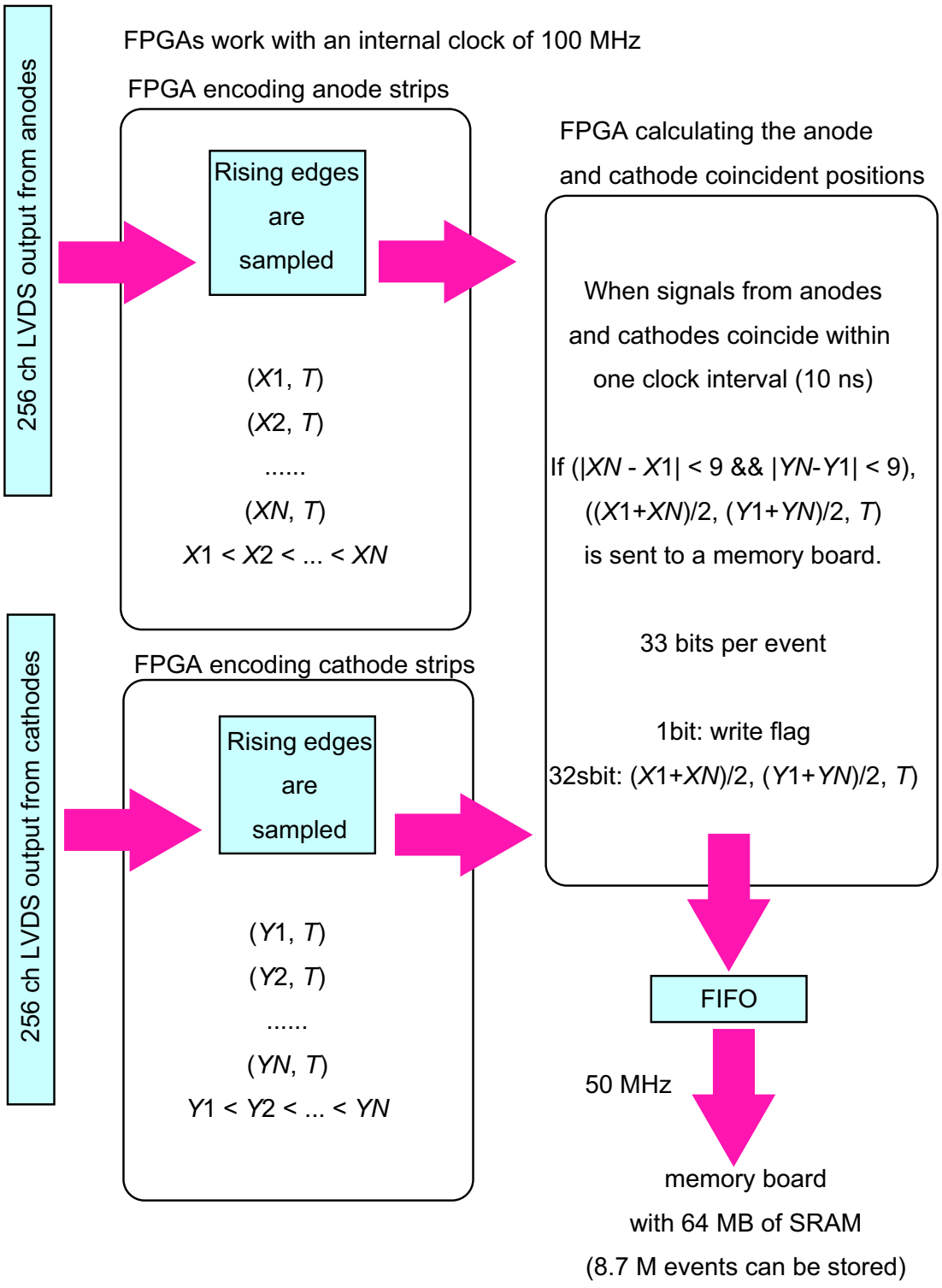

Figure 2.15: A block diagram of the position encoding system used for the X-ray area detector.

2.2.5 X-ray imaging

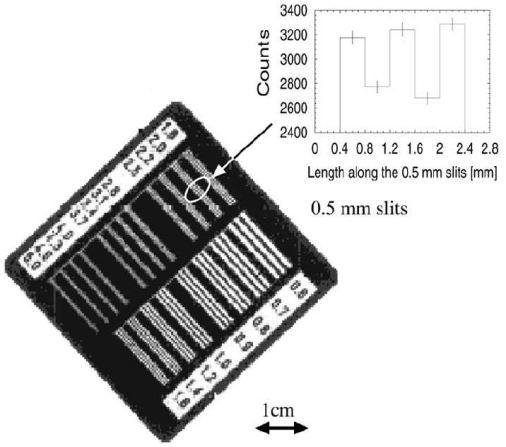

Figure 2.16: X-ray image of a test chart irradiated with an X-ray generator [26]. The slits of various width are scribed in the 0.05 mm thick lead layer on the plastic plate. The slits of 0.5 mm width are separated clearly.

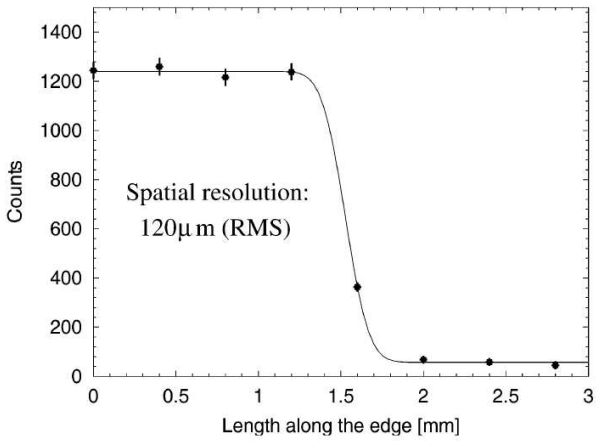

Figure 2.17: Projection along the edge of the test chart fitted by $a_1 + a_2\mathrm{erf}((x-a_3)/(\sqrt{2}\sigma))$, where $\mathrm{erf}(x) = \int_0^x \exp(-t^2)\mathrm{d}t/\sqrt{\pi}$ and a_1, a_2, a_3, σ are determined by fitting.

Using this position encoding system, two-dimensional X-ray imaging was performed. The output of the encoding module was integrated without corrections and two-dimensional images were obtained. Figure 2.16 is the image of a test chart irradiated with an X-ray generator [26]. The acceleration voltage of the X-ray tube was set to 12 kV with a 1 mm thick aluminum filtering to cut low energy X-rays. To enhance the position resolution, the vessel was filled with a Xe based gas mixture (Xe 70% C_2H_6 30%). Xenon has a large stopping power, and thus a practical range for electrons liberated by 12 keV X-ray is 1 mm in xenon gas whereas the range in argon gas is 2 mm. For this reason, a xenon gas was used. The detection depth was set to 2 mm to reduce diffusion effects. The position resolution was evaluated from this image.

If the fluctuation of encoded positions is characterized by a Gaussian distribution with deviation σ, the projection of an edge will be described by the error function. Figure 2.17 shows a projection along the edge of the test chart fitted by $a_1 + a_2\mathrm{erf}((x-a_3)/(\sqrt{2}\sigma))$, where $\mathrm{erf}(x) = \int_0^x \exp(-t^2)\mathrm{d}t/\sqrt{\pi}$. The parameter σ, corresponding to the position resolution of the μ-PIC, was determined to be 120 μm, . The position resolution of a pixel gaseous detector with a pitch of d is theoretically limited by $\sigma = d/\sqrt{12}$. The theoretical limit of the μ-PIC is $400/\sqrt{12} = 115$ μm, which is close to the measured position resolution. Thus the position resolution is reasonable and of good quality.

2.2.6 Time Projection Chamber based on μ-PIC (micro-TPC)

The μ-PIC also delivers another application, a Time Projection Chamber (micro-TPC). The two-dimensional data combined with timing information allows the reconstruction of the three-dimensional tracks of charged particles. Figure 2.18 shows a schematic of the micro-TPC. The charged particles causes the formation of clouds of ions and electrons in gas. The electron clouds drift toward the μ-PIC along the electric field applied across the gas volume. Because of the constant drift velocity of electrons within the gas of the detector, electron clouds generated at different height above the μ-PIC will reach the surface of the μ-PIC at different times. This time lag is proportional to the height of the electron cloud, and thus their relative position can be reconstructed using the timing

information. If the encoding module is triggered by a simultaneous event, the absolute height can be obtained.

Figure 2.19 shows a block diagram of the position encoding system used for the micro-TPC. The system is almost the same as that mentioned in the previous section, but the format of the output data is different. In the case of the micro-TPC, two-dimensional positions are not averaged. Instead, the maximum and minimum coordinates are recorded and thus one can derive the sizes of the electron clouds. The output data also contain additional information to identify events belonging to the same trigger (*event_ID*, see Fig.2.19). In this method, events with a big difference between the maximum and minimum coordinates must be removed because they occasionally involve noise. Thus, deriving the maximum and minimum coordinates is useful to improve signal-to-noise ratio. To measure absolute positions, the position encoding system is triggered by a signal produced in coincidence with the charged particles. Then, the absolute positions can be calculated using the drift velocity in the gas and the time difference between the trigger and the arrival times of the electron clouds.

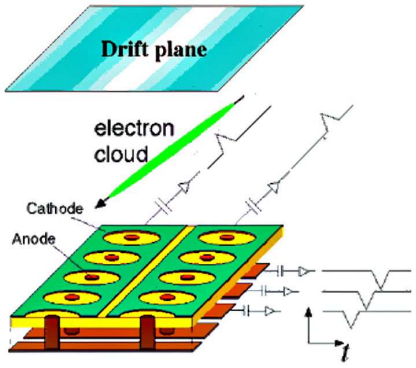

Figure 2.18: A schematic of a micro-TPC. Because of the delay in arrival times of electron clouds at the surface of the μ-PIC , the ASDs amplify the signals from the μ-PIC at different times.

Figure 2.20 shows a typical cosmic muon track. The micro-TPC with the detection depth of 15 cm was filled with a 1atm Ar-C_2H_6 (90:10) gas mixture. The detector was operated at a high gas gain of 3×10^4 to ensure that the small charge deposition of MIPs, 4 electrons per strip (with a pitch of 400 μm), exceeds the detection threshold. Two plastic scintillators were located above and below the micro-TPC. A coincidence of these scintillators was used for the muon trigger and the absolute height of the track was measured. The position resolution of muon tracks was about 400 μm.

2.3 Calibration of X-ray area detector

In this section, fundamental issues in calibration of X-ray area detectors, calculations of a camera length and a refinement of non-orthogonality to the beam, will be described.

2.3.1 Camera length

To obtain a scattering angle, the camera length defined as the distance between the sample and the detector plane must be measured. In general a well-known powder having strong Debye-Scherrer rings is favorable for the camera length calibration. Since the diffraction angles of the rings are known, the camera length can be calculated. In addition, the shape of the rings provides information of the non-orthogonality of the detector. We used silver behenet and CeO_2 powder for calibration at the SPring-8 and the KEK-PF beam line, respectively.

We used the two-dimensional data analysis program FIT2D developed by Hammerley [29] for the correction. The FIT2D provides 2-theta scans of the rings. It also allows a beam center and the non-orthogonality of the detector to be refined.

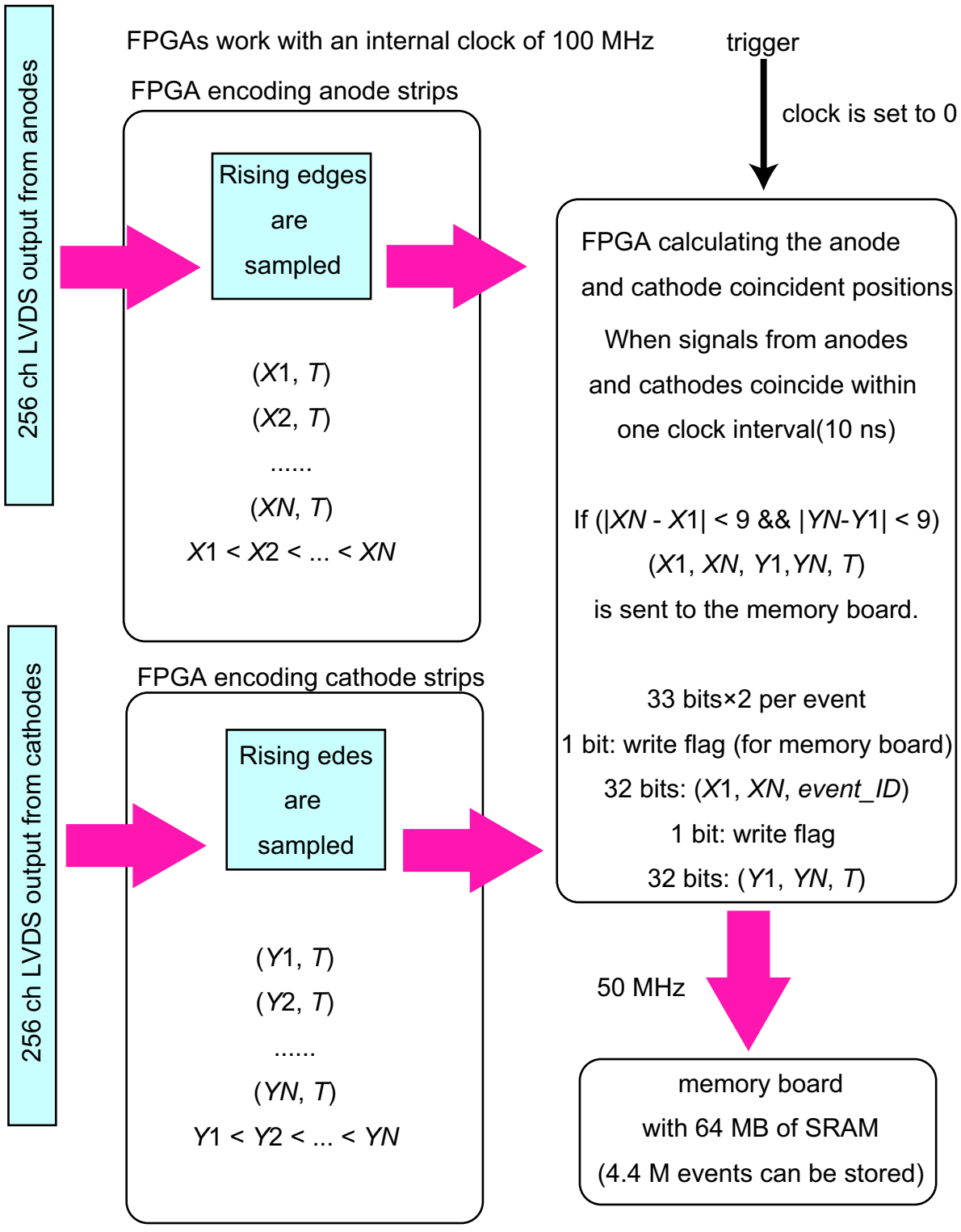

Figure 2.19: A block diagram of the position encoding system for use with the micro-TPC.

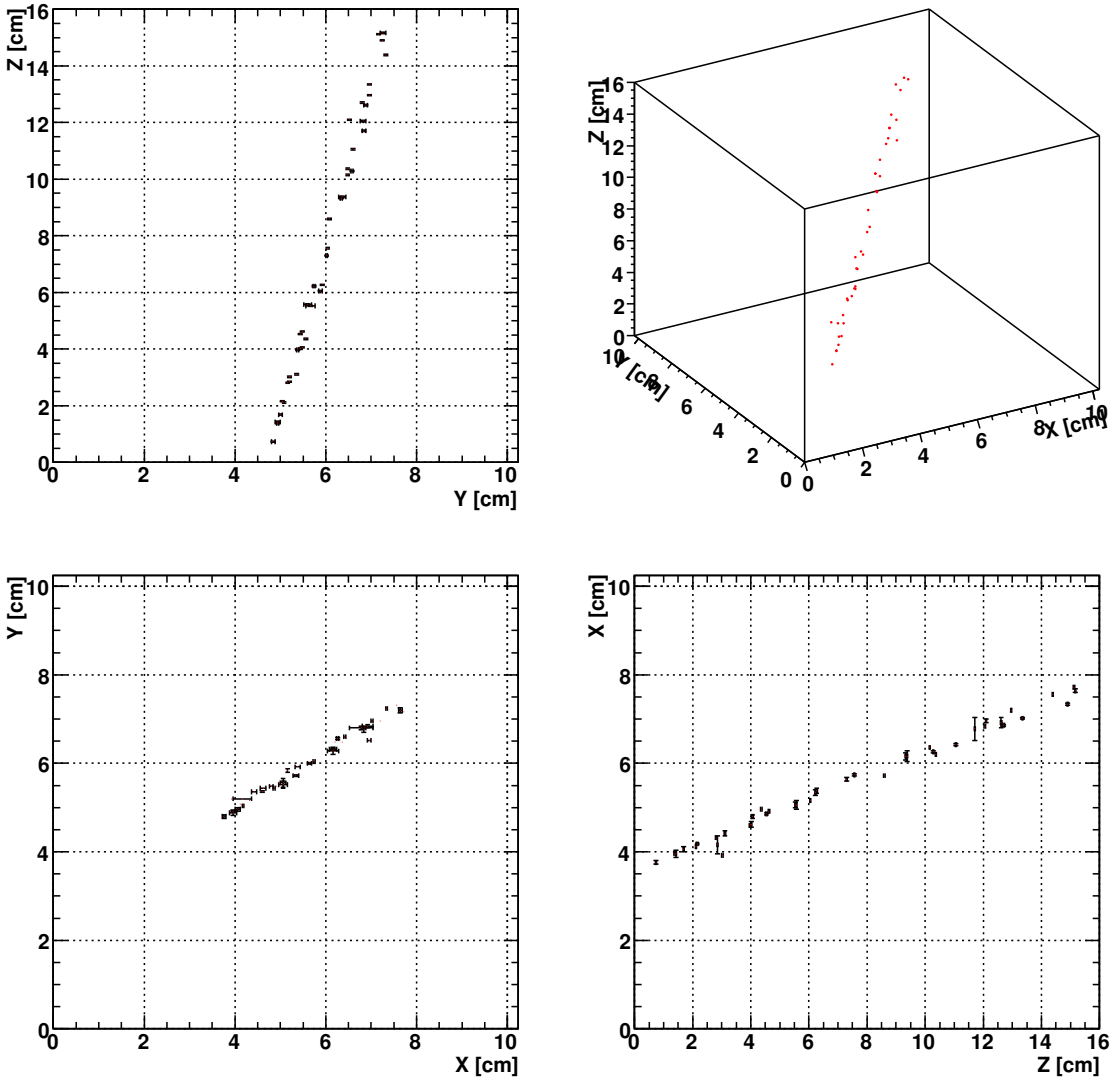

Figure 2.20: Typical cosmic muon track.

2.3.2 Refinement of non-orthogonality

Occasionally, the detector is irradiated with the beam at a slant to reduce the parallax effect in a wide-angle region. In general, the detector should be aligned perpendicular to the beam but it is difficult to eliminate a small deviation from the correct position. Therefore, there is a need to correct for this non-orthogonality.

We now consider the projection of the rings to the detector plane. A spatial orientation of the frame of the detector is expressed by Euler angles. The detector system is denoted by the letters (X, Y, Z) and a reference system is denoted by the letters (x, y, z), shown in Fig. 2.21. The direction of the z-axis is defined to be parallel to the beam. The Euler angles ϕ_0, θ_0, ψ_0 are defined as below:

- ϕ_0 represents a rotation angle around the axis z of the original reference frame.
- θ_0 represents a rotation angle around an intermediate X axis, which corresponds to an angle between the z-axis and the Z-axis.
- ψ_0 represents a rotation angle around the axis Z of the final frame identical to the detector frame.

The position of a point on the detector is expressed by (X, Y, 0) in the detector coordinate system. A coordinate transformation to the reference system is done by multiplication of the matrices representing the three simple rotations. The resultant coordinate is expressed as in the equation

$$\begin{pmatrix} x \\ y \\ z \end{pmatrix} = \begin{pmatrix} 0 \\ 0 \\ l \end{pmatrix} + \begin{pmatrix} \cos\psi_0 & \sin\psi_0 & 0 \\ -\sin\psi_0 & \cos\psi_0 & 0 \\ 0 & 0 & 1 \end{pmatrix} \begin{pmatrix} \cos\theta_0 & 0 & -\sin\theta_0 \\ 0 & 1 & 0 \\ \sin\phi_0 & 0 & \cos\phi_0 \end{pmatrix} \begin{pmatrix} \cos\phi_0 & \sin\phi_0 & 0 \\ -\sin\phi_0 & \cos\phi_0 & 0 \\ 0 & 0 & 1 \end{pmatrix} \begin{pmatrix} X \\ Y \\ Z \end{pmatrix}, \quad (2.1)$$

where l is a distance between the sample and the detector. A Debye-Scherrer ring with a scattering or diffraction angle of 2θ is included in a region expressed as in the equation

$$x^2 + y^2 - z^2\tan^2 2\theta = 0. \quad (2.2)$$

On substituting (x, y, z) by equation (2.1), the projection of equation (2.2) to the detector plane is given by

$$X^2(\cos^2\theta_0 - \sin^2\theta_0\tan^2\theta) + Y^2 + 2lX\sin\theta_0\tan^2\theta - l^2\tan^2\theta = 0. \quad (2.3)$$

Since the geometry has symmetry with respect to rotations about the beam (the z-axis), ϕ_0 and ψ_0 vanish in equation (2.3). The projection is a hyperbola when $\cos^2\theta - \sin\theta_0\tan^2\theta < 0$. It is an ellipse when $\cos^2\theta - \sin\theta_0\tan^2\theta > 0$. The plots of the lefthand side of Fig. 2.22 show examples of the projections for various values of θ. They demonstrate simulations of a diffraction pattern for a CeO_2 powder irradiated with 0.7744 Å X-rays. The camera length was set to 125 mm. The points follow a Gaussian distribution with width $\sigma = 0.08$ mm. The plots of the lefthand side of Fig. 2.22 were transformed to a plane vertical to the beam. The figures on the righthand side show the transformed plots.

2.4 Time-resolved measurements

In this section, two examples of time-resolved measurements using the X-ray area detector based on the μ-PIC and the encoding system are described: time-resolved X-ray diffraction and the Continuous Rotation Photograph (CRP) method. The detector system was able to perform time-resolved measurements without significant dead time. Advantages of continuous time-resolved measurements are also discussed in following sections.

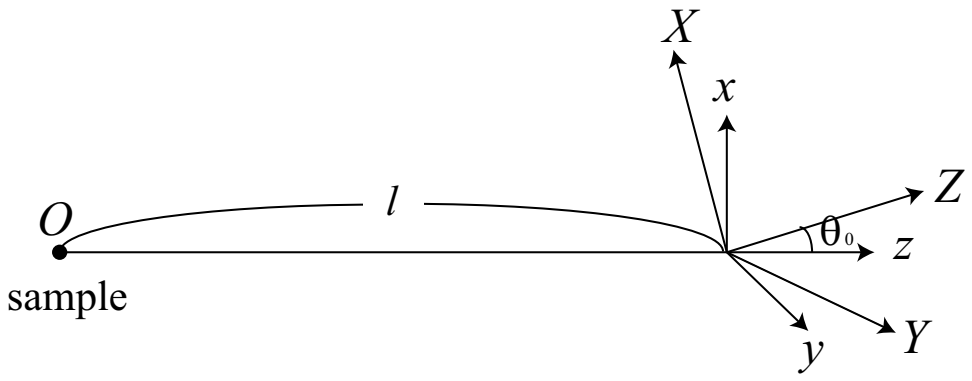

Figure 2.21: Definition of the detector coordinate system (X, Y, Z) and the reference system (x, y, z). The direction of the z-axis is defined to be parallel to the beam.

2.4.1 Time-resolved X-ray diffraction

Figure 2.24 and 2.25 show a pyromellitic acid hydrate and anhydrate powder diffraction pattern obtained with the X-ray area detector based on the μ-PIC . The hydrate is a compound formed by the addition of water to the pyromellitic acid and the anhydrate is one that loses the water. Since they are powder diffractions, the intensity of diffracted photons depends on only 2θ. The objects were irradiated with 0.7 Å X-rays at KEK-PF. The distance between the detection area and the sample was 137 mm. The experimental setup is shown in Fig. 2.23. The diffraction patterns of the hydrate and anhydrate are clearly different and it is easy to distinguish these objects. The detector was placed perpendicular to the beam and thus the peaks in high-angle region are wide. To reduce this parallax effect, the detection depth should be reduced and the detector should be placed on a tilt to the beam. In the case of SAXS measurements, 2θ is typically less than a few degrees and the parallax is negligible.

The hydrate loses the water and becomes the anhydrate when heat is applied (140 °C). The removal of the water from the hydrate is called dehydration. The anhydration diffraction pattern shown in Fig. 2.24(b) and 2.25 was observed after the dehydration reaction had finished.

To prove the efficiency of continuous time-resolved measurements and measure the time resolution, the dehydration reaction was observed in real time. The reaction occurs so quickly that the dehydration process itself can not be observed by the μ-PIC detector system. On the other hand, the weight fraction of the hydrate changes much more slowly, within several seconds. Thus the observed diffraction pattern is determined by the weight fraction of the hydrate. Figure2.25 shows the time-resolved profile as a function of time. In Fig. 2.25 and Fig. 2.27, one can see that the reaction occurred in about 7 sec and the diffraction pattern clearly changed.

Assuming the background and mass absorption coefficient are constant, the observed intensity $I(2\theta, t)$ is expressed as $I = xI_d(2\theta) + (1-x)I_h(2\theta)$, where $I_d(2\theta)$ ($I_h(2\theta)$) is the intensity of the anhydrate (the hydrate) including the constant background. The mass absorption coefficient of the object will change as unbound water is evaporated. However, the contribution of evaporated water to the X-ray absorption is small and thus the mass absorption coefficients for the hydrate and the anhydrate are sufficiently close. The diffraction pattern at each frame is fitted by $I = xI_d(2\theta) + (1-x)I_h(2\theta)$ and x is obtained from the fit.

The time-resolved x as a function of time is shown in Fig. 2.28. The weight diffraction of hydrate starts from 1 and ends with approximately 0, which means the dehydration has finished. The x values are plotted every 0.65 sec using 4.3×10^4 events. In the case of this system, analysis of diffraction patterns generally requires more than 10^4 events. Therefore the time resolution is determined by not only the counting-rate limit of the encoding system but also the intensity of X-rays. We used the low-intensity X-ray beam at KEK-PF and observed the slow diffraction change.

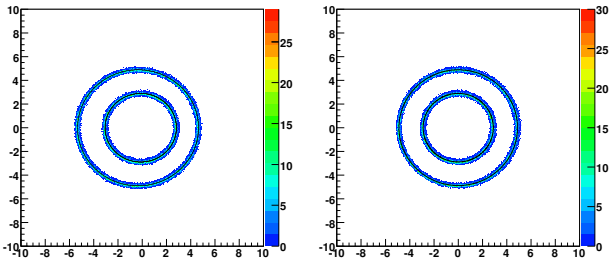

(a) $\theta = 10^\circ$

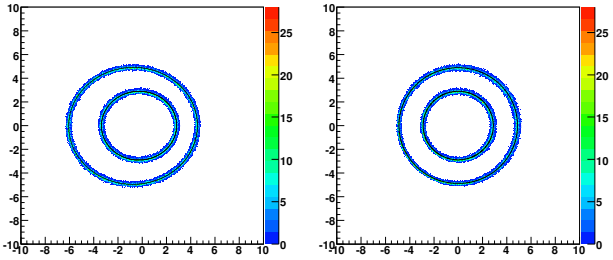

(b) $\theta = 20^\circ$

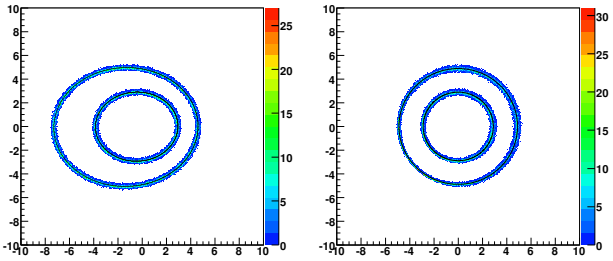

(c) $\theta = 30^\circ$

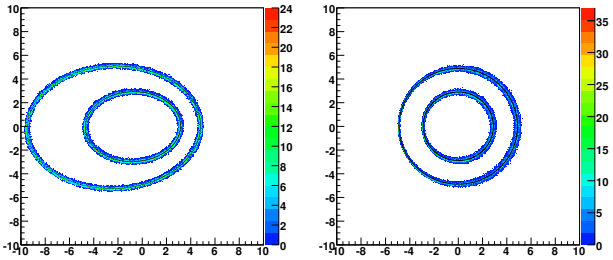

(d) $\theta = 40^\circ$

Figure 2.22: Projection of diffraction cones to a slanted detector plane with $\phi = 0^\circ$ and $\psi = 2^\circ$ (left). The plots of the lefthand side are converted to ones in a plane vertical to the beam (right).

The counting rates of 70 kcps at this experiment has enough margin for encoding system. If samples are irradiated with the higher intensity third-generation synchrotron radiation sources, higher time resolution would be expected. Considering the encoding system (100 MHz), our goal is to observe X-rays at a counting rate of 10 MHz. At this counting rate, one can obtain 10^4 events every 1 msec. Therefore, adjustments of the detector system to high counting rate environments is important in terms of fine-time-resolved experiments.

For most of the X-ray area detectors currently available, dead time caused by readout is unavoidable and diffraction patterns are recorded in limited intervals. Even the PILATUS, another photon counting detector, is not free from the dead time, and repeated measurements using fast shutters are required. Instead of continuous measurements one should prepare a large amount of samples and use repeated measurements to collect the data of diffraction pattern in each period. Thus it takes a long time to measure all periods of the diffraction. A solution to this problem is to combine three-fast CCDs, successively irradiate X-rays and read charges generated by X-rays [30]. This method provides continuous measurements at a frame rate of 3.4 msec. However, fast CCDs have large readout noise that narrows the dynamic range. Furthermore, the CCD system is so complex that they cannot be triggered by other instruments such as a beam monitor. These features also prevent the CCD system from achieving wide utility.

Another solution for avoiding dead time is counting photons one-by-one and recording continuously. One-by-one photon counting is easy for gas detectors because there is no need to integrate charges in the detection area and one can obtain signals in real time. We successfully developed the system that count photons one-by-one and encodes their positions in real time. The X-ray area detector based on the μ-PIC will provide a powerful tool in time-resolved X-ray measurements if the maximum global counting rate is enhanced to 10^7 photons/sec.

In this paper, we will focus on measurements of Small Angle X-ray Scattering, which also requires adjustments of the detector system to high counting rates environments. Therefore, detector systems succeeding in measurements of SAXS also lead to fine-time resolution for time-resolved measurements.

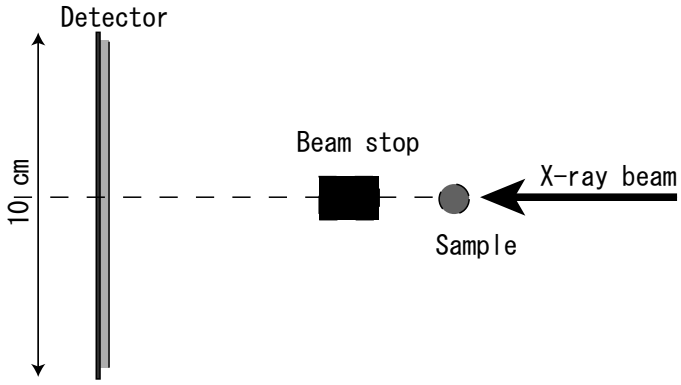

Figure 2.23: Schematic top view of instrumentation generally employed in this paper.

2.4.2 Continuous rotation photograph (CRP) method

Although the photon-counting area detectors such as PILATUS and the μ-PIC have been developed recently , diffraction patterns from a single crystal were recorded by integrated-type area detectors. The crystal is oscillating during the measurements to observe the diffraction patterns at various angles. To observe a wide range of 2θ one should conduct many experiments with changing slightly the rotation angle of the crystal.

A photon-counting type area detector, MSGC showed the new approach [31] [32]. The continuous rotation photograph (CRP) method was employed allowing all diffraction spots from the

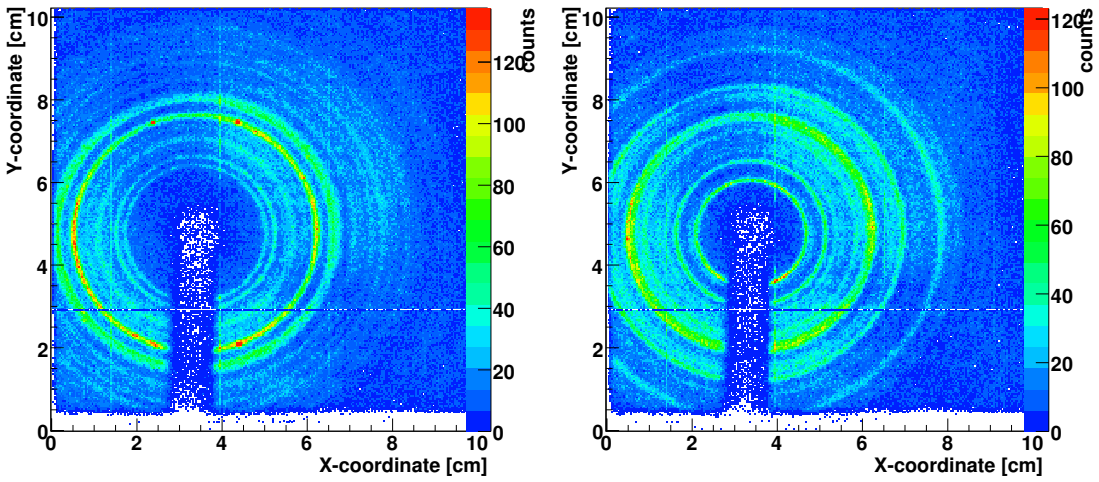

(a) Hydrate

(b) Anhydrate

Figure 2.24: Raw images of a hydrate and an anhydrate. The diffraction from the anhyadrate was measured after the dehydration reaction had finished.

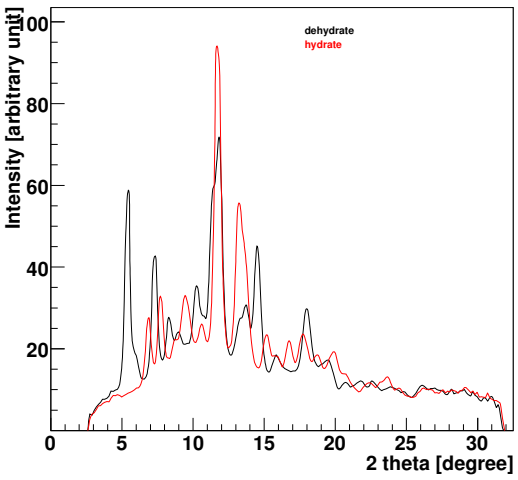

Figure 2.25: Profiles of a pyromellitic acid hydrate and anhydrate. The diffraction from the anhydrate was measured after the dehydration reaction had finished.

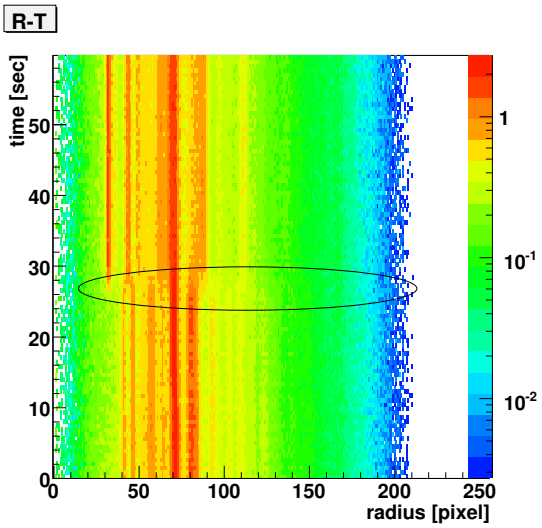

Figure 2.26: Time resolved diffraction pattern as a function of time. The dehydration reaction of a pyromellitic acid hydrate occured within 7 sec.

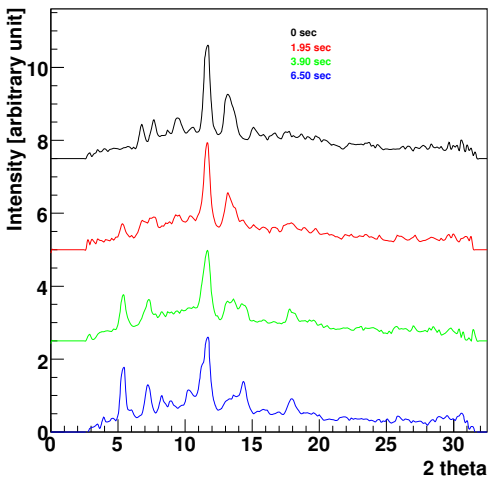

Figure 2.27: Time resolved diffraction pattern as a function of time. 0 sec is defined as the time when the dehydration reaction started.

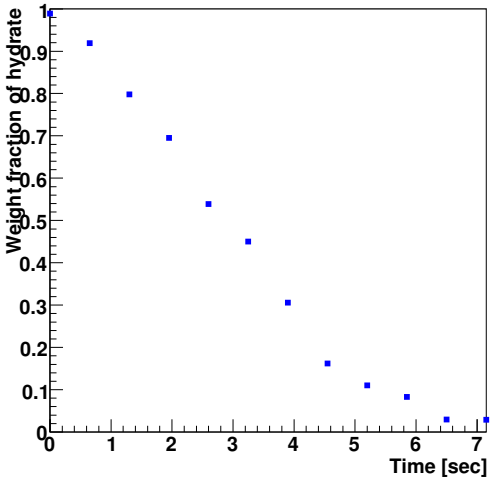

Figure 2.28: Weight fraction of the hydrate as a function of time. 0 sec is defined as the time when the dehydration reaction started. The reaction is almost finished at 7 sec.

crystal to be observed in a short period of a few seconds. In this method, the crystal rotates around an axis using a goniometer. The CRP method requires a time-resolved area detector which can associate the arrival time of a photon to the instantaneous rotation angle of the crystal. The detector then provides a movie of the diffraction spots as the crystal rotates 360° or 180°. The angular resolution of the diffraction spots is expected to be less than 0.1°. Using intense X-rays, the measurement would be completed after a few rotations of the crystal. A measurement during many rotations would enhance the accuracy of the data. The CRP method introduces a new parameter, the rotation angle and hence it allows to remove most of the background X-rays.

The MSGC proved that the CRP method was useful and drastically shortened the measurement time to a few seconds, which was 100 to 1000 times faster than CCDs and four-axis diffractometer currently in use in this field. However, the MSGC, suffering from serious discharges and critical damages caused by discharges, was operated at a low gas gain of 1000 and maintained stable operation for only a short period. The signal-to-noise ratio was deteriorated by the low gas gain and lack of data. Thus 9% internal agreement factor ($R_{\rm int}$) that MSGC achieved could not be improved. Due to the instability, the MSGC did not meet the requirements of X-ray crystallography [21]. $R_{\rm int}$ represents the degree of an agreement between experimental values and calculated values. $R_{\rm int}$ is 0 % when these values completely agree and high-precision measurements reduces $R_{\rm int}$.

Alternatively, we examined the CRP method using the μ-PIC , which is more robust against discharges and has attained stable operation for more than one month. Figure 2.29 shows integrated diffraction spots form a rotating Ylid ($C_{11}H_{10}O_2S$) crystal. Figure 2.30 shows the diffraction spots as a function of the rotation angle. In this experiment, the μ-PIC was used without a GEM and worked stably at a gas gain of 3000. A 1atm Ar-C_2H_6 gas was filled in the vessel. We used the Ar-based gas for maintaining a stable operation though the gas has less stopping power than the Xe-based gas generally used. Although the raw data shown in Fig. 2.30(a) contains a large amount of X-ray scattered by the air, the clusters of diffracted photons are clearly recognized in the three-dimensional space. Thus, it is possible to eliminate the background X-rays and Fig. 2.30(b) shows the diffraction spots after the background reduction. Using these diffraction spots an internal agreement factor, $R_{\rm int}$ of 3.7 % was obtained for an exposure time of 3700 sec. The Ylid crystal was irradiated with an X-ray generator, and thus the burst rate of the strongest diffraction spots

was at most 3.6×10^5 cps, which was well within the capabilities of the current encoding system. Irradiation with intense X-rays generated by third-synchrotron radiation sources would provide an R_{int} of less than 1%.

It can be concluded that adjustments of the detector system to high counting rate environments is useful not only for SAXS experiments but also measurements of time-resolved powder diffractions and the CRP method with high accuracy.

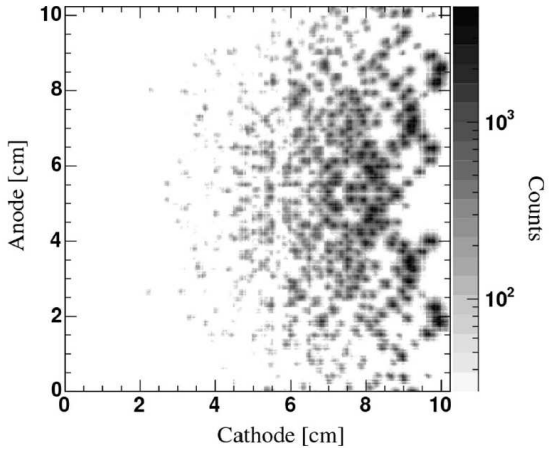

Figure 2.29: Raw image of diffraction from an organic crystal Ylid integrated over 3700 sec.

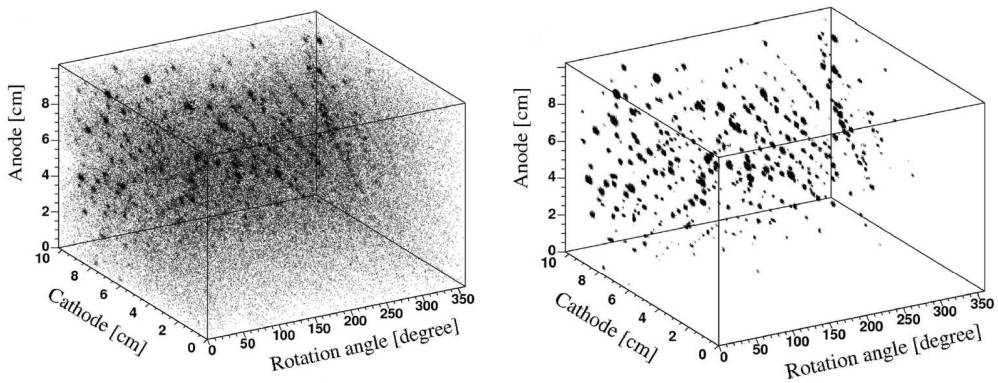

(a) (b)

Figure 2.30: X-ray diffraction from Ylid plotted in three-dimensional space. The diffraction pattern forms many three-dimensional clusters. (a)Raw data. (b)Data after background reduction.

Chapter 3

Performance characteristics of the μ-PIC detector for high-count rate environments

The development of the μ-PIC was originally motivated by an application as a Compton camera on board a satellite. The Compton camera consists of the micro-TPC surrounded by scintillators and the encoding system. An incident gamma-ray is scattered within the micro-TPC and the scattered gamma-ray is absorbed by the scintillator. Using the kinetics of the recoil electron and the scattered gamma-ray, the incident gamma-ray can be reconstructed. The camera aims at observations of cosmic gamma-rays for which counting rates are low. The encoding system for the X-ray area detector based on the μ-PIC described in the previous section shares the same idea to encode positions of signals with that of the Compton camera. This system is referred to as the classical system.

To adjust the encoding system to high-counting rate environments, some improvements of the system are necessary. In this section, first we will demonstrate the performance characteristics using the classical encoding system, point out its problems, and then show how the encoding system should be improved. New logic for encoding positions is also demonstrated in this section. We will also show the performance characteristics of the μ-PIC for high-counting rate environments investigated mainly in the RIKEN Structural Biology beamline I BL45XU at SPring-8, Japan. This beamline was designed for SAXS measurements.

3.1 Experimental setup

At the BL45XU, the photon flux can reach 10^{12} photons per second. A pair of four-blade slits was set in front of the sample to define the beam size. The beam intensity was adjusted using absorbers installed in front of the first slit. The beam size in front of the sample was a rectangle of 1.0 mm (horizontal)$\times$0.8 mm (vertical). A vacuum path shown in Fig. 3.1 was inserted between the sample and the detector to prevent from scattered X-rays by the sample interacting with the air and producing the background. At the end of the beam path, a polyimide window is arranged to keep inside the path under a vacuum and reduce an absorption loss. A beam-stopper is arranged on the window. The μ-PIC was set perpendicular to the X-ray beam and placed next to the polyimide window.

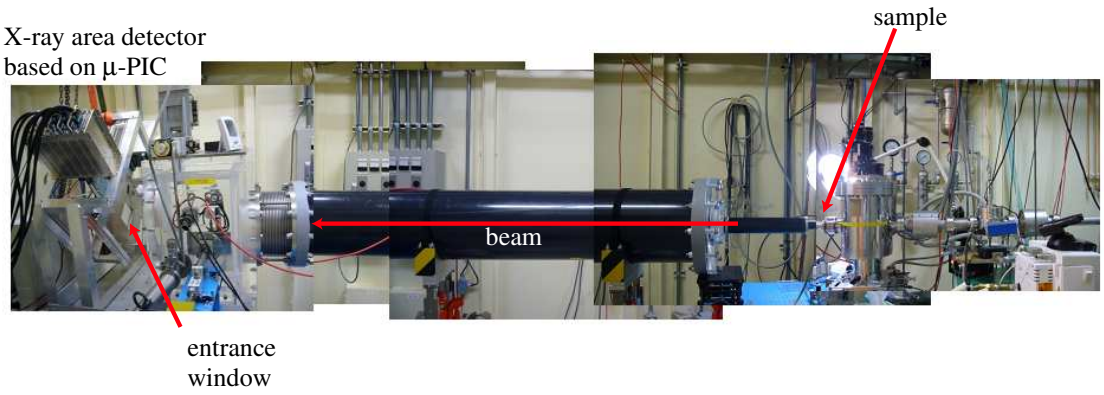

Figure 3.1: Overview of experimental setup in the RIKEN Structural Biology beamline I BL45XU at SPring-8, Japan.

3.2 Performance characteristic

3.2.1 Linearity

Linearity in local counting rates

Linearity of the μ-PIC in local counting rates was investigated [21]. The X-ray area detector without the GEM was locally irradiated with X-rays generated by an X-ray generator with a target of molybdenum (K_α : 17.4 keV). The gas gain was 2000. Linearity in an anode current was plotted as a function of counting rates in Fig. 3.2(a). A good proportionality to the anode current was maintained at a counting rate of up to 10 Mcps/mm^2.

Linearity in global data acquisition rates

The measurement described above was conducted to investigate the performance of the μ-PIC itself. The global data acquisition rate (DAR) of the encoding system must also be examined for the actual applications. This was studied at BL45XU at SPring-8 using SAXS from a piece of glassy carbon, whose scattering pattern is close to uniform. The camera length was set to 2200 mm. The wavelength of the X-ray beam was adjusted to 0.9 Å (13.8 keV). A 1 atm Xe-C_2H_6 (70:30) gas mixture was used as an absorber of X-rays. In this section, all experiments were conducted with this gas filling. The DAR was measured for a counting rate ranging from 20 cps to 5 Mcps. The anode current of the μ-PIC depends linearly on the beam intensity at the detector, as discussed above. Therefore, we compared the DAR and the leakage current of the μ-PIC to evaluate the linearity in the DAR.

The DAR and the anode current demonstrated a good linear correlation from 20 cps to 5 Mcps, as shown in Fig. 3.2 (b). The current limit of the high voltage supply module, which supplies current up to 10 mA, limits the DAR. The anode current limit was roughly equivalent to a DAR of 5 Mcps.

3.2.2 Distortion

In principle, micro-pixel gas detectors with strip-readout are free from an image distortion. It is one of advantages of these detectors. On the other hand, CCDs suffered from a strong distortion need corrections. In general the image of CCD-II includes an image distortion and a non-uniform

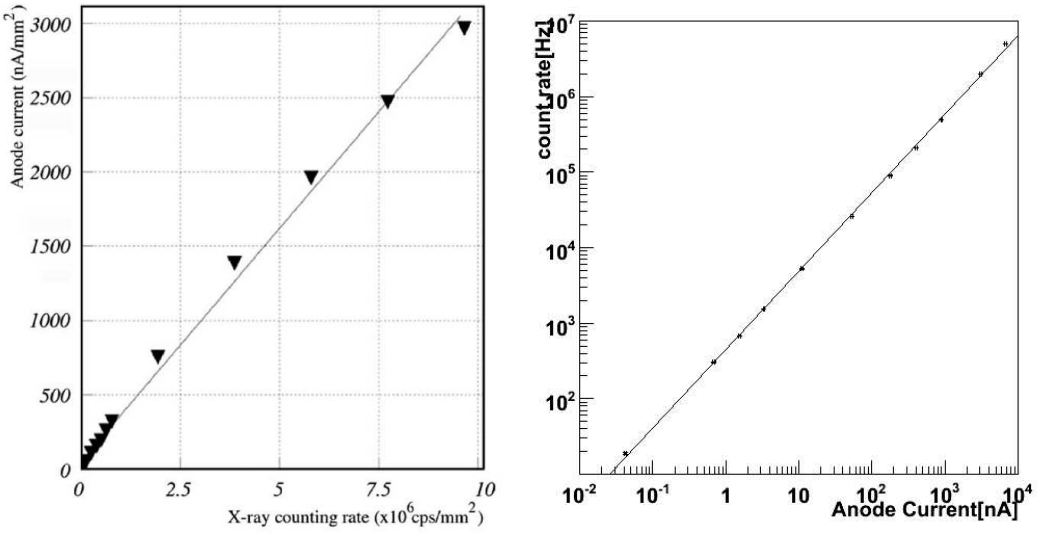

(a) Anode current as a function of the intensity of X-rays [21]

(b) Global data acquisition rates as a function of an anode current

Figure 3.2: Linearity in (a) local counting rates and (b) global data acquisition rates

response, due to the aberration of the electron lens in the Imaging Intensifier and the non-uniformity of the phosphor thickness.

Through measurements using the μ-PIC , a negligibly small distortion was detected in images of a grid mask. On the grid mask, holes were perpendicularly arranged at a constant interval. The entrance window of the μ-PIC was masked and irradiated with scattering from a piece of a glassy carbon. The wavelength of the X-rays was 0.9 Å (13.8 keV) and the camera length was 2200 mm.

Figure 3.3(a) and (b) show images of the grid mask observed by the μ-PIC . The global counting rates of (a) and (b) are 8 kcps and 200 kcps, respectively. For reference, an image of the mask shown in Fig. 3.3(c) was observed by a CCD in the same condition. One can see a strong distortion in Fig. 3.3(c). However, the differences in the distance of the holes, as observed by the μ-PIC were within 1% of the entire active area. The deviation from the perpendicular was < 1 degree. Moreover, the change in the image was negligible when the beam intensity was varied. The peaks observed at the holes on the mask moved 2-8 μm when the beam intensity was varied from 8 to 200 kcps. The change of 2-8 μm is negligible considering the pixel pitch of 400 μm. We concluded from these results that the strip readout and the coincidence of the strips caused no distortion. Even in the case of micro pattern gas detectors, an analogue position encoding method would distort images under moderate count rate environments due to their readout circuits. In the present evaluation, all image profiles were performed without correction for image distortion.

3.2.3 Dynamic range

We examined the dynamic range of a solution scattering curve decreasing exponentially as q increases. Figure 3.4 shows the scattering curve. The target is a polystyrene latex whose diameter is 120 nm. The wavelength of the X-rays was 0.9 Å (13.8 keV) and the camera length was 2200 mm. The scattering curve of the latex, approximated by a solid sphere, is expected to follow the power law of q^{-4}. A wide dynamic range of over 10^5 is obtained and the intensity clearly follows the power law of q^{-4}.

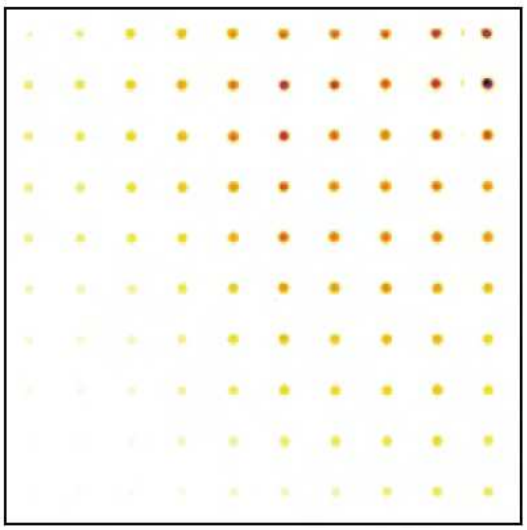

(a) μ-PIC (8 kcps)

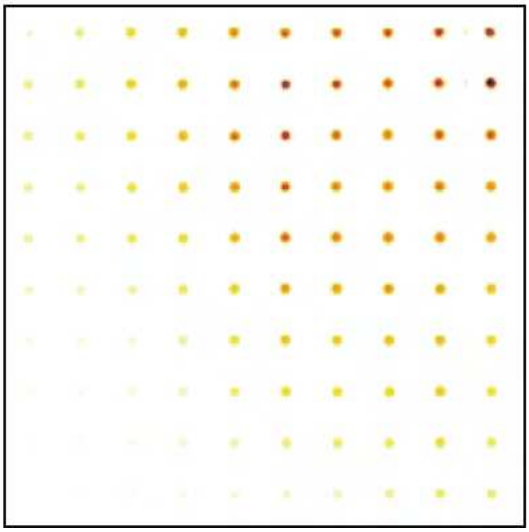

(b) μ-PIC (200 kcps)

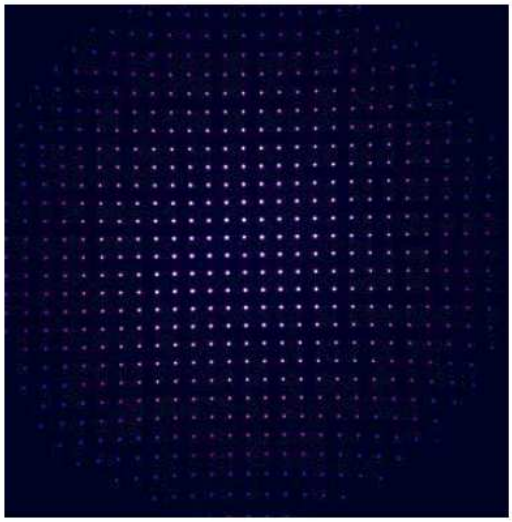

(c) CCD

Figure 3.3: (a)(b)Image of a grid mask. The entrance window of the μ-PIC was masked and irradiated with scattering from a piece of a glassy carbon. (c)Image of the grid mask recorded by a CCD.

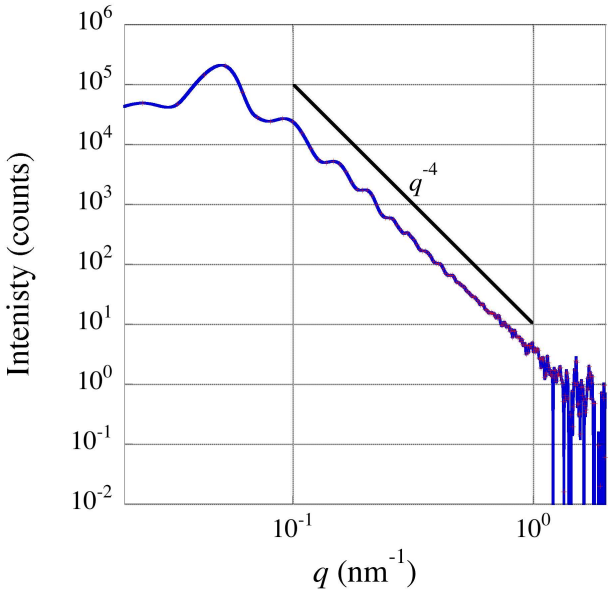

Figure 3.4: Solution scattering curve from polystyrene latex. The diameter is 120 nm. A scattering curve of the latex approximated by a solid sphere follows the power law of q^{-4}. The dynamic range of over 10^5 is obtained and the intensity clearly follows the power law of q^{-4}. The classical encoding system was employed.

3.2.4 Accidental coincidence

The strip readout of 256 ch + 256 ch simplifies the system. However, the encoding system needs to overcome difficulties in encoding the position in high-rate environments. The encoding system monitors the whole detector and finds coincident strips. Therefore, in high-rate environments where several X-rays are likely to arrive closely enough in time to pile up, the system often determines incorrect positions and thus produces a ghost image. Diffraction pattern images of an Au nano particle solution at a DAR of 120 kHz and 2 MHz are shown in Fig. 3.5. One can see the clear ghost image that consists of two rectangles crossing the beam center in Fig. 3.5 (a). The ghost image is not seen in Fig. 3.5 (b) that was obtained in the low counting rate environment. The incorrect calculations in high-counting rate environments occur as follows.

It is assumed that two X-rays arrive closely enough in time to pile up. Figure 3.6 demonstrates such events. One of the X-rays hits the μ-PIC at ($X1$, $Y1$) and the other at ($X2$, $Y2$). If $X1$ and $Y1$ coincide with the clock interval of $T1$, $X2$ and $Y2$ coincides with $T2$, and $T1 \neq T2$, two events are successfully recorded. When $X1$, $X2$ are synchronized with the same clock T and $|X1 - X2| > 8$, both events are discarded. If signals generated by the anodes and cathodes completely coincide, this encoding system works well and always records the correct coordinates. In this chapter, we refer to an analog signal generated by the ASD as just a 'signal' and a digital signal as a 'hit'. Since an electron liberated by an X-ray crosses a few μ-PIC pixel, a few signal and then a few hits are generated by the ASDs.

However, due to the time walk of the ASDs mentioned in the previous chapter, anode strips and cathodes strips occasionally fail to coincide. In the previous chapter, using signals obtained by a pulse generator, we proved that overall time walk was less than 2 ns when input charges are in the range of 0.05 pC to 2 pC. However, due to the slow rise of signals, that is tens of nanoseconds, generated by the μ-PIC , the time walk would increase when the ASDs are connected to the detector. In addition, the low threshold of 0.01 pC makes the situation worse.

Figure 3.7 shows oscillograms of discriminated signals and analog output of the ASDs. Discrim-

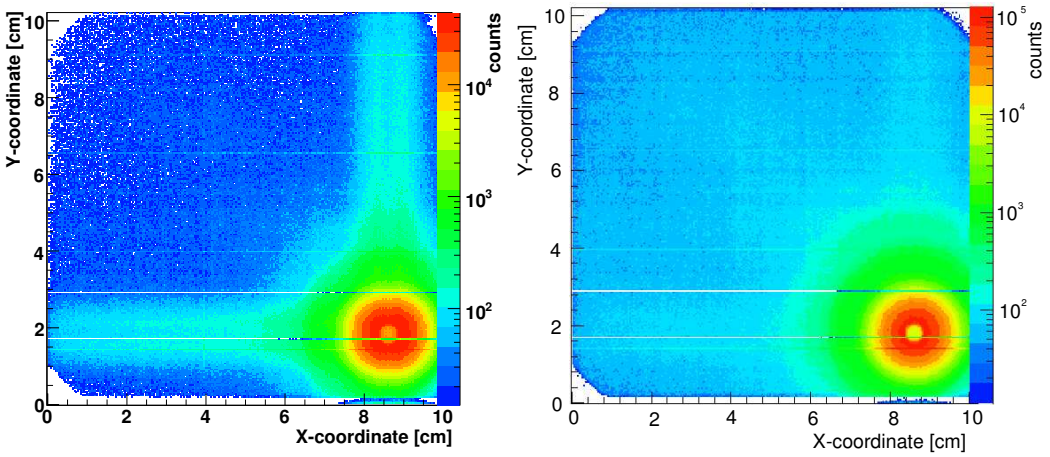

(a) At a DAR of 2 MHz

(b) At a DAR of 120 kHz

Figure 3.5: Diffraction pattern images of an Au nano particle solution at a DAR of 120 kHz and 2 MHz. Ghost induced by accidental coincidence can be clearly seen in (a). The classical encoding system was used.

inated signals from anode strips were ORed together. Discriminated signals from cathode strips were also ORed together. The 32-channel summed analog output in the Fig. 3.7 (b) shows that the signals sent from the anodes have the different waveform from those from the cathodes. The difference in the waveform is due to the ASDs, whose performance is different for positive and negative inputs. Given the difference in rising time constant of the anodes and cathodes, 20 to 30 % hits fail to coincide. It should be noted that a capacitor of 1μF connects the analog output and a ground in order to reduce noise. The sloping rise and fall at the analog output is caused by the capacitor. Since an X-ray photon usually deposits its energy on only a few strips, anodes and cathodes produce few signals. Due to the timewalk of the ASDs, not all discriminated signals of the anodes and cathodes are in coincidence. In the worst case such as Fig. 3.7(c), all hits fail to coincide and thus the incoming X-ray is not detected though the pulse height is well above the threshold.

In high-counting rate environments, strips failing to coincide properly are likely to coincide with other strips generated by other X-rays. For instance, $X1$ and $Y2$ coincide in accident and an incorrect coordinate of ($X1$, $Y2$) is recorded. Many such incorrect results form the ghost and distort the image. In SAXS, most X-rays concentrate on the area close to the beam center. Therefore, accidental coincidences involving an X-ray hitting close to the beam center are most likely to be observed. When both of the two X-rays are observed near the beam center within an interval of tens of nanoseconds, the resultant positions are likely to be wrong and would cause an image distortion there, but do not contribute to the ghost image. When two X-rays hit the μ-PIC within an interval of tens of nanoseconds and one is around the beam center and the other is apart from the center, they are likely to contribute to the ghost image. In this case, the $X = X1$ or $Y = Y2$ cross the region close to the beam center and the other coordinate ($Y = Y2$ or $X = X1$) ranges in the whole detector. Therefore, the ghost image forms a cross.

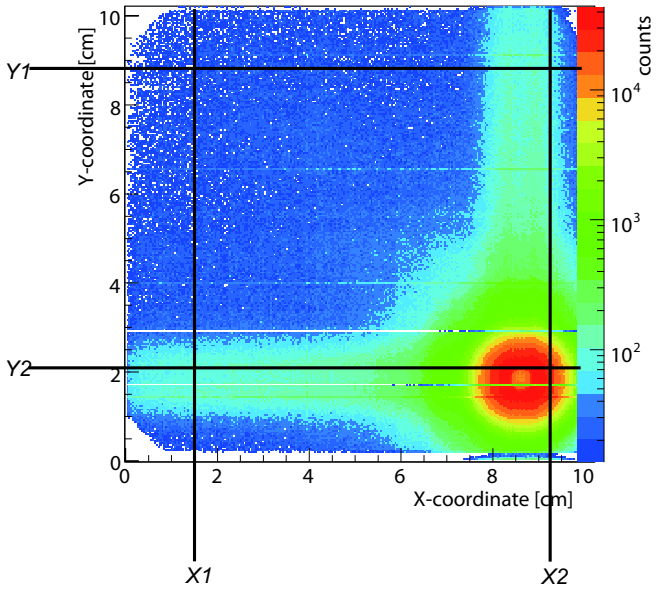

Figure 3.6: Diffraction pattern image of an Au nano particle solution at a DAR of 2 MHz. The classical encoding system was used. Two X-rays hit at ($X1$, $Y1$) and ($X2$, $Y2$) close enough in time to pile up. Due to the timewalk of the ASDs, $X1$ and $Y1$ occasionally fail to synchronize with the same clock T of the encoding module. Alternatively, $X1$ and $Y2$ coincide in accident and an incorrect position of ($X1$, $Y2$) is recorded.

3.3 X-ray detection efficiency with position encoding system

In the previous section, we showed that the encoding system sometimes fails to detect X-rays though the pulse heights are well above the threshold. Then, X-ray detection efficiency was examined and the result is shown in Fig. 3.8. The vessel containing the detector was filled with a Xe-C_2H_6 (70:30) gas mixture and was irradiated with ^{109}Cd (22.2 keV, 24.9 keV). In this experiment, the ASD reference threshold voltage was set to $\pm$23 mV, 64-cathode strips were ORed, and the analog and digital output was monitored.

The numbers of hits (digital signals) generated by the cathodes were shown as a function of pulse height of the 64-channel ORed analog output in Fig. 3.8. X-rays generated by ^{109}Cd emit copper fluorescent of 8 keV when they interact with the copper electrodes of the μ-PIC . Thus a wide range of X-rays can be obtained. The ratio of the hits having coincident hits generated by the anodes (256 channels) was also determined. Hits sent from the anodes were measured in the same way.

From these measurements, it is concluded that most hits are lost because of the failure of coincidence. An X-ray generates a few hits and thus the ratio of the lost X-rays is about 50 %. In high-rate environments, the ratio of the lost hits is expected to be almost the same because the detector system maintains linearity up to 5 MHz. The count loss is slightly decreased by the accidental coincidence as counting rates increase. However, it mainly depends on the time walk characteristics of the ASDs. To avoid the count loss, all hits should be taken into account even if they do not synchronize to any other hits. We will discuss such a method in subsequent sections.

It should be noted that the number of digital generated by the cathodes is larger than that generated by the anodes because the threshold supplying the cathodes is higher than that supplying the anodes. Since the minimum threshold level is dictated by the noise level that strongly depends on the environment, the threshold level needs to be well-adjusted every time the environment

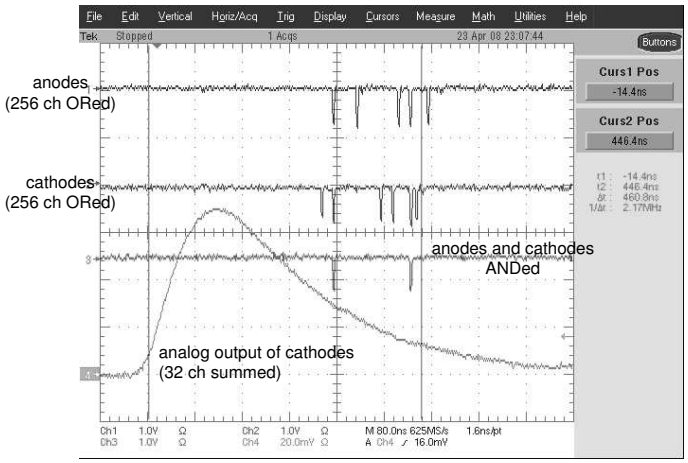

(a)

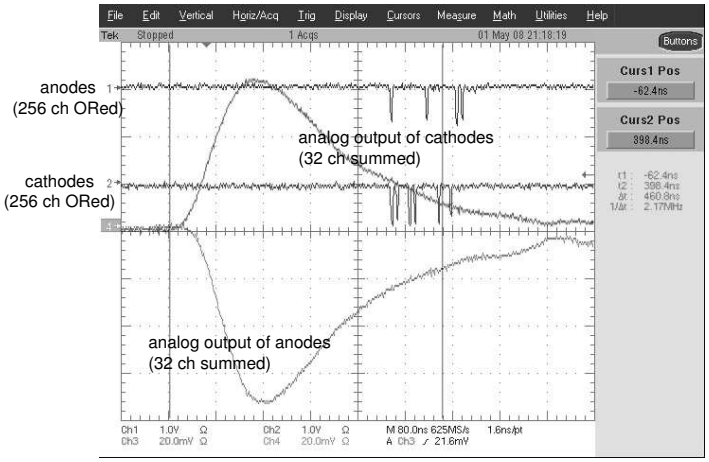

(b)

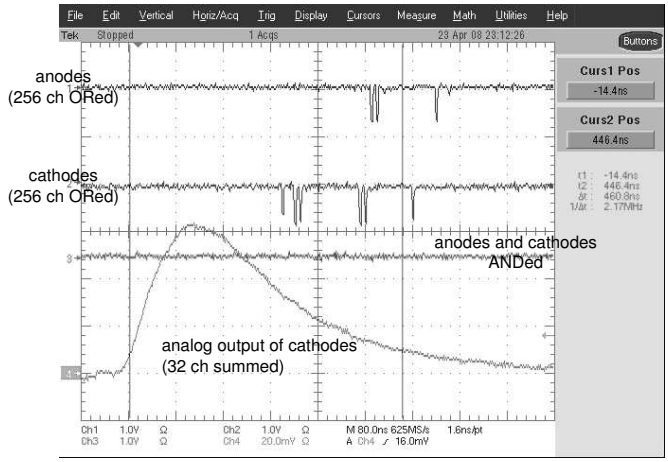

(c)

Figure 3.7: Discriminated signals and analog output of ASDs. Discriminated signals from anode strips were ORed together. Discriminated signals from cathode strips were also ORed together. Not all discriminated signals of anodes and cathodes are in coincidence. Oscillograms also show 32-strips summed analog output.

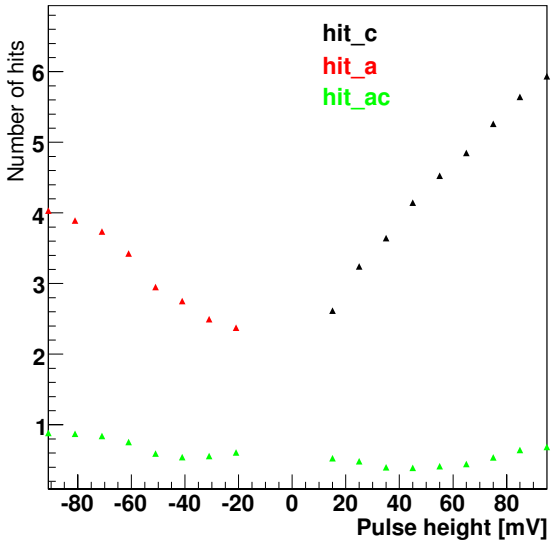

Figure 3.8: X-ray detection efficiency. Numbers of hits (digital signals) generated by the anodes and cathodes per photon, hit_a, hit_c are plotted as a function of pulse height at analog output. Ratio of hits (digital signals) having coincident ones, hit_{ac} is also shown.

changes.

3.4 New position encoding method (mode-II)

In this section, improvements in the position encoding method will be discussed. From now, we will refer to the classical encoding method as mode-I and the new method mentioned in this section as mode-II. Figure 3.9 shows a block diagram of the mode-II position encoding system. Mode-II allows one to record all hits. On the other hand, mode-I only records hits from the anodes and the cathodes when they coincide in a clock interval (10 ns). One can easily load new files to the FPGAs which are components of the position encoding system, and then the new logic of the system can be used. According to Fig. 3.8, the data acquisition rate doubles using the mode-II.

The number of generated hits strongly depends on the energy of the X-rays, the gas gain, and gains of the ASDs. In the case of an X-ray photon of 8 - 13.8 keV available at SPring-8, it generates 0 to 2 pairs of the hits which coincide within in a clock interval. We integrated the resultant hits and obtained two-dimensional images shown in the previous sections.

The uniformity of the μ-PIC is quite good at about 5 % RMS. However, the low threshold level of 25 mV (corresponding to 3.6 mV at the comparator input) supplied to the ASDs is in a region where input charges are very sensitive to propagation delay at the comparator output. The propagation delay is the main reason for the counting loss. Thus, the small gain variation leads to non-uniformity of the signal detection efficiency.

Figure. 3.10 shows an approximately uniform illumination, the scattering pattern image of glassy carbon, whose scattering curve declines gentle. The encoding system used was mode-I. The non-uniformity can clearly be seen in Fig. 3.10. The many vertical and horizontal lines are due entirely to the gain variation of the ASDs.

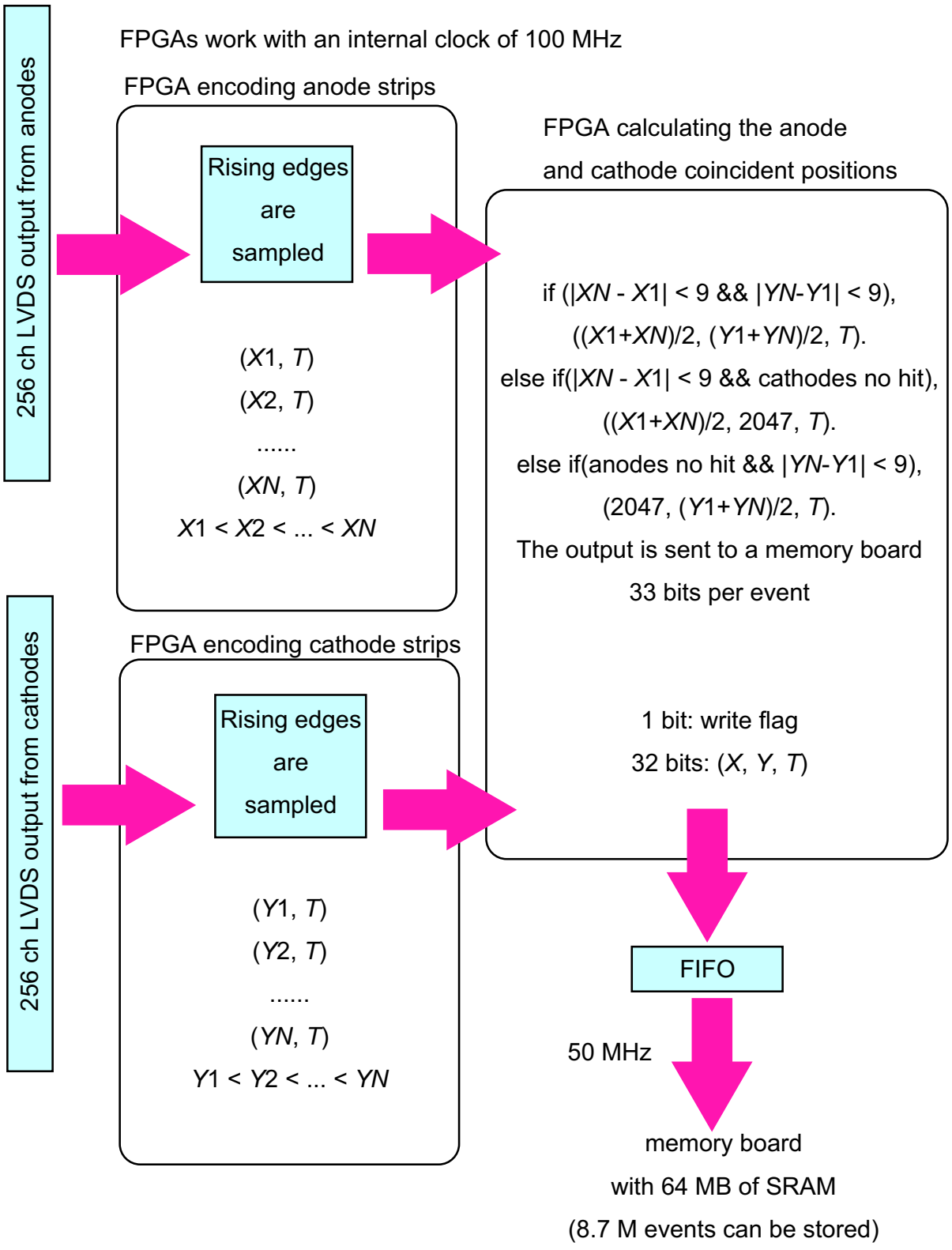

Figure 3.9: A block diagram of the mode-II position encoding system

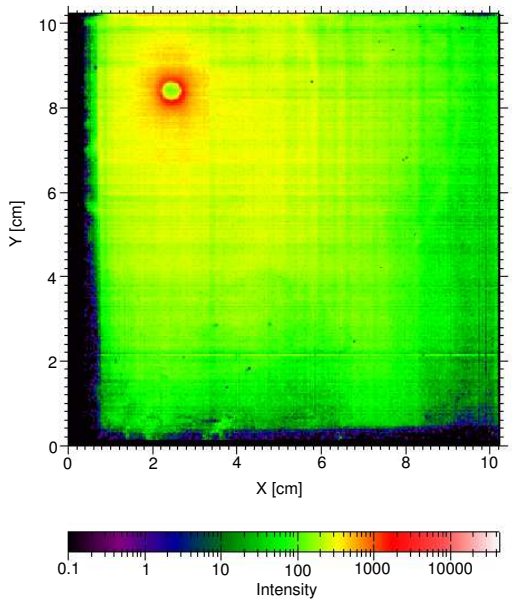

Figure 3.10: Raw scattering pattern image of glassy carbon. The sample was irradiated with 0.9 Å (13.8) X-rays at BL45-XU SPring-8. The mode-I encoding system was employed.

3.4.1 Two-dimensional images obtained by mode-II

In mode-I, hits generated by an X-ray are recorded and integrated to obtain a two-dimensional image. The recorded hits are the projection of the electron track liberated by the X-ray photon to the μ-PIC detector plane. Thus, the two-dimensional image obtained is the integration of the electron tracks. Considering the gas diffusion (the diffusion coefficient of 210 $\mu\mathrm{m}\sqrt{\mathrm{cm}}$) and the range of the electrons, this method deteriorates the position resolution. Moreover, the number of hits generated by an X-ray photon depends on the gain of the gas detector and the ASDs. Thus the integration of the electron tracks emphasizes non-uniformity of the system.

To improve these problems, in addition to mode-II, the calculation of the positions of the X-rays was improved. An X-ray generates several hits. Instead of integrating all the hits, the averaged position of the hits is calculated. Since hits generated by an X-ray form a cluster, the averaged time of the anode and the cathode clusters is refered. When the time difference is less than 100 ns, they make an anode-cathode pair. This method improves the position resolution because the diffusion that follows a Gaussian distribution is compensated. The averaged positions are filled in a two-dimensional histogram and the image can be obtained. This method is independent of the gain variations while an X-ray generates at least two hits, one by the anodes and the other by the cathodes.

To eliminate incorrect position calculations, we used X-rays which had no possibility of pile-up. When the arrival time difference between two X-rays is less than 200 ns, they are likely to pile up, considering the time constant of the ASDs. Therefore, these X-rays are removed in the off-line analysis. We refer to this cut as a pile-up cut.

For the evaluations of the mode-II position encoding systems, described in this section, we used a solution scattering patterns from SiO_2 nano particles and from Apo-Ferritin that is a protein. The diameter of the SiO_2 particles is 100 nm. These samples were irradiated with 1.5 Å (8 keV) X-rays at BL45-XU SPring-8. The intensity of the X-ray beam in front of the samples was 1.5×10^{10} that is almost the same as the intensity of the beam used for the IPs. The camera length was set to 2167 mm. Figure 3.11 shows solution scattering patterns from SiO_2 nano particles. Since a data acquisition rate was high (6.3 MHz), a ghost image can be clearly seen in Fig. 3.11(a). The ghost

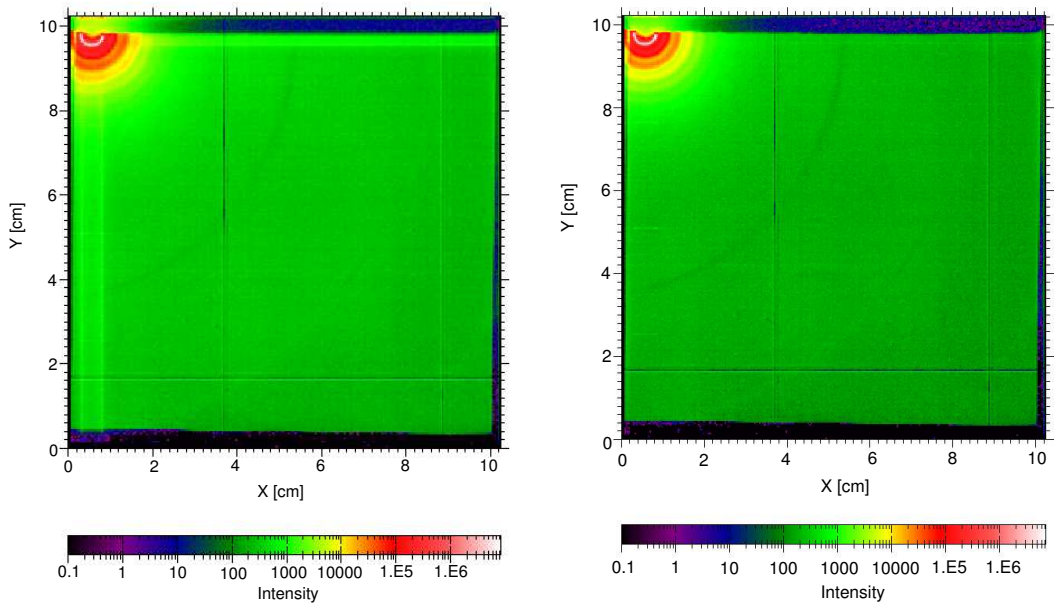

(a) (b)

Figure 3.11: Solution scattering patterns from SiO_2 nano particles. The diameter is 100 nm. The data was collected by the mode-II encoding system. The sample was irradiated with 1.5 Å (8 keV) X-rays at BL45-XU SPring-8. (a)We caluculated the average the positions of the hits generated by the X-rays but did not applied pile-up cut. A ghost image crossing a beam center can be clearly seen. (b)The ghost image vanished when applying a pile-up cut.

image vanished after applying the pile-up cut.

Figure 3.12(a) and (b), produced using the same data show a solution scattering pattern from Apo-Ferritin. In Fig. 3.12(a), all the events with the anode and cathode hits in the same clock (= 10 ns) are filled in a histogram. In Fig. 3.12(b), the averaged positions of the hits are calculated and the pile-up cut was applied. In Fig. 3.12(a) there are many vertical and horizontal lines while Fig. 3.12(b) is quite smooth. Two clear valleys are seen between the intense rings in Fig. 3.12(b). Thus, the combination of the mode-II encoding system and the calculations of the averaged positions of the hits drastically improve the detection uniformity and enhance the quality of X-ray images.

3.4.2 Aging behavior in high-counting rate environment

X-ray area detectors for use at third-generation synchrotron radiation sources must be resistant to damage caused by intense X-rays. The detectors are also required to confirm linearity and stability during a long duration radiation.

Environments with high levels of X-ray radiation create special design challenges of the μ-PIC . In the case of the μ-PIC , after radiation with intense X-rays, the gas gain in the area around the beam center drops permanently. An area irradiated with a strong scattering peak shows the same feature. In Fig. 3.12(b), a small ring ($(X, Y) = (3.5, 7.5)$) which corresponds to an area damaged by intense X-rays distributing around the beam center can be seen. Figure 3.12(b) also shows the drop in gain caused by two strong scattering peaks which had been observed before this measurement.

In principle, the small drop in the gain does not affect the detection efficiency when all signals generated by X-rays are counted by the detector system. For the data presented in Fig. 3.12, the

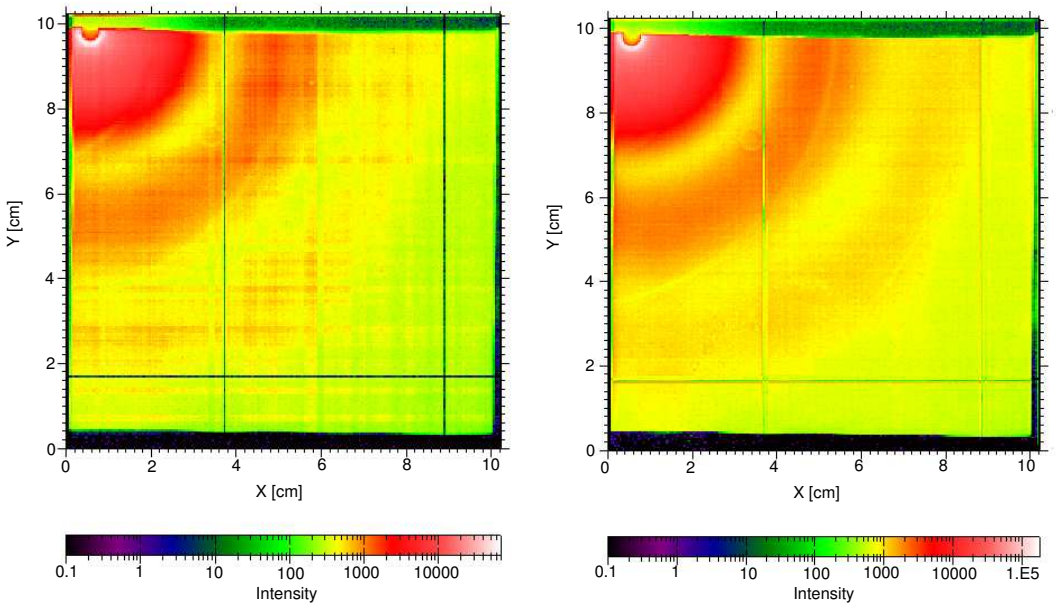

(a) (b)

Figure 3.12: Solution scattering pattern image of Apo-Ferritin. The sample was irradiated with 1.5 Å (8 keV) X-rays at BL45-XU SPring-8. Plots (a) and (b) use the same data set. (a)Events having the anodes and the cathodes hit in the same clock (= 10 ns) are integrated. (b)All events are analyzed on the basis of mode-II.

common reference threshold voltage supplied to each of the ASD chips is still high and the detector failed to detect a part of X-rays hitting the damaged area, which do not exceed the threshold. This can be avoided by applying the lower threshold. Therefore, it is important to improve signal-to-noise ratio.

The easiest way to obtain the fine signal-to-noise ratio is to raise the gas gain by installing another GEM above the current one. However, when the amount of electrons amplified by the μ-PIC is large, they would damage the surface of the μ-PIC . Thus, it is important to reduce the noise level. The extension board connecting the μ-PIC with the ASDs mainly contributes to the noise problem because its connection to the ground level is weak and the length is too long. We are developing a new extension board and will place readout circuits closer to the μ-PIC .

Another solution to this problem is to remove the ethane gas and use another kind of a quencher gas such as CO_2. Intense X-rays allow hydrocarbon families to form larger complexes (polymerization), which pile on the electrodes of the μ-PIC . The polymers could change the electric field around electrodes and reduce the gas gain. Instead of the hydrocarbon families, inorganic compounds like CO_2 or CF_4, which has more radiation-hardness , should be added.

3.4.3 External trigger

Since the intensity of the X-ray beam occasionally fluctuates, it must be monitored during a measurement by a reliable detector such as an ion chamber. To conduct a precise measurement of the intensity of scattered X-rays, the X-ray area detector should synchronize with the monitoring detector, using, for example, a common gate signal. Then, we improved the encoding system by allowing it buffer data in the FIFO only while receiving the gate signal.

3.4.4 Solution scattering measurement

With the gating and the introduction of the mode-II position encoding system, solution scattering patterns were measured at SPring-8. A solute scattering curve is determined by subtracting the solvent curve from the solution curve. Since their exposure times are sometimes different, the scattering curves are corrected by the integrated intensities of incoming photons. Another correction to derive the correct solute scattering curve is for the pile-up cut.

In principle, the ratio of discarded events depends on the data acquisition rate because a probability of pile-up depends on it. The data acquisition rate is different between the solution and the solvent scattering measurements. Thus, a correction for the ratio of the discarded events is significant.

Then, the scattering curve without applying the pile-up cut was divided by the one with the cut. The resultant curve shown in Fig. 3.13 is almost flat except in the region shaded by the beam stopper. The correction coefficient for the pile-up cut C_p is the constant values of these curves.

Taking the corrections into account, the solution scattering curve must be multiplied by $(C_p)_{\rm solvent}/(C_p)_{\rm solution}$. The subtraction of scattering curves is sensitive to the correction coefficient and thus careful measurements and calculation are required. A 1%-deviation of C_p disturbs a wide angle region where the difference between the solution and solvent is quite small.

The resultant scattering curve is shown in Fig. 3.14 (c). It almost agrees with the scattering curve measured by an IP as reference while (a) apparently deviates from the reference. Plots (a), (b) and (c) used the same data set. In the case of (a), hits from the anodes and the cathodes when they coincide in a clock interval (10 ns) are used (equivalent to the mode-I). The peaks and the valleys shown in Fig. 3.14(a) deviate from those obtained using the IP. The mode-I encoding system caused the non-uniformity of the X-ray detection efficiency and thus the profile of the solution scattering is slightly changed. The solute scattering curve determined by subtracting the solvent curve from the solution curve is very sensitive to this change. Fig . 3.14 (b) shows the plot without the pile-up cut. The plot almost agrees with the reference but the deviation from it is larger in the wide-angle region in comparison with Fig. 3.14 (c). Table 3.1 summarizes the results of the analysis of solution scattering from an Apo-Ferritin.

Figure 3.15 shows the intensity difference between the μ-PIC and the IP (R-Axis). The scattering patterns from Apo-Ferritin shown in Fig. 3.14(c) were used for the evaluation. The degree of difference, $100(I_{\mu\text{-PIC}})(q) - I_{\rm IP}(q))/I_{\rm IP}(q)$ [%], is shown on the y-axis. Since the scattering patterns of the μ-PIC and the IP are consistent in the small-angle region, the intensity of the IP is normalized to that of the μ-PIC using an averaged intensity in a range of $0.1 \leq q \leq 0.15$ [nm^{-1}]. The reason why the difference in the wide-angle region is especially large is the non-uniformity of the detection efficiency for X-rays. The drift plane located above the μ-PIC would be slanted slightly. The slanted plane leads to the non-uniformity of the thickness of the gas layer and thus of the detection efficiency.

Figure 3.16 shows solution scattering curves from SiO_2 nano particles. Plots (a), (b) and (c) used the same data set. In the case of (a), hits from the anodes and the cathodes when they coincide in a clock interval (10 ns) in the same clock (= 10 ns) were used (equivalent to the mode-I). Recall that the scattering curve of the particles approximated by a solid sphere follows the power law. The curve shown in Fig. 3.16 (a) approximately follows the power law of q^{-4} but the exponent changes at $q \sim 0.6$ [nm^{-1}]. In the wide-angle region, the count loss due to the accidental coinciden is significant because the difference between the solution and the solvent curve is very small. The counting rate of the solution scattering is higher than that of the solvent scattering and thus the count loss is larger. Therefore, the solution curve shown in Fig. 3.16 (a) would have more counts. The plot shown in in Fig. 3.16 (b) also has the count loss for the same reason and thus the pile-up cut is necessary to obtain the correct curves. The dynamic range of solute scatterings shown in Fig. 3.16 (c) was widened by introduction of mode-II and the intensity clearly follows the power law of $q^{-3.7363}$. The scattering curve deviates from the power law of q^{-4} because the particles are not

Table 3.1: Results of an analysis of solution scattering from Apo-Ferritin and water are summarized. 'Events (mode-I)' represents the number of hits from the anodes and the cathodes when they coincide in a clock interval (10 ns). A few hits are generated by an X-ray. 'After analysis' represents the number of the X-rays hitting the detector. These two numbers do not need to be the same but agree by accident in this case.

Apo-Ferritin		
Exposure time	473.63737 sec	
Events (total)	724,820,905	
Data acquisition rate	1.530328 MHz	
Hits (mode-I)	137,616,751	(18.9863%)
After analysis	137,588,418 photons	(18.9824%)
Counting rate of X-rays	290.493 kHz	

Water		
Exposure time	405.06771 sec	
Events (total)	290,734,627	
Data acquisition rate	717.743 kHz	
Hits (mode-I)	55,642,762	(19.1387%)
After analysis	55,630,853 photons	(19.1346%)
Counting rate of X-rays	137.337 kHz	

perfect spheres. The difference between the solute scattering and the power law $q^{-3.7363}$ is shown at the bottom. It shows that the detector follows the power law in a range of over 10^6 and thus maintains linearity there.

Obviously, the X-ray area detector based on the μ-PIC has attained the widest linearity in solute scattering. This range exceeds that provided by the MSGC. Well-tuned IPs have a dynamic range of about 10^6 but the solute scattering curves determined by subtracting the solvent curve from the solution curve only maintain linearity in a range of about 10^5. This implies that the accuracy of the X-ray intensity measured by the IPs is limited to 10^{-5} by the internal background such as readout noise. On the other hand, the solute scattering curve measured by the μ-PIC has a 10 times wider dynamic range. Thus the detector system proves that the accuracy of X-ray counts is better than 10^{-6}. This high accuracy was attained because the detector is free from the internal background and the statistical uncertainty is dominant. The μ-PIC proved that it has the key features of the photon-counting detectors. The high accuracy of the μ-PIC allows to measure weak diffraction spots and scattering pattern precisely and will lead to high-precision measurements.

The PILATUS is also a photon-counting detector and has the same feature as the μ-PIC . However, the dynamic range of the 20-bit counter that each pixel comprises is 10^6 while that of the μ-PIC is infinite. Theoretically the 20-bit counter limits that of solute scattering curves obtained by a single frame to 10^6. To use a larger-bit counter, the pixel structure needs renewal and it requires a long-term development. Thus, the measurements must be repeated to achieve a wider dynamic range.

3.4.5 Guinier plot

According to equation (1.7), the gyration R_g can be obtained from the Guiner plot. A part of the data in Fig. 3.14 (b) is plotted in Fig. 3.17. The interval is limited to the region where $qR_g <\sim 1$ where the Guinier approximation is valid. Since the IP has a finer position resolution, it has more

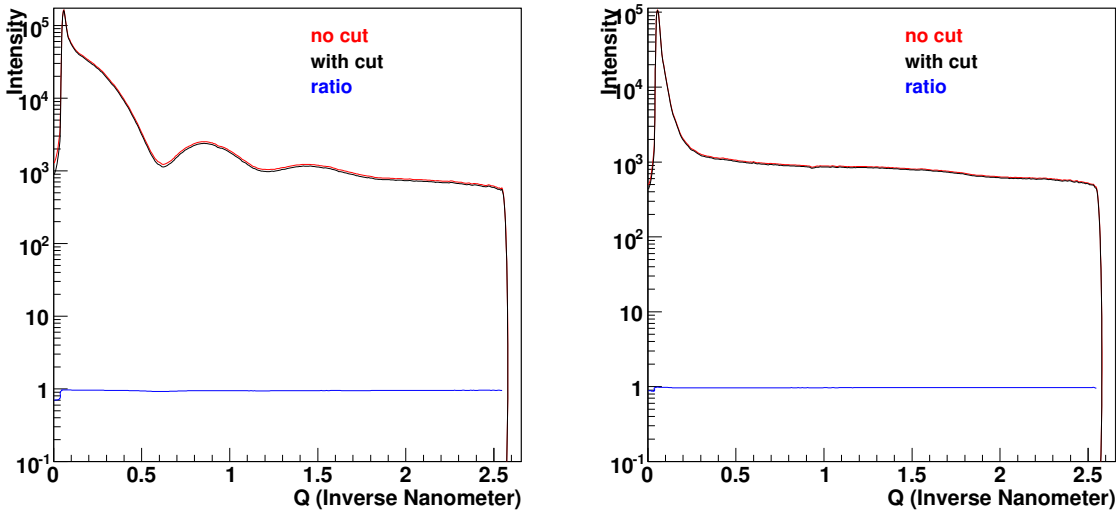

(a) (b)

Figure 3.13: Scattering curve without applying the pile-up cut is divided by one with the cut. (a) shows scattering curves from an Apo-Ferritin solution and (b) shows those from a water. The samples were irradiated with 1.5 Å (8 keV) X-rays at BL45-XU SPring-8. The whole detection area of the μ-PIC was used to obtain the scattering curves.

data in the very small angle region of $q < 0.05\text{nm}^{-1}$ and thus the small error of the gyration. The gyration obtained by the μ-PIC was 5.357 ± 0.006 nm while the gyration obtained by the IP was 5.320 ± 0.031 nm. Considering the errors, the gyrations derived by the μ-PIC and the IP seem consistent.

3.5 Further improvements of position encoding method (mode-III)

The new position encoding method, mode-II, improved the performance of the detector system in terms of linearity, uniformity, accidental coincidence, and counting loss. However, there is a room for further improvements because a new parameter, a pulse width of a hit, is available. The hits having maximum and minimum coordinates sampled in a clock interval (10 ns) are considered and the average of them is recorded by the mode-I and mode-II encoding system. Thus, the hits placed between the maximum and minimum coordinates are neglected. However, it is necessary to use all hits to calculate the averaged position. Thus, mode-III that is an improved version of mode-II and can measure pulse widths was developed.

Figure 3.18 shows a block diagram of the mode-III position encoding system. The mode-III system records both leading edges and falling edges of the hits (the digital signals) of the ASDs and thus the widths of the hits can be measured. If two or more ASD channel generate hits within a clock of 10 ns, positions of all the channels are recorded. The pulse heights of each channel can be deduced from the widths. Therefore, this method also allows one to find a centroid of the charge distribution and then improve the position resolution.

Figure 3.19 shows hits and their widths generated by 1.5 Å (8 keV) X-rays produced at SPring-8. Since the charges concentrate in the center of the electron cloud, strips located in the center

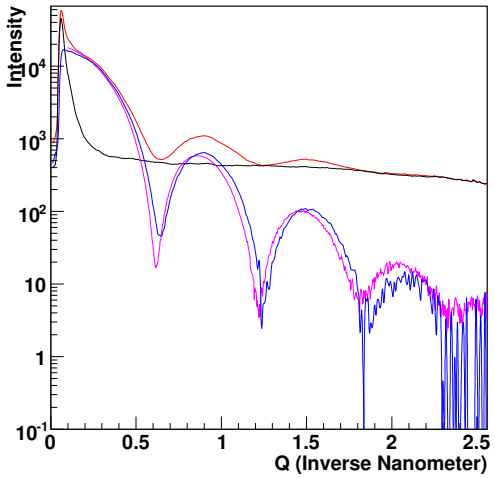

(a) Mode-I

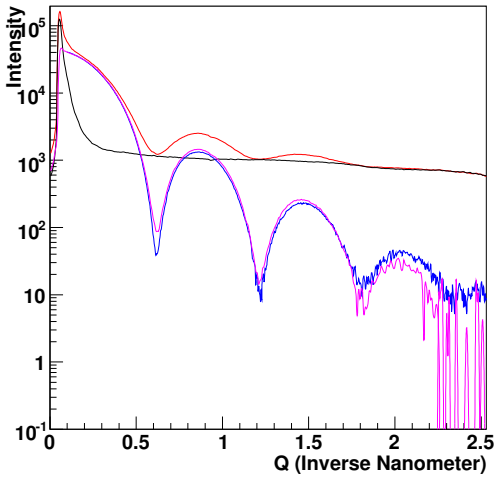

(b) Mode-II without the pile-up cut.

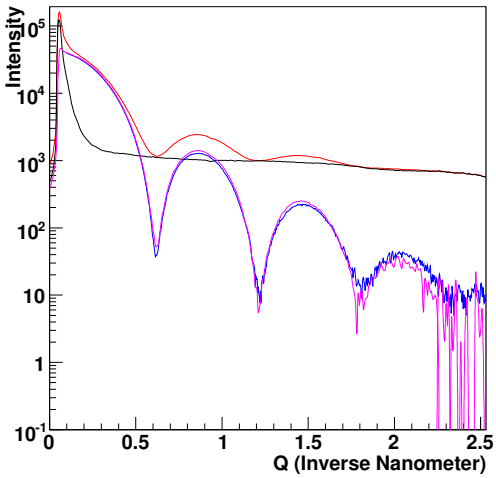

(c) Mode-II

Figure 3.14: Solution scattering patterns from Apo-Ferritin. The samples were irradiated with 1.5 Å (8 keV) X-rays at BL45-XU SPring-8. The red, black, blue, pink lines refer to a scattering curve of the solution, a solvent (water), their subtraction, and a scattering curve measured by IP (R-Axis) for reference, respectively. Plots (a), (b) and (c) used the same data set obtained by the mode-II encoding system. In the case of (a), hits from the anodes and the cathodes when they coincide in a clock interval (10 ns) are used (equivalent to the mode-I). (b)An X-ray generates a few hits and their averaged position is used. The pilse-up cut was not applied. (c)An X-ray generates a few hits and their averaged position is used. The pile-up cut was applied.

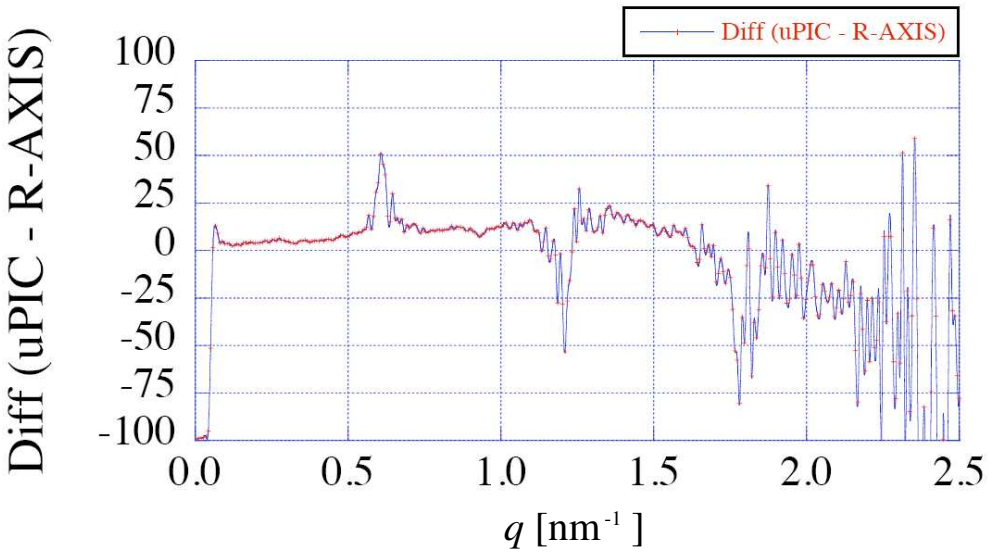

Figure 3.15: Intensity difference between the μ-PIC and the IP (R-Axis). The scattering patterns from Apo-Ferritin shown in Fig. 3.14(c) were used for the evaluation. $100(I_{\mu\text{-PIC}})(q) - I_{\text{IP}}(q))/I_{\text{IP}}(q)$ [%] is shown on the y-axis. The intensity of the IP is normalized to that of the μ-PIC using an averaged intensity in a range of $0.1 \leq q \leq 0.15[\text{nm}^{-1}]$.

have long pulse widths and cross the threshold first. Hits generated by strips surrounding the center usually have short pulse widths and follow the signals generated at the center. This feature suggests that the entire electron cloud arrives at the μ-PIC at almost the same time. The observed propagation delay occurs due to the time walk of the ASDs. It should be noted that electrical noise has short length of less than a few clocks while most of the hits have lengths of more than 5 clocks. Considering the features of the signals generated by X-rays and the electrical noise, it is easy to separate noise and signal.

Since the mode-III system has been constructed without ADCs, it is simple and easy to handle. The encoding system was upgraded by loading new files to the FPGAs. On contrary, RAPID uses the fast ADCs with necessity of cooling water and the detector system is complex.

The mode-III system could reduce the possibility of making noise and signal pairs. A counting rate of noise-noise pairs can be examined by recording the output of the μ-PIC in the absence of radiation. In this way, the rate for noise-noise pairs was seen to be several Hz and thus is negligible. In high-counting rates environments, the possibility of making noise-signal pairs is small but their contribution to non-linearity is considerable. Our next goal is to achieve a wider dynamic range of 10^{6-7} and thus making noise-signal pairs should be avoided. By considering the widths of hits and the number of hits, noise will be eliminated and the dynamic range will be enhanced.

3.5.1 Position calculation

Now we assume that the shape of the analog output is a triangle whose length of the base, W_0, is independent of its height. while its height h, is proportional to the input charge. The definition of the parameters is shown in Fig. 3.20. The pulse width of the digital output, W, is then expressed by

$$W = W_0 \frac{h - V_{\text{th}}}{h} \tag{3.1}$$

where V_{th} is the threshold voltage. A simple calculation gives

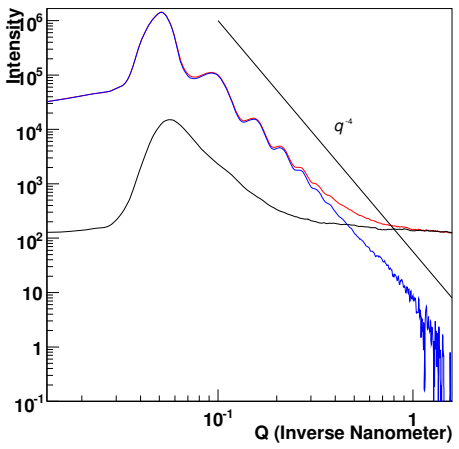

(a) Mode-I

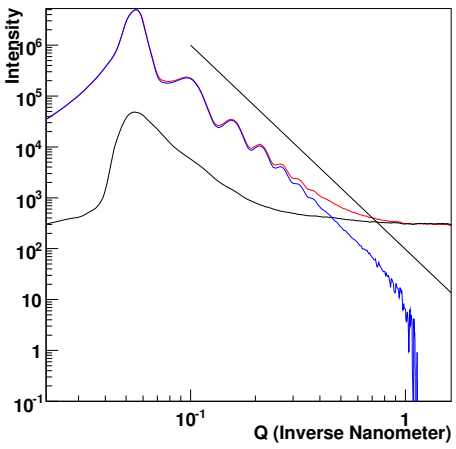

(b) Mode-II without the pile-up cut.

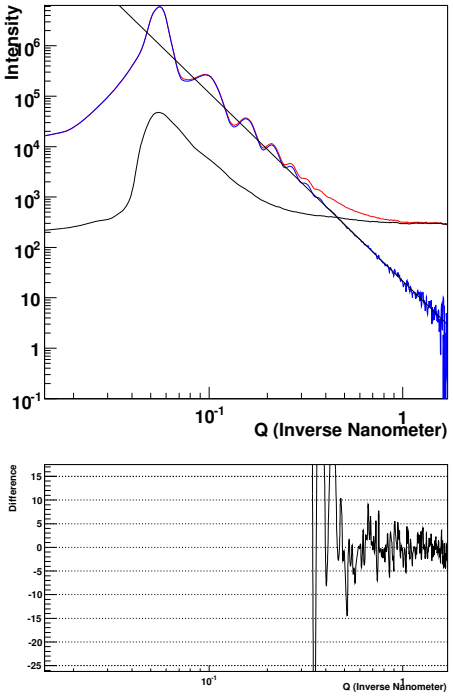

(c) Mode-II

Figure 3.16: Solution scattering curve from SiO_2 nano particles. The diameter of the particles is 100 nm. The red, black, and blue lines represent the scattering curve of the solution, the solvent (water) and their subtraction, respectively. The samples were irradiated with 1.5 Å (8 keV) X-rays at BL45-XU SPring-8. A scattering curve of the latex approximated by a solid sphere follows the power law of q^{-4}. Plots (a), (b) and (c) used the same data set. In the case of (a), hits from the anodes and the cathodes when they coincide in a clock interval (10 ns) are used (equivalent to the mode-I). (b)An X-ray generates a few hits and their averaged position is used. The pile-up cut was not applied. (c)An X-ray generates a few hits and their averaged position is used. The pile-up cut was applied. The difference between the solute scattering and the power law is shown at the bottom.

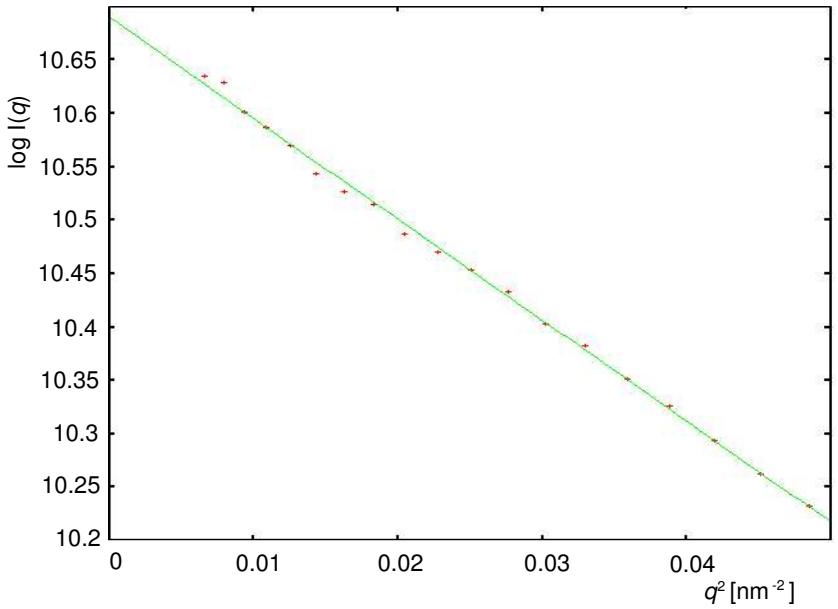

(a) μ-PIC

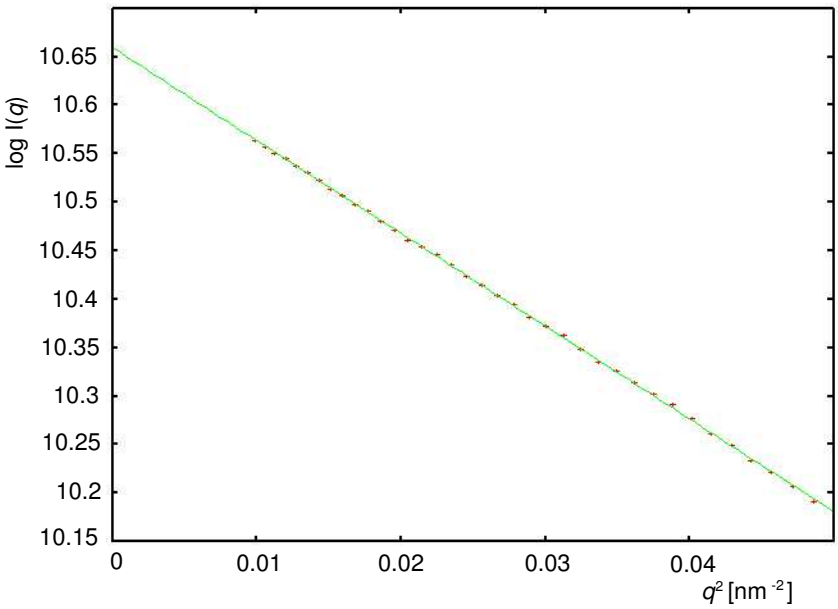

(b) Imaging plate

Figure 3.17: Guinier plots for an Apo-Ferritin.

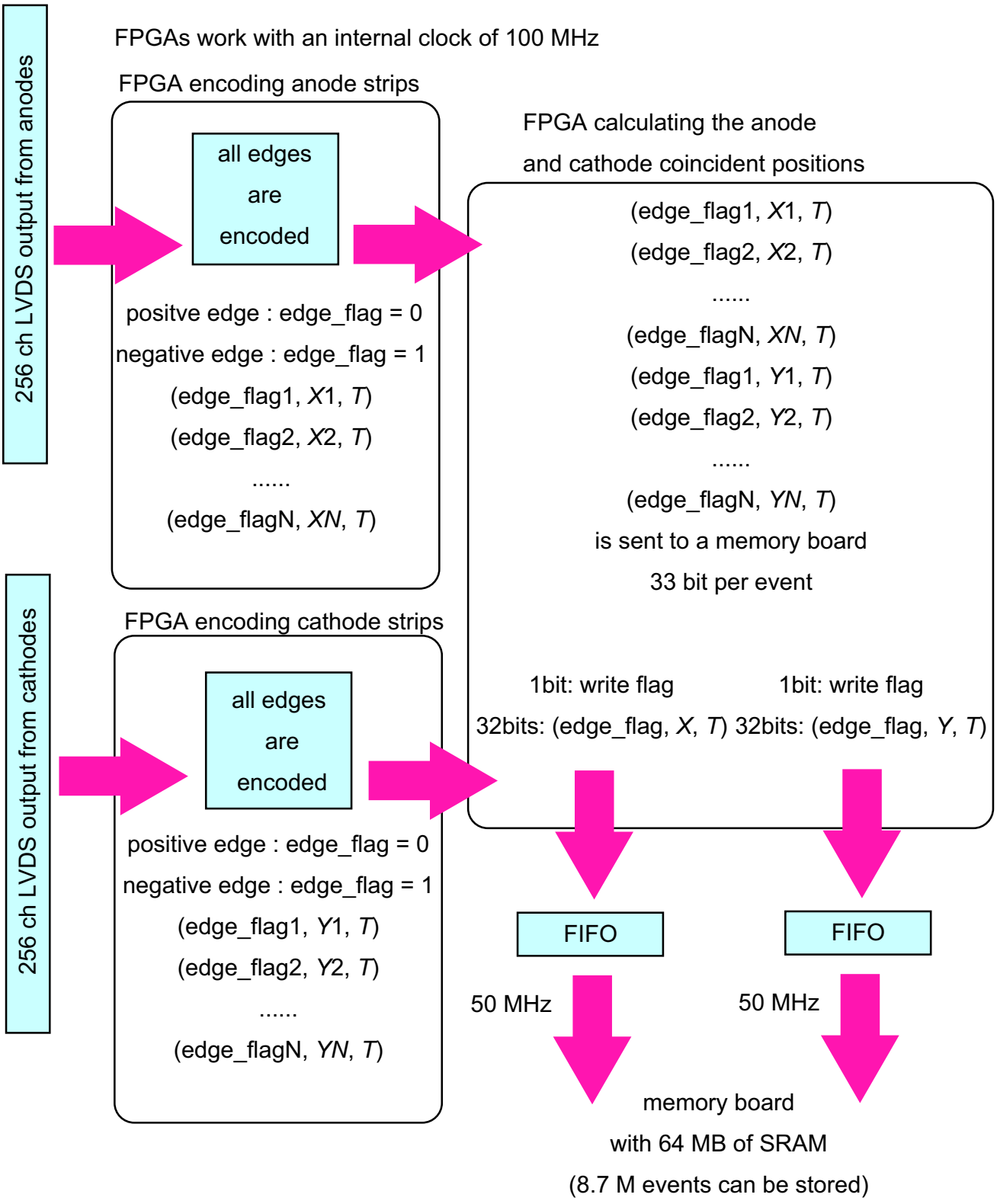

Figure 3.18: A block diagram of the mode-III position encoding system

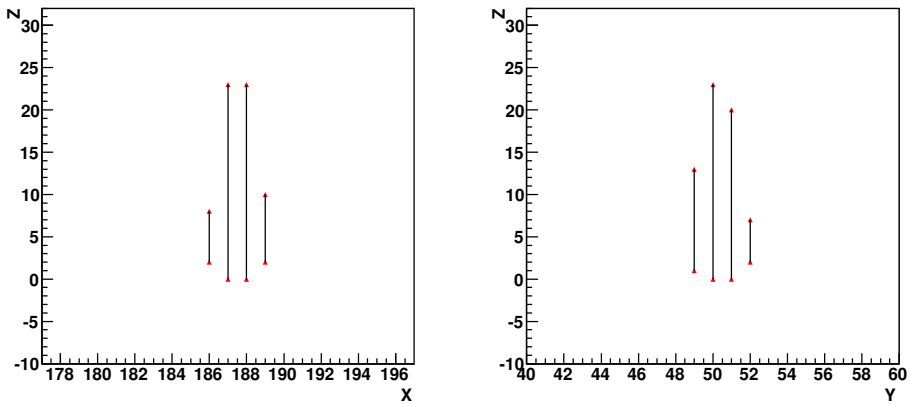

(a)

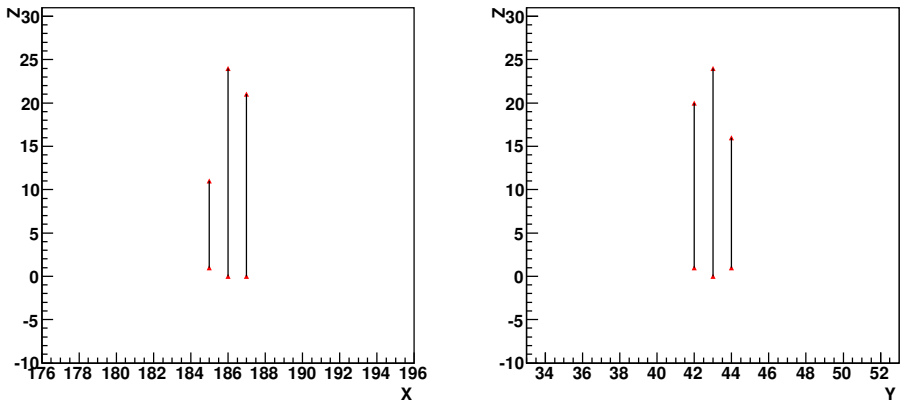

(b)

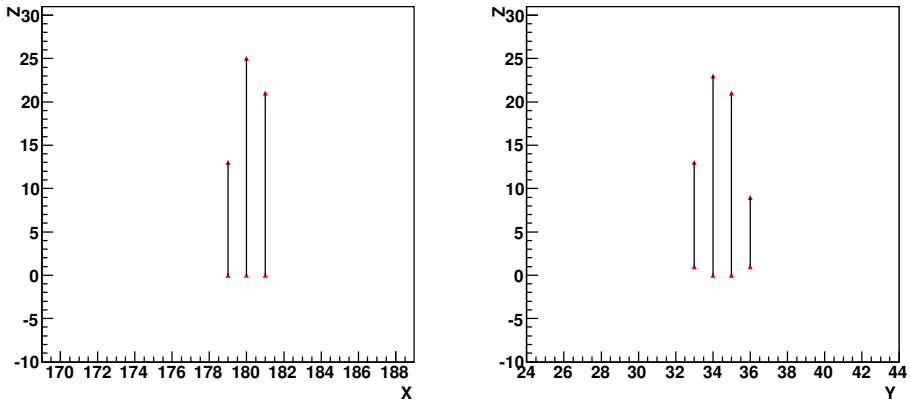

(c)

Figure 3.19: Typical X-ray events monitored by the mode-III encoding system. The detector was irradiated with X-rays of 1.5 Å (8 keV) at SPring-8. X refers to the strip number of anodes: Y to the strip number of cathodes; Z to the clock. Z = 0 is defined as the time when the first hit is detected. Red-filled triangles display the timing of leading edges and falling edges while lines denote clocks when the signals exceed the threshold.

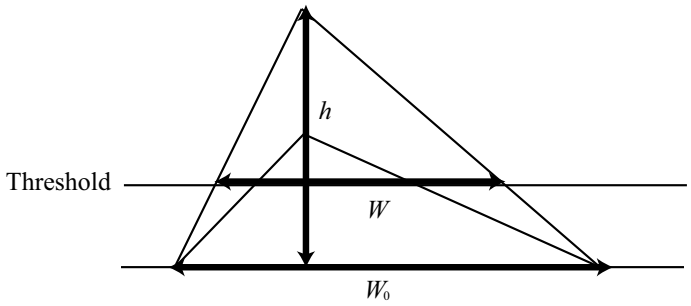

Figure 3.20: Schematic of the analog output of the ASD and definition of the parameters.

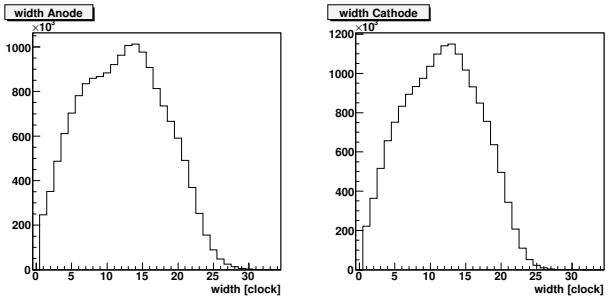

Figure 3.21: Distribution of the pulse width. The detector was irradiated with an X-ray generator. The acceleration voltage of the X-ray tube was set to 45 kV.

$$h = \frac{1}{1 - \frac{W}{W_0}} V_{\rm th} \tag{3.2}$$

Thus, the relative pulse height $h/V_{\rm th}$ is determined by the width W and the length of the base W_0. The width W tends to W_0 as h tends to infinity. Therefore, W_0 corresponds to the maximum width under a condition where pile-up is does not occur. Using the expression given in Eq. (3.2), the centroid of the charge distribution is calculated by the width of the hits. The calculation of the position of the X-ray is performed independently in X and Y.

W_0 was determined by the maximum width. Under high-counting rate environments, pile-up is likely to occur and the width occasionally becomes longer than that of a single pulse. Therefore, W_0 was invesitaged under a low-counting rate environment where the counting rate per pixel is less than 10 Hz. Figure 3.21 shows the resultant distribution of the pulse height. The detector was irradiated with an X-ray generator without a monochrometer. The acceleration voltage of the X-ray tube was set to 45 kV. The X-ray tube mainly emits copper fluorescent of 8 keV but also emits X-rays with higher energy up to 45 keV. In this experiment, the ASD reference threshold voltage was set to -45 mV (anodes) and 55 mV (cathodes). This assymetric threshold level makes the width distributions shown in Fig. 3.21 different. All the experiments using the mode-III system were applied to this threshold voltage. The maximum width for the anodes and the cathodes are about 300 ns and 280 ns, respectively. The position resolution weakly depends on W_0 and the error of about 50 ns is allowed. Therefore, we set W_0 to 300 ns for the anodes and 280 ns for the cathodes.

3.5.2 Position resolution

We achieved improvements in the position resolution using the mode-III system. The position resolution was evaluated from an image of a grid mask where holes with a radius of 250 μm were

drilled. The entrance window of the μ-PIC was masked and irradiated with scattering from a piece of a glassy carbon. The scatterer was placed 1666 mm in front of the detector plane and was irradiated with X-rays of 1.5 Å (8 keV) at SPring-8. The centroid of the charge distribution was calculated using pulse widths and the resultant image is displayed in Fig. 3.22.

The counts distribution around a hole as a function of the distance from the hole center r is shown in Fig. 3.23. The holes close to the beam center (< 32 mm) were summed up. If the fluctuation of the calculated positions is characterized by a Gaussian distribution with deviation σ, the counts distribution is represented by the curves shown in Fig. 3.24. The polar cooridanate system (r, θ) is used to denote the distribution. Figure 3.24(a) shows counts per pixel; (b) shows the integral of (a) on the interval of $0 \leq \theta \leq 2\pi$. According to Fig. 3.24(b), the tails of the curves strongly depend on σ. The area around the center is less important to determine σ because the curves are almost propotional to r there. The distribution shown in Fig .3.23(a) and (b) is fitted by the curve shown in Fig. 3.24(b). The resultant position resolution is $\sigma = 93.6$ μm. For reference, the same image was recorded by the mode-II system and the position resolution was determined to $\sigma = 157.9$ μm that is larger than $\sigma = 120$ μm described in section 2.2.5.

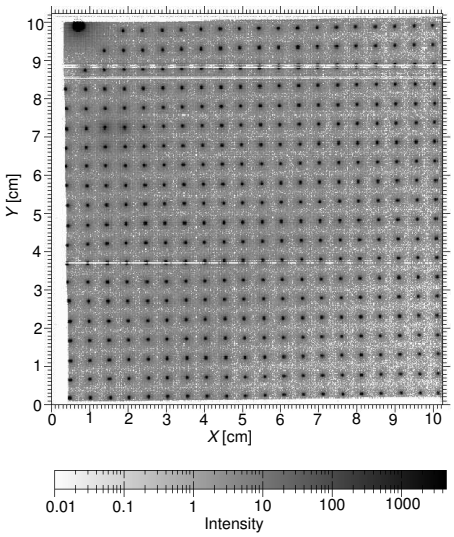

Figure 3.22: Image of a grid mask. The entrance window of the μ-PIC was masked and irradiated with scattering from a piece of a glassy carbon. The bin size is set to $200\mu\text{m} \times 200\mu\text{m}$.

The counts distribution shown in Fig. 2.17 is the projection along the edge at a 45° angle from the μ-PIC strips. The position resolution of the μ-PIC is minimum at a 45° angle and maximum at a right angle. In the case of the holes, the position resolution of their edges is the average over all the angles. If the position resolution at a right angle is expressed by σ, the averaged value is given by

$$\frac{\int_0^{4\pi} \cos\theta \mathrm{d}\theta}{\frac{1}{4\pi}}\sigma = \frac{4}{\sqrt{2}\pi}\sigma = 0.900\sigma. \tag{3.3}$$

This equation implies that the position resolution of $\sigma = 120$ μm at a 45° angle corresponds to $\sigma = 120 \times 0.900 \times \sqrt{2} = 153$ μm on the edges of the holes. This value is similar to the resolution of mode-II (157.9μm).

We have assumed that the shape of the analog output is a triangle and the width is expressed by eq. 3.2. This is a rough approximation of the X-ray position but improves the resolution. However, the actual shape, shown in Fig. 2.11, is not a triangle. Therefore, the correlation of the pulse widths with the pulse heights determined by real measurements will enhance the position resolution.

3.5.3 Refinements in scattering curves

Chicken collagen

We also examined the mode-III system using diffraction from chicken collagen and solution scattering. Figure 3.25 shows a diffraction pattern of chicken collagen. The scatterer was placed 1666 mm in front of the detector plane and was was irradiated with X-rays of 1.5 Å (8 keV) at SPring-8.

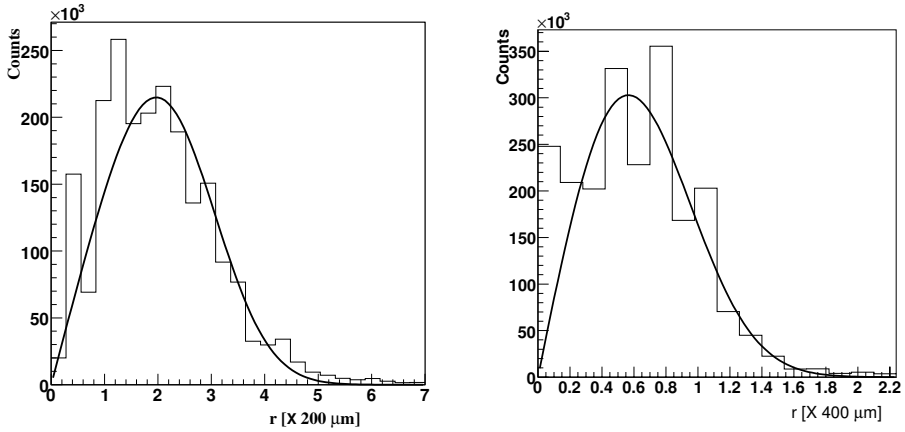

(a) mode-III (b) mode-II

Figure 3.23: Counts distribution as a function of the distance from the center of the holes. Holes close to the beam center (< 32 mm) were summed up.

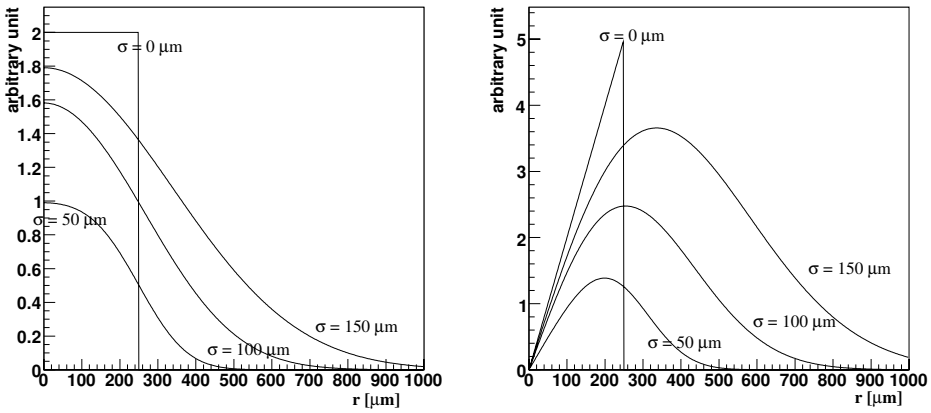

(a) Counts per pixel.

(b) Integral of (a) on the interval of $0 \leq \theta \leq 2\pi$.

Figure 3.24: Counts distribution around a hole with a diameter of 500 μm.

The resultant images are displayed in Fig. 3.25 (a) and (b). The bin size is set to $200\mu\text{m} \times 200\mu\text{m}$. The first peak about 1.5 mm apart from the shade of the beam stopper is clearly separated. For reference, the averaged positions of hits recorded by the mode-II system were integrated and the resultant images are shown in Fig. 3.25 (c), (d) and (e). Due to the position resolution, there are many empty bins in Fig. 3.25(c) where the bin size is set to $200\mu\text{m} \times 200\mu\text{m}$.

The angular region designated by the diagonal lines in Fig. 3.25 (a) is used to determine the distributions shown in Fig. 3.26. The black lines referring to the diffraction curve determined by Fig. 3.25(a) have higher diffraction peaks and show a improved resolution. The oscillating curves in Fig. 3.26 (c) and (d) are due to many empty bins in Fig. 3.25(c). We adjusted the bin size of the scattering curve drawn by the red line in Fig. 3.26 (c) to smooth, and examined the position resolution of the first and the second peak of the sample shown in Table 3.2. Then it was compared with the resolution of the peaks obtained by the mode-III system. It can be concluded that the position resolution of the peaks was improved well by position interpolation. The diffraction curve determined by Fig. 3.25(a) was also compared with that observed by the IP for reference shown in Fig. 3.25(e) and these two curves agree well. The pixel pitch of the IP is 100 μm.

Table 3.2: The position resolution (FWHM) of the first and the second peaks of chicken collagen.

	mode-II	**mode-III**
1st peak	0.0148 nm^{-1}	0.00807 nm^{-1}
2nd peak	0.0111 nm^{-1}	0.00161 nm^{-1}

Solution scattering

We measured solution scattering from SiO_2 nano particles using the mode-III system. The diameter of the particles is 110 nm. The instrumentation is same as that used for the observation of the diffraction from the collagen metioned before. The resultant scattering curve is shown in Fig. 3.27. Using the same data set, the scattering curves with and without interpolation are compared. The curve with interpolation has steeper valleys and agrees better with that observed by the IP with a pitch of 100 μm. The first peak that corresponds to the edge of the shadow of the beam stopper is lower in comparison with that measured by the IP. It might be due to the aging mentioned in Section 3.4.2. The scattered X-rays by the sample concentrated on the edge of the shadow and the gain there dropped.

Table 3.3 summarizes the results of the analysis of solution scattering from the SiO_2 nano particles. Since the mode-III system records both leading edges and falling edges of the hits of the ASDs, the number of events generated by an X-ray doubles in comparison with mode-II.

3.6 Future improvements

3.6.1 Gain stability

The ideal detection efficiency of photo-electrons generated by X-rays in the detection volume is 100 %. To achieve it, the pulse height of signals generated by the X-rays must be well above the threshold applied to the ASDs. The detection efficiency is not effected by the gain variation of the detector while the pulse heights of the signals are well above the threshold. In principle, the gain of the μ-PIC (and many micro-pixel gaseous detectors) vary within a time-frame of several hours after a high voltage is applied. The duration of this gain variation is determined by the time constant of the polarization of the polyimid placed between the anodes and the cathodes. Moreover, the gain could be changed by intense X-rays, as mentioned in 3.4.2. Therefore, to keep the detection efficiency of the liberated electrons at 100 % is an important issue. To eliminate the fluctuation

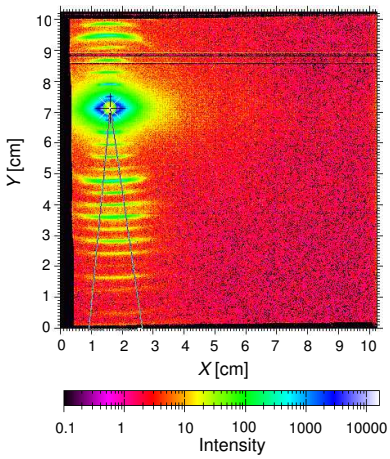

(a) Integration of interpolated positions from pulse widths. The bin size is set to 200μm $\times$ 200μm.

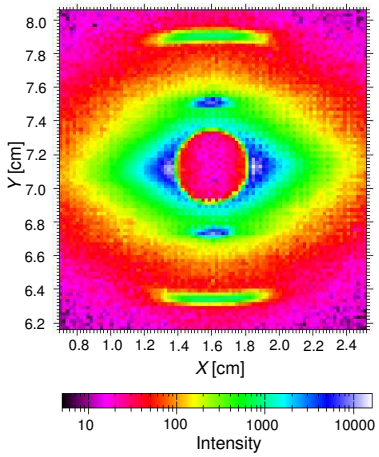

(b) Integration of interpolated positions from pulse widths. The bin size is set to 200μm $\times$ 200μm.

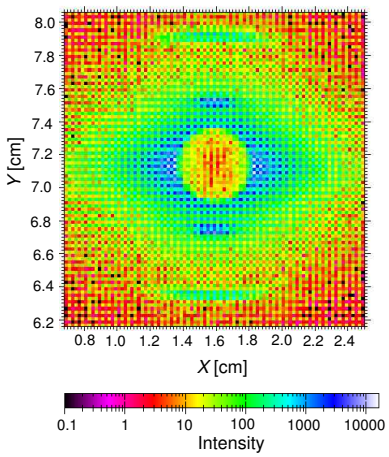

(c) Averaged positions of hits were integrated. The bin size is set to 200μm $\times$ 200μm, the same as (a) and (b).

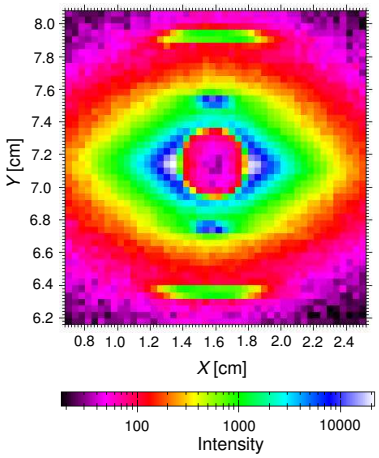

(d) Averaged positions of hits were integrated. The bin size is set to 400μm $\times$ 400μm

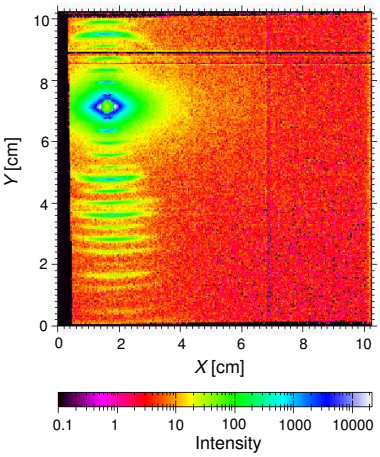

(e) Averaged positions of hits were integrated. The bin size is set to 400μm $\times$ 400μm

Figure 3.25: Diffraction pattern of chicken collagen. The detector was irradiated with X-rays of 1.5 Å (8 keV) at SPring-8. Counts per bin is displayed in the two-dimensional histograms. (a) (b) The centroid of the charge distribution was calculated using pulse widths. The first peak about 1.5 mm distanced from the shade of the beam stopper is clearly separated. (c) (d) (e) Averaged positions of hits recorded by the mode-II system were integrated. Due to the pixel size of the μ-PIC , there are many empty bins in (c).

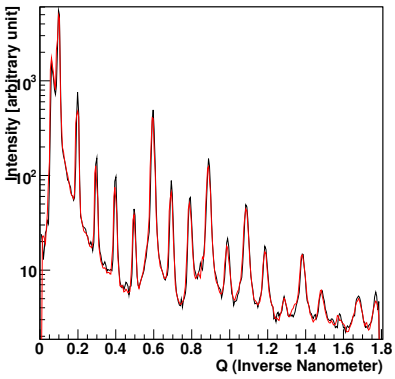

(a) The Red line refers to the diffraction curve of Fig. 3.25 (e).

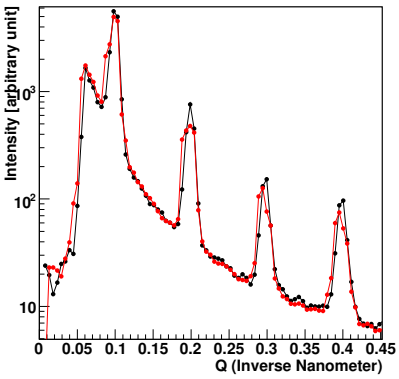

(b) The Red line refers to the diffraction curve of Fig. 3.25 (e).

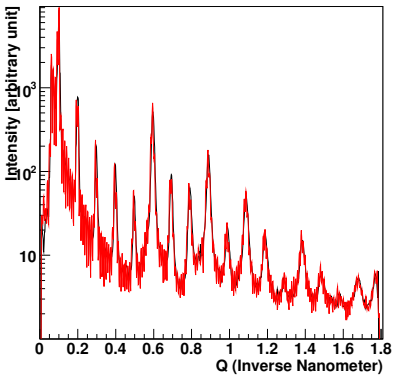

(c) The Red line refers to the diffraction curve of Fig. 3.25 (c).

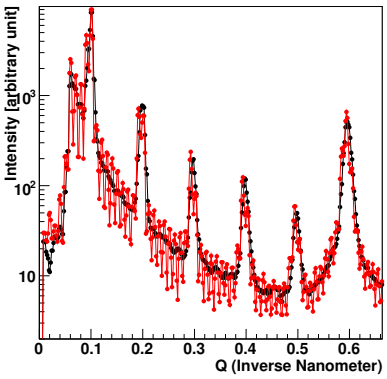

(d) The Red line refers to the diffraction curve of Fig. 3.25 (c).

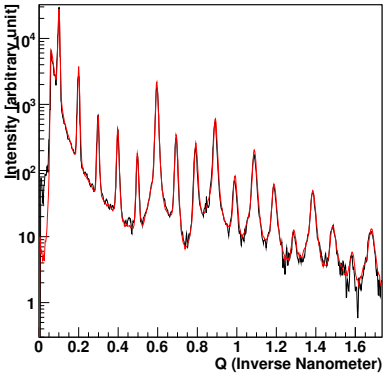

(e) The Red line refers to the diffraction curve observed by the IP for reference.

Figure 3.26: Comparison of the diffraction curve determined by mode-III with Fig. 3.25 (c) and (e). The angular region used to determine the distributions is designated by the diagonal lines shown in Fig. 3.25 (a). The black lines refer to the diffraction curve of Fig. 3.25.

Table 3.3: Results of an analysis of solution scattering from the SiO_2 nano particles and water are summarized. The number of events generated by an X-ray doubles because the mode-III system records both leading edges and falling edges of the hits of the ASDs. 'After analysis' represents the number of the X-rays hitting the detector.

SiO_2 nano particles		
Exposure time	800.949 sec	
Events (total)	598,680,543	
Data acquisition rate	747.464 kHz	
After analysis	46,797,583 photons	(7.817%)
Counting rate of X-rays	58.43 kHz	

Water		
Exposure time	3960.94 sec	
Events (total)	376,858,883	
Data acquisition rate	95.1438 kHz	
After analysis	28,874,951 photons	(7.662%)
Counting rate of X-rays	7.289 kHz	

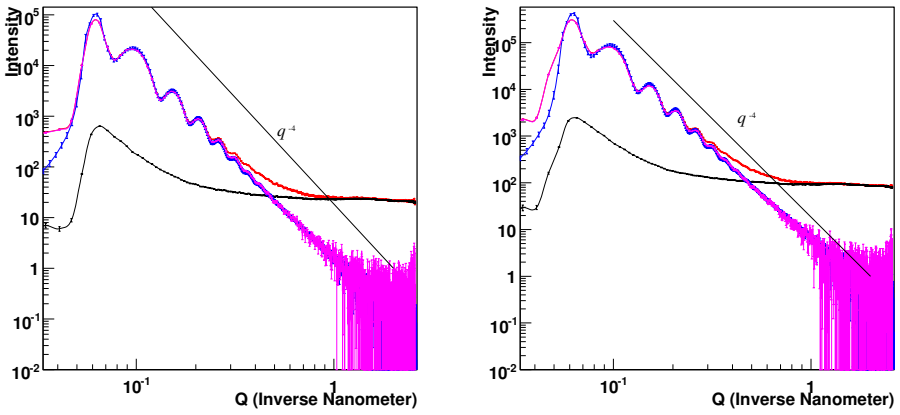

(a) Integration of interpolated positions from pulse widths.

(b) Averaged positions of hits were integrated.

Figure 3.27: Solution scattering patterns from SiO_2 nano particles. The diameter is 110 nm. (a) and (b) uses the same data collected by the mode-III encoding system. The sample was irradiated with 1.5 Å (8 keV) X-rays at BL45-XU SPring-8. The red, black, pink, blue lines refer to a scattering curve of the solution, a solvent (water), their subtraction, and a scattering curve measured by IP (R-Axis) for reference, respectively.

of the detection efficiency, we need to improve the signal-to-noise ratio and ensure that all signals generated by the X-rays exceed the threshold. The solution is described in Section 3.4.2.

3.6.2 Counting rates

To avoid radiation damage of samples and obtain fine scattering patterns, exposure of intense X-rays for a short duration is required. Thus, the X-ray area detector must work properly under the high-counting rate environments. Now we confirmed that the mode-I position encoding system functions at a DAR of 5 MHz and the mode-II system at a DAR of 7 MHz. Our goal is to operate the μ-PIC under the high-counting rates where IPs are used. We successfully measured the solution scattering in such an environment and achieved the dynamic range of $> 10^6$. The DAR of the mode-III system is estimated at > 10 MHz there. However,the mode-III system is more complex and records more information. Thus, the data flow is bottlenecked in an FPGA controlling the output to the memory module at a DAR of > 2 MHz. Therefore, the position encoding system is in need of a renewal.

The current encoding system uses three FPGAs; one for the anodes, another for the cathodes, and the other functions as a controller. The controller receives encoded positions from the other two FPGAs and sends the data to the memory module. A propagation delay caused by communications between the controller and the other two FPGAs is the main reason of the counting rate limit. the output of encoded positions should be sent directly to the memory module.

3.6.3 Detection efficiency for X-rays

X-rays scattered by a sample are absorbed by a 4-mm Xe-C_2H_6 (70:30) gas layer kept at 1 atm. The detection efficiencies for 8 keV and 13.8 keV X-rays, which are commonly used at BL45-XU SPring-8, are 24% and 8%, respectively. As shown in Table 3.4, the absorption by the gas layer located between the entrance window and the drift plane is a major loss of incident X-rays. Therefore, the drift plane must be glued to the internal side of the polyimide entrance window. Since incident X-rays need to penetrate an entrance window, the window must be kept thin, and does not have a tolerance for a pressure of $>$ 1atm. For this reason, increasing the gas pressure is not an easy way to improve the detection efficiency. However, since the detector is aiming at small-angle scattering measurements, it is unnecessary to consider parallax. Thus one can safely double the thickness of the gas layer and the detection efficiency will also be doubled.

Table 3.4: Absorption rates. The gas layer represents that located between the entrance window and the drift plane and its thickness is 2 mm. X-rays of 8 keV and 13.8 keV are commonly used at BL45-XU, SPring-8.

Energy	**Entrance window and drift plane**	**gas layer**	**detection region**
8 keV (1.5 Å)	$\sim 10\%$	17%	32%
13.8 keV (0.9 Å)	$\sim 2\%$	4.4%	8.5%

The diffusion is an important issues which must be taken into account when one extends the thickness of the gas layer. The diffusion of the electrons as they drift toward the μ-PIC is proportional to $\sqrt{z}$, where z is the drift length. The diffusion coefficient of a Xe-C_2H_6 (70:30) gas is 210 $\mu\mathrm{m}\sqrt{\mathrm{cm}}$ at a drift field strength of 0.7 kV/cm. The root mean square of the electron cloud distribution after 4-mm drift is 132 μm and after 8-mm drift is 187 μm. Even in the case of the 8-mm gas layer, the diffusion is considerably smaller than the pitch of the μ-PIC . In addition, we derive the centroid of the electron cloud distribution using the pulse widths and thus, it is easy to estimate the diffused distribution of the electron cloud. It can be concluded that the detector with the 8-mm gas layer will double the detection efficiency for X-rays and will maintain almost the same position resolution as the current detector.

3.6.4 μ-PIC with large active area

One solution for improvements of the angular resolution of scattering curves is to obtain the centroid of the electron distribution, and another is to extend the active area of the detector, which allows extension of a camera length. In this case, the position resolution remains the same but the angular resolution, which is a function of the camera length, improves.

We have successfully fabricated a μ-PIC with an active area of 300 mm$\times$300 mm, shown in Fig. 3.28(a), and demonstrated its stability for long-duration operation. We used the same readouts as that of the μ-PIC with a detection area of 100 mm$\times$100 mm. X-ray imaging using a μ-PIC with a large active area is now under investigation. We successfully tested the detector system based on the large μ-PIC work at SPring-8. Figure 3.28(b) shows the setup. The detector was irradiated with 0.9 Å (13.8 keV)scattering from a silver behenet powder and yielded the two-dimensional image shown in Fig. 3.28 (c). One can see two diffraction rings in this image.

For this measurement, the detector is contained in a sealed aluminium vessel with an aluminum entrance window of 1-mm thickness. We used an Ar-C_2H_6 (90:10) gas mixture, which can stabilize the μ-PIC better than a Xe-based gas mixture. Since the experiment was conducted without a GEM, the signal-to-noise ratio was not good. We are planning to install a large GEM with an active area of 230 mm$\times$ 280 mm, the largest currently available; replace the aluminum window with polyimide; and use a Xe-based gas mixture. As a consequence, the detection efficiency and the signal-to-noise ratio should improve.

3.6.5 Compact system

For delivering compact readouts with low power, a CMOS-ASIC chip with amplifiers and discriminators is being developed at KEK, Japan. The number of channels is doubled to 8 channels per chip. In a few years, these CMOS-ASIC chips will allow all the readout electronics to be located on the rear of the gas vessel, and make it possible to develop an imaging detector similar in size to a PC-notebook at a reasonable cost.

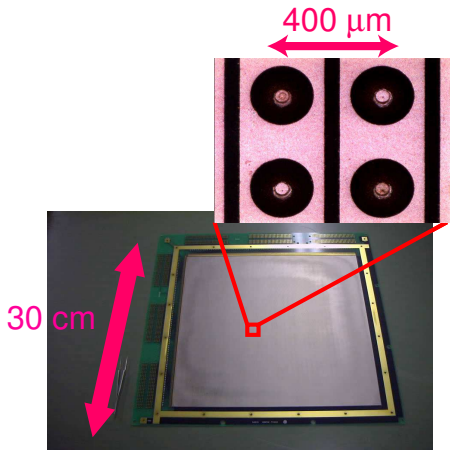

(a) μ-PIC with an active area of 300 mm×300 mm.

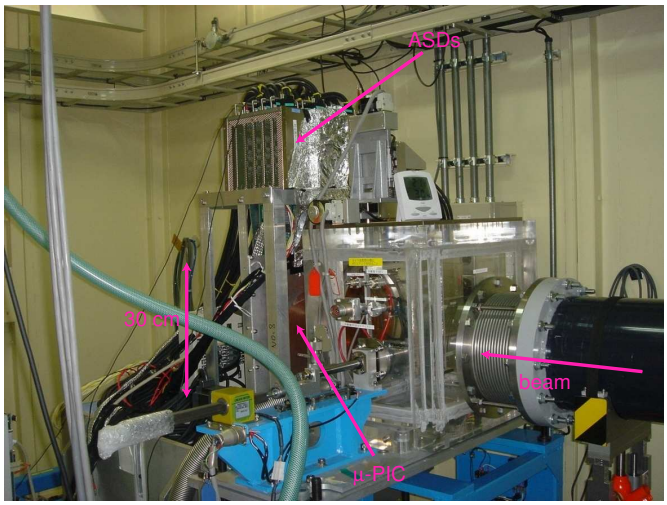

(b) X-ray area detector based on the μ-PIC with an active area of 300 mm×300 mm at beamline BL45XU.

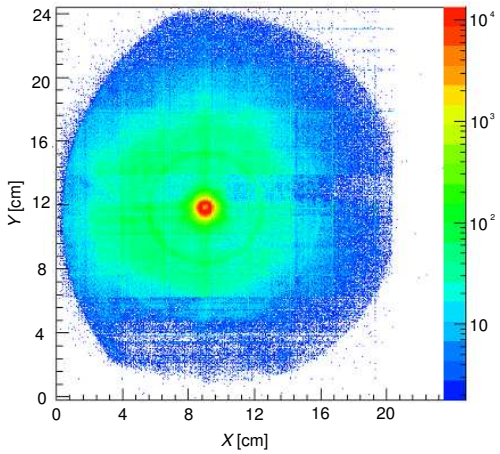

(c) The first image observed by the large μ-PIC . Scattering pattern from a silver behenet powder irradiated with 0.9 Å (13.8 keV) X-rays at SPring-8.

Figure 3.28: μ-PIC with a large active area.

Chapter 4

Application to Compton camera

As mentioned in chapter 2, the development of the μ-PIC has been originally motivated by an application to a Compton camera on board a satellite. Figure 4.1 shows a schematic of the camera. A Time Projection Chamber based on a μ-PIC (micro-TPC) is a component of the Compton camera and a gamma-ray Compton-scattered there is observed. The scattered gamma-ray is absorbed by pixellated scintillators surrounding the micro-TPC while the recoil electron is absorbed by the micro- TPC. The micro-TPC and scintillators acquire a complete set of kinematic and geometry information and then the incident gamma-ray can be fully reconstructed. In this chapter, we report on improvements of the data acquisition (DAQ) for the micro-TPC. The concept of mode-II was used for the improvement on DAQ for the micro-TPC.

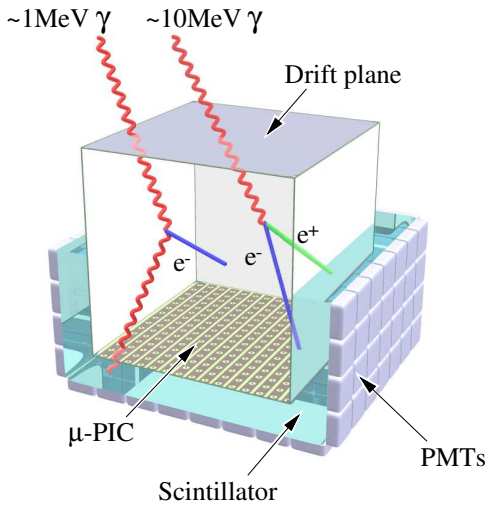

Figure 4.1: Schematic of a Compton camera based on the μ-PIC . The Compton camera consists of the micro-TPC surrounded by scintillators and the encoding system.

4.1 MeV gamma-ray observation

Many attractive phenomena - supernova remnants, spin-down pulsers, black holes, the galactic center, and active galactic nuclei - radiate MeV gamma-rays. Production of gamma-rays in the universe involves several mechanisms such as synchrotron radiation, Bremsstrahlung, inverse Compton scattering, nuclear transition and decay and annihilation. Thus, MeV gamma-ray observations bring many useful information about the universe.

The dominant interaction in the energy band from a sub MeV up to several tens is Compton scattering. Observing Compton scattering is the most challenging matter. Tracking recoil electrons is difficult because of the high probability of multiple scattering in material. The multiple scattering deteriorates an anglular resolution of incident gamma-rays. In addition, gamma-rays Compton-scattered by a satellite induce internal background. It is also difficult to separate signals from background because of the insufficient anglular resolution.

A few observations for MeV gamma-rays on board satellites were carried out in the past. It should be noted that the number of observations in this energy band is quite small in comparison

with other energy bands. The most successful observation in this energy band is COMPTEL [33] on board the Compton Gamma Ray Observatory (CGRO) satellite. In spite of the successful all-sky survey conducted by COMPTEL, the number of celestial objects found in the MeV gamma-ray band was smaller by an order of magnitude than that found in the GeV band. Thus, a Compton telescope with an improved detection sensitivity is awaited.

COMPTEL consists of two planes of position sensitive detectors: modules filled with organic liquid scintillator and NaI(Tl) crystal arrays. The liquid scintillator has a low atomic number to prevent multiple-Compton scattering. Gamma-rays Compton-scattered in the liquid scintillator are absorbed by the inorganic crystals. The NaI(Tl) crystals which have a high atomic number and a high density were chosen to enhance the photon absorption properties. The two detectors measure energy and hit positions of a recoil electron and a scattered gamma-ray. A momentum of the scattered gamma-ray can be reconstructed by the hit positions. A measure of a time difference between the two detectors (time-of-flight) is used for background reduction. Since the direction of a Compton recoil electron was not measured with COMPTEL, the direction of the incident photon could only be reconstructed as a cone demonstrated in Fig. 4.2. Accordingly, it was difficult to reject the background, thereby limiting the sensitivity. The time-of-flight value was useful for the background reduction but insufficient.

Measuring the direction of the recoil electron reduces the Compton cone to a small segment of the cone, and leads to the stronger background rejection [34] [35]. Figure 4.3 shows a principle of the electron tracking camera. To measure both the three-dimensional track and the energy of the recoil electron, the micro-TPC based on the μ-PIC was introduced.

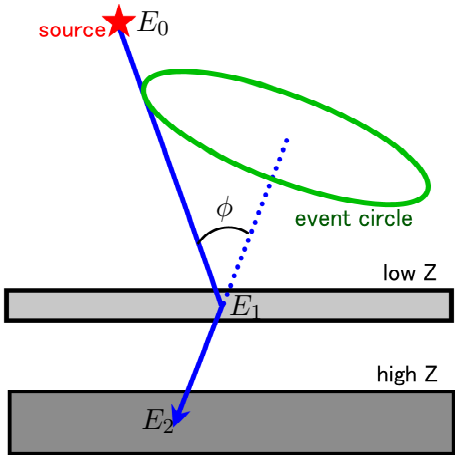

Figure 4.2: Schematic view of Compton scattering occurred in COMPTEL.

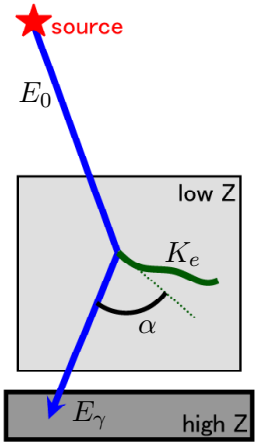

Figure 4.3: Schematic view of an electron tracking camera.

4.2 Reconstruction of Compton events

The electron tracking camera provides complete reconstruction of incident gamma-rays using kinetic energy and a momentum vector of a recoil electron, and energy and a momentum vector of a scattered gamma-ray. Figure 4.4 shows a schematic of a Compton event. Here, we define some variables.

The momentum vector of the incident gamma-ray, $\vec{s}_{\rm rcs}$, which normalized to $|\vec{s}_{\rm rcs}| = 1$ and its energy $E = 0$ are given by

$$E_0 = E_\gamma + K_e \tag{4.1}$$

$$\vec{s}_{\rm rcs} = \left(\cos\phi - \frac{\sin\phi}{\tan\alpha}\right)\vec{g} + \frac{\sin\phi}{\sin\alpha}\vec{e} \tag{4.2}$$

where E_γ, K_e, $\vec{g}$, $\vec{e}$, ϕ, α represent the energy of the scattered gamma-ray, the kinetic energy of the recoil electron, a scattering angle of the gamma-ray, and a recoil angle of the electron, respectively. The scattering angle ϕ is given by

$$\cos\phi = 1 - \frac{m_e c^2}{E_\gamma + K_e}\frac{K_e}{E_\gamma} \tag{4.3}$$

The recoil angle α is derived by $\vec{g}$ and $\vec{e}$. This value $\alpha_{\rm geo}$ is given by

$$\cos\alpha_{\rm geo} = \vec{g}\cdot\vec{e} \tag{4.4}$$

The recoil angle is also derived by the kinetic energy of the recoil electron and the gamma-ray. This value $\alpha_{\rm kin}$ is given by

$$\cos\alpha_{\rm kin} = \left(1 - \frac{m_e c^2}{E_\gamma}\right)\sqrt{\frac{K_e}{K_e + 2m_e c^2}} \tag{4.5}$$

$\alpha_{\rm geo}$ and $\alpha_{\rm kin}$ are derived by the independent variables and thus they are also independent. In the case of the background events, $\alpha_{\rm geo}$ and $\alpha_{\rm kin}$ have different values. Selection of events whose $\alpha_{\rm geo}$ is the same as $\alpha_{\rm kin}$ brings the strong background rejection. Now we refer to the selection as an *alpha* cut.

Electron tracking cameras can reconstruct gamma-rays event by event. Thus two angular resolutions for an incident gamma-ray can be defined when a position of a gamma-ray source is known.

- ARM (Angular Resolution Measure) : resolution of the scattering angle of the gamma-ray, ϕ.

$$\mathrm{ARM} = \phi_{\rm geo} - \phi_{\rm kin} \tag{4.6}$$

- SPD (Scatter Plane Deviation) : resolution of a plane including $\vec{g}$ and $\vec{e}$

$$\mathrm{SPD} = \left(\vec{g}\cdot\left(\frac{\left(\frac{\vec{g}\times\vec{s}_{\rm rcs}}{|\vec{g}\times\vec{s}_{\rm rcs}|}\right)\times\left(\frac{\vec{g}\times\vec{s}}{|\vec{g}\times\vec{s}|}\right)}{\left|\left(\frac{\vec{g}\times\vec{s}_{\rm rcs}}{|\vec{g}\times\vec{s}_{\rm rcs}|}\right)\times\left(\frac{\vec{g}\times\vec{s}}{|\vec{g}\times\vec{s}|}\right)\right|}\right)\right)\arccos\left(\left(\frac{\vec{g}\times\vec{s}}{|\vec{g}\times\vec{s}|}\right)\cdot\left(\frac{\vec{g}\times\vec{s}_{\rm rcs}}{|\vec{g}\times\vec{s}_{\rm rcs}|}\right)\right) \tag{4.7}$$

  where $\vec{s}$ and $\vec{s}_{\rm rcs}$ represent a actual direction of the incident gamma-ray and its reconstructed direction.

4.3 Current Status of Compton camera based on the μ-PIC

In this section, the current status of the Compton camera using the position encoding system shown in Fig. 2.19 will be described. Figure 4.6 shows the Compton camera currently used. A TPC was mounted on a structure that can rotate, and was filled with an Ar-C_2H_6 gas mixture at a pressure of 1 atm. A detection volume of the TPC was 10 cm×10 cm×9.5 cm where a drift field of 0.26 kV/cm was applied. An induction field applied between the GEM and the μ-PIC was 1.06 kV/cm. The gas gains of a μ-PIC and a GEM were 3×10^3 and 10, respectively, and thus the total gas gain is 3×10^4.

Since most gamma-rays are scattered forward, scintillators used as absorbers are located behind the TPC. We arrayed 8×8 GSO:Ce scintillators with a pixel size of 6 mm× 6 mm× 13 mm read by a multi-anode Flat Panel PMT H8500. These components are combined and form 3 × 3 arrays.

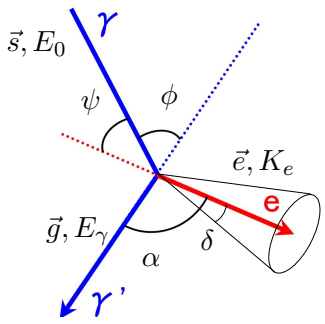

Figure 4.4: Definition of variables

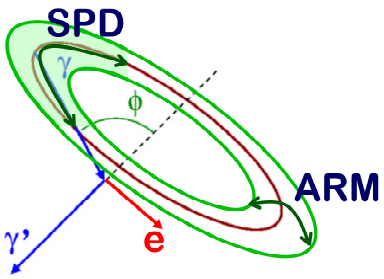

Figure 4.5: Definition of ARM and SPD

Figure 4.7(a) shows reconstructed images of gamma-rays from a point ^{137}Cs source. The spectrum of incident gamma-rays is shown in Fig. 4.7(b). The ^{137}Cs source has a strong peak at 662 keV. Energy of an incident gamma-ray should be the same as sum of that of a recoil electron and a scattered gamma-ray when their energy is completely absorbed by the camera. The reason why one can see another peak in lower energy region is that the recoil electron could escape from the TPC or the scattered gamma-ray could escape from the scintillators. It is impossible to reconstruct these events and thus they must be discarded. To yield the two-dimensional image, the blue shaded part around 662-keV peak was used. ARM and SPD were 6.5°, 132.8° (FWHM), respectively.

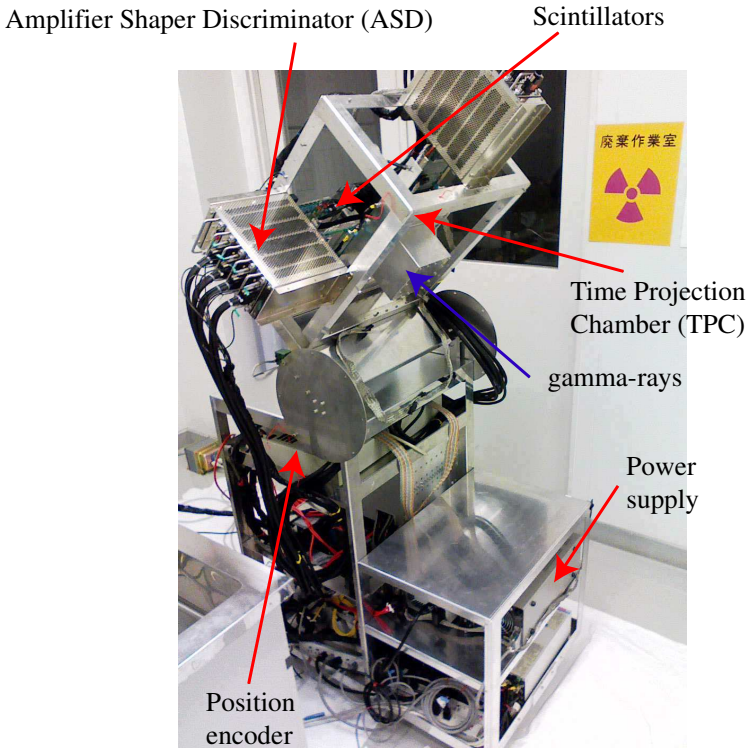

Figure 4.6: Compton camera system. The time projection chamber is mounted on a structure that can rotate.

Figure 4.8 shows an image of gamma-rays from three gamma-ray sources, ^{137}Cs (662 keV), ^{22}Na (511 keV), ^{133}Ba (356 keV). One can see three peaks from the sources in Fig. 4.8 (b). The images of the sources are successfully separated concerning the energy of the incident gamma-rays. Figure 4.8 (c)(d)(e) show events included in the yellow, green, and blue region in Fig. 4.8(b), respectively.

To check the analysis program used for our detector, GEANT4 simulations were performed [25]. Events generated by GEANT4 provide correct energy, positions, and momentum vectors and then values derived by the analysis program were compared with the real values. The position resolution of the Compton-scattered points is shown in Fig. 4.9 and the the angular difference between analyzed momentum vectors and real ones of recoil electrons in Fig. 4.10.

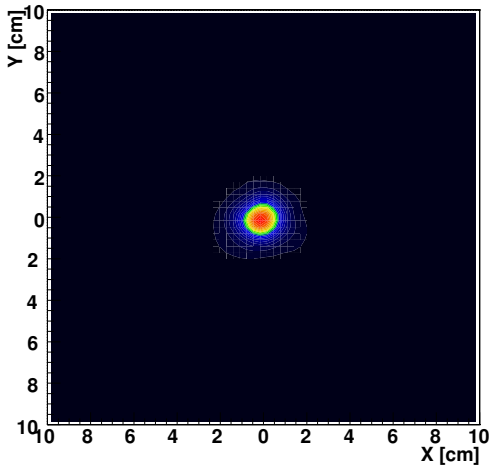

(a) Reconstructed image of gamma-rays from a ^{137}Cs source 22.5 cm apart from the TPC. The center of the μ-PIC is defined as (0 cm, 0 cm).

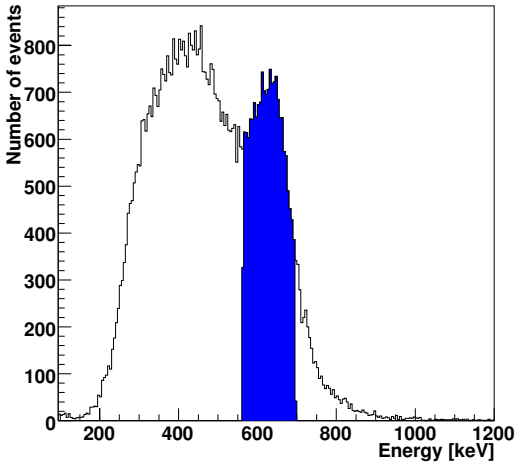

(b) Reconstructed spectrum of the gamma-rays. Blue shaded part was used to yield the image.

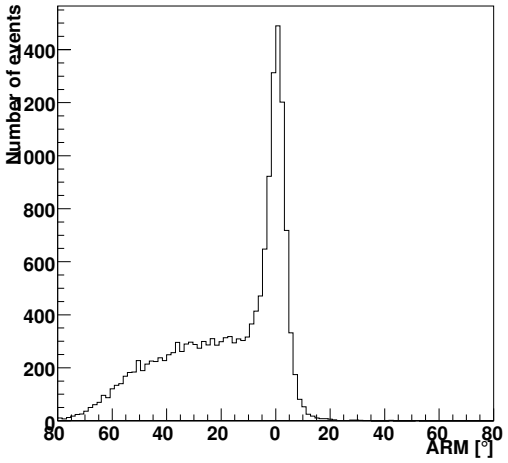

(c) ARM 6.5° (FWHM)

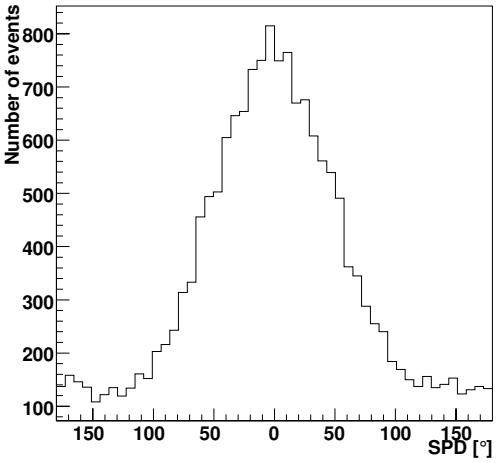

(d) SPD 132.8° (FWHM)

Figure 4.7: Irradiation with a ^{137}Cs point source.

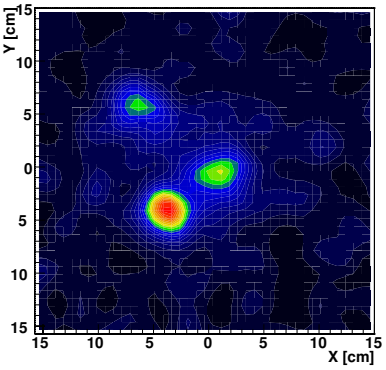

(a) Reconstructed image of gamma-rays from three gamma-ray sources. The center of the μ-PIC is defined as (0 cm, 0 cm).

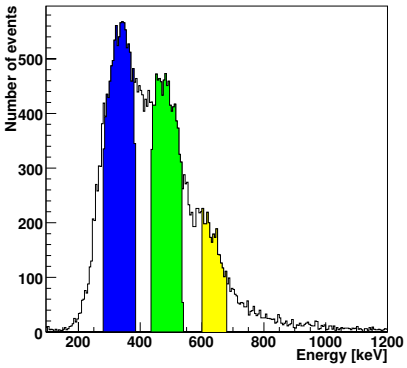

(b) Spectrum of the gamma-rays. Each shaded part was used to yield (c), (d) and (e).

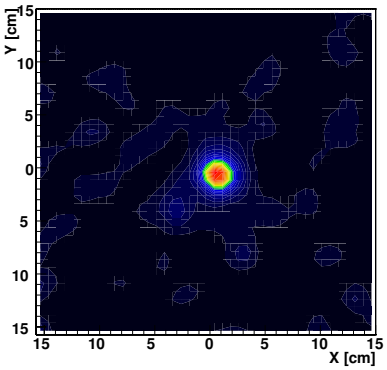

(c) Events included in the yellow region corresponding to the ^{137}Cs source.

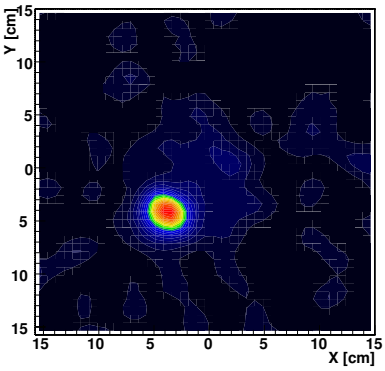

(d) Events included in the green region corresponding to the ^{22}Na source.

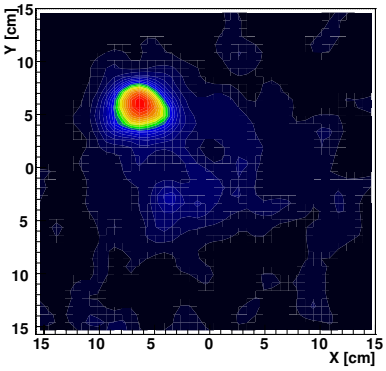

(e) Events included in the blue region corresponding to the ^{133}Ba source.

Figure 4.8: Irradiation with ^{137}Cs, ^{22}Na, ^{133}Ba point sources. The three sources were successfully separated using the energy information.

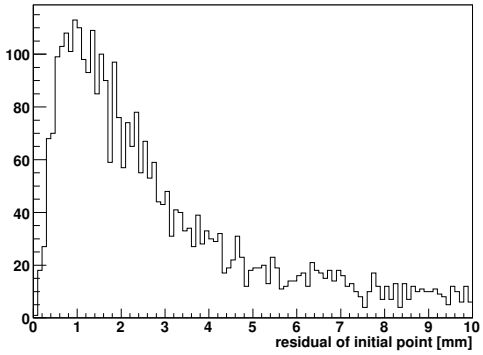

Figure 4.9: Position resolution of Compton-scattered points simulated by GEANT4 [25]. The TPC-modeI position encoding system was used.

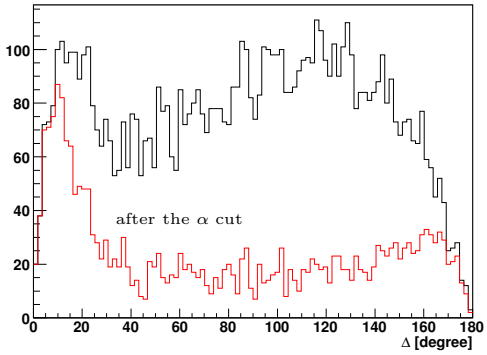

Figure 4.10: Angular difference between analyzed momentum vectors and real ones of recoil electrons [25]. Compton events were generated by GEANT4 and analyzed and then the analyzed momentum vectors and real ones were compared.

4.4 New position encoding system for micro-TPC

4.4.1 TPC mode-II

Our goal is to achieve a sensitivity of 10 times as high as that of COMPTEL. The goal necessitates a micro-TPC with a large volume ($> 50 \times 50 \times 50$ cm^3) and a μ-PIC with a large detection area. Considering the low consumption power provided by satellites, the readout electronics of the μ-PIC must be simplified. To reduce the number of channels, anodes in the same column are connected by a strip and so are cathodes in the same row. Hits from the anodes and the cathodes when they coincide in a clock interval (10 ns) are recorded and the three-dimensional tracks of the recoil electrons can be observed. We used the hits in coincidence in order to improve the signal-to-noise ratio. A block diagram of the position encoding system for use of the micro-TPC is demonstrated in Fig. 2.19.

The strip readout delivers the simple system whereas it is difficult to obtain the correct positions. Deposited charges by the recoil electrons over the anode and cathode strips depend on how many anode and cathode strips the electrons cross and the asymmetric deposition leads to the propagation delay.

In comparison with ARM, SPD is much worth due to the insufficient accuracy of the momentum vectors of the recoil electrons, as shown in Fig. 4.10. Since the electrons are multi-scattered in a gas, it is essential to measure their tracks around Compton-scattered points. However, the recoil electrons deposit less energies around the Compton-scattered points than around the endpoints of the tracks. As mentioned in Chapter 3, the propagation delay at the digital outputs of the ASDs increases as $\mathrm{d}E/\mathrm{d}x$ is low. In the case of the encoding system shown in Fig. 2.19, hits from the anodes and the cathodes are recorded when they coincide in a clock interval (10 ns), and delayed signals are discarded. Therefore, the number of hits around the Compton-scattered point is less than an end point of the electron. The resolution of the momentum vectors of the recoil electrons deteriorates due to the loss of the hits. Figure 4.9 shows that the position resolution of the Compton points is much worse than the pitch of the μ-PIC due to the loss of the hits. Therefore, some improvements similar to mode-II are necessary.

We developed a new encoding system for use of the micro-TPC. The concept of the new system is the same as the mode-II encoding system: all hits are recorded. Figure 4.11 shows a block diagram of the new system. Now we refer to the new position encoding system as TPC mode-II

and the old one as TPC mode-I.

The performance of the TPC mode-II system was investigated with cosmic muons. Two plastic scintillators were located above and below the TPC. A coincidence of these scintillators was used for the muon trigger. Figure 4.12 shows typical muon tracks. X refers to the strip numbers of the anodes: Y to the strip numbers of the cathodes: Z to the clock. $Z = 0$ is defined as the time when the first hit is detected. For conversion to length, X and Y should be multiplied by 0.04 (= pixel pitch) and Z by 0.042 determined by a drift velocity. To compare TPC mode-I with II, Fig. 4.12(b)(d) show hits from the anodes and cathodes only when they coincide in a clock interval (equivalent to TPC mode-I). The X-Z and Y-Z planes in Fig. 4.12(a)(c) show all the hits. The propagation delay is within two clocks in most cases. Thus, in the X-Y plane and three-dimensional space of Fig. 4.12(a)(c), anode and cathode hits when they coincide in two clocks interval are paired together and plotted. Figure 4.12 shows that the propagation delay is likely to occur and TPC mode-II drastically improved the quality of the muon tracks.

Figure 4.13 shows tracks of recoil electrons when the detector was irradiated with ^{137}Cs. The Compton events are demonstrated in the same manner as in Fig. 4.12. Figure 4.13 shows that the TPC mode-II system increase the number of hits per recoil electron. Electrons in a gas are multi-scattered and thus precise tracks are necessary to determine Compton-scattered points and momentum vectors there.

The distribution of the number of hits per muon track is shown in Fig. 4.14. The ASDs connected with the cathode strips generate more hits than those for the anode ones because the lower threshold is applied to the cathode readout. The absolute values of the threshold for the cathode and anode readout are usually different because of the noise level and the offset of the comparators in the ASDs. Figure 4.14(c) shows that many hits are discarded by TPC mode-I. Figure 4.15 demonstrates the distribution of the number of hits per recoil electron track. The trend of the distribution agrees with that of the muon tracks in most part. One can see peaks at 0 hit in Fig. 4.14 and 4.15. The 0-hit events are generated when only hits from the anodes are recorded, and vice verasa. Thus, these events are considered as the electronic noise accidentally coincided with the triggers. These results imply that TPC mode-II would improve the position resolution of the Compton-scattered points and SPD.

4.4.2 TPC-modeIII

It is essential to determine which edge of a track is a Compton-scattered point. To determine which edge of the track is the Compton-scattered point, a track is divided by two. The ratio of the track length to the distance between edges of each fragment is calculated [25]. A possibility of multiple scatterings increases as an electron deposits its energy. Thus, the ratio of the fragment including the Compton-scattered point must be smaller. This criterion was applied to the data described in Section 4.3. According to GEANT4 simulation, the criterion gives 60% recoil electrons correct directions. Since the ratio of 60% is slightly better than a random selection of the Compton points, this result indicates another criteria is strongly required. We will suggest a new criteria using the widths of the hits.

To measure the widths, TPC-modeIII, similar to mode-III for use of the X-ray area detector, was suggested. With minor change in the position encoding module, shown in Fig. 4.16, the widths are available. From the widths, one can deduce approximate pulse heights and then $\mathrm{d}E/\mathrm{d}x$.

Since the TPC-modeIII encoding system is being designed now, it is unavailable. Instead of the new system, we studied tracks of recoil electrons monitored by the mode-III system for use of the X-ray area detector. Figure 4.17 shows typical tracks of recoil electrons. X refers to a strip number of anodes: Y to a strip number of cathodes: Z to a clock. Z = 0 is defined as a time when analog signal from cathodes or anodes generated by a liberated electron cross the threshold for the first time. A TPC with a detection volume of 10 cm×10 cm×0.4 cm filled with Xe-C_2H_6 (70:30) gas mixture at a pressure of 1 atm. Since the detection volume is small, most of the electrons would

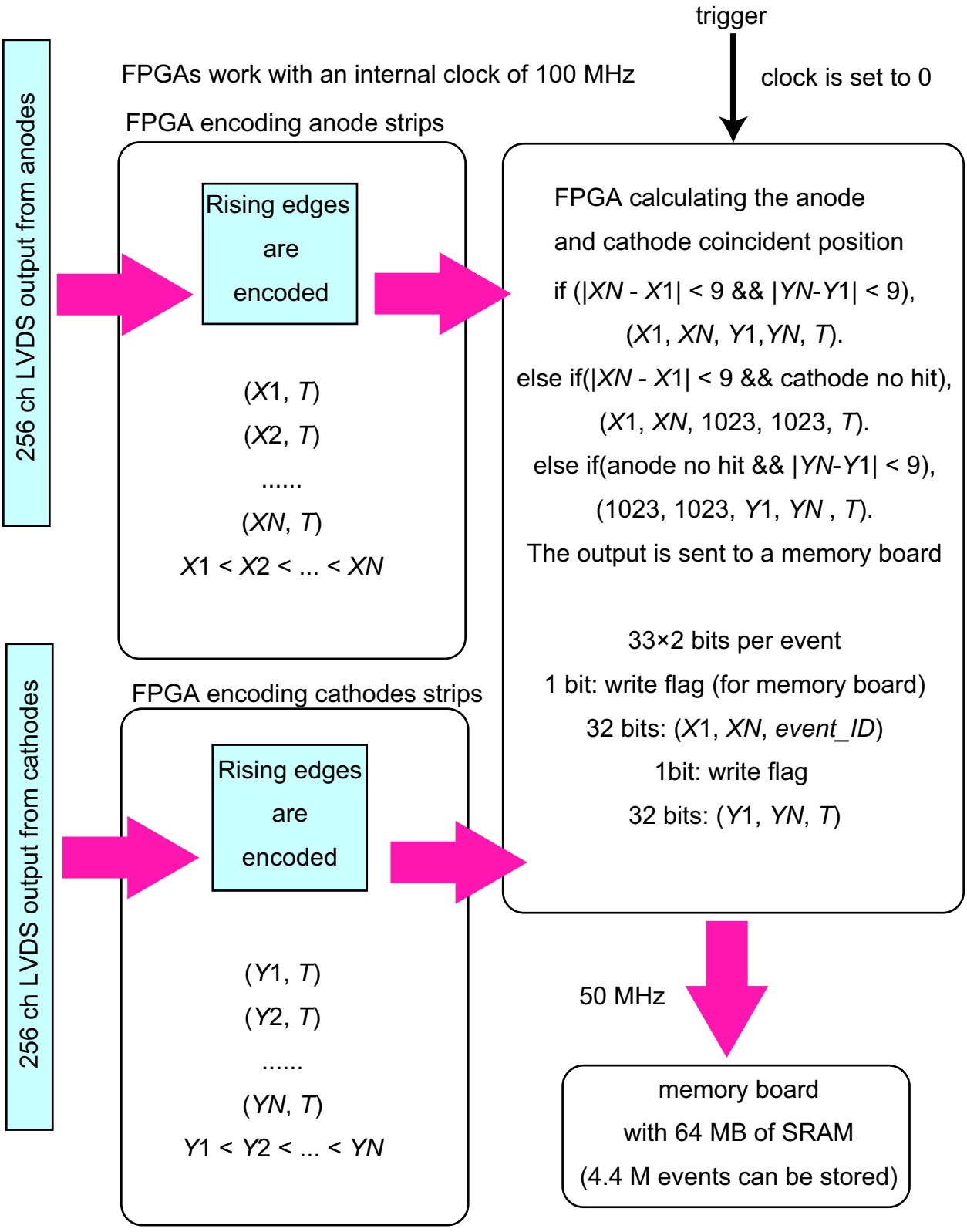

Figure 4.11: A block diagram of a new position encoding system for use of the micro-TPC. The idea of the new system is similar to mode-II.

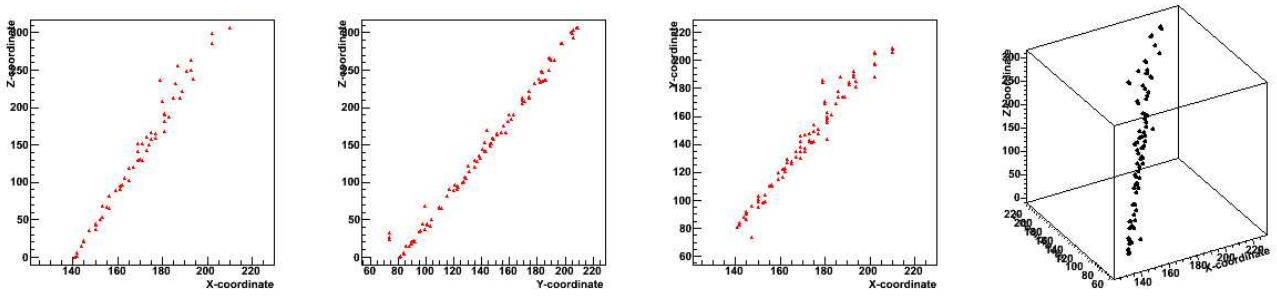

(a) All events are used.

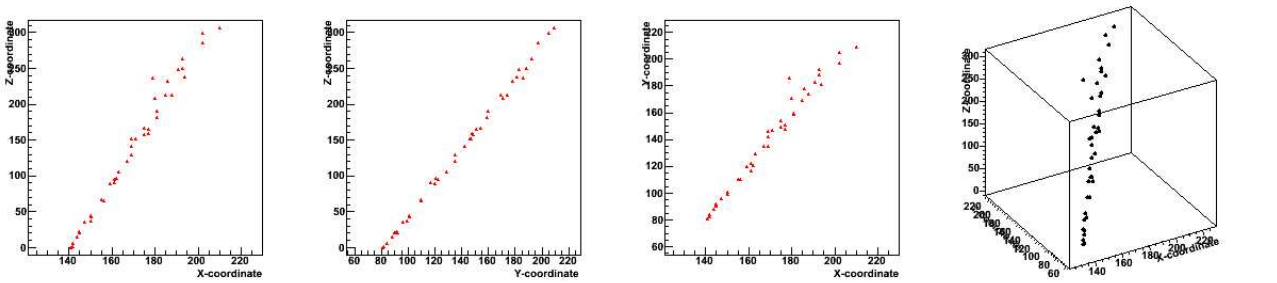

(b) Hits from the anodes and cathodes only when they coincide in a clock interval are used.

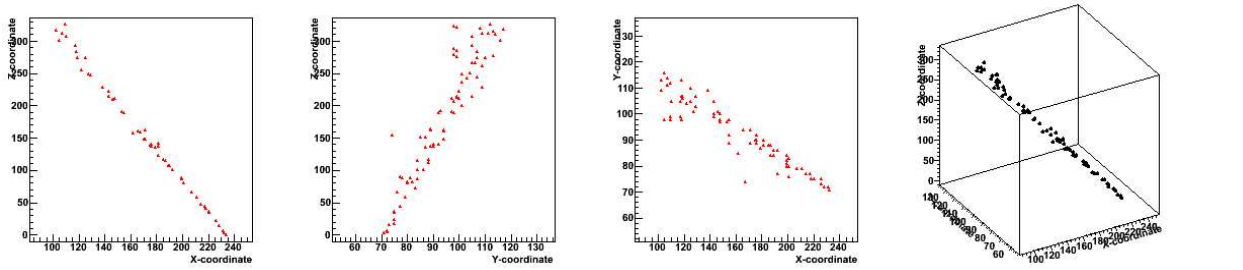

(c) All events are used.

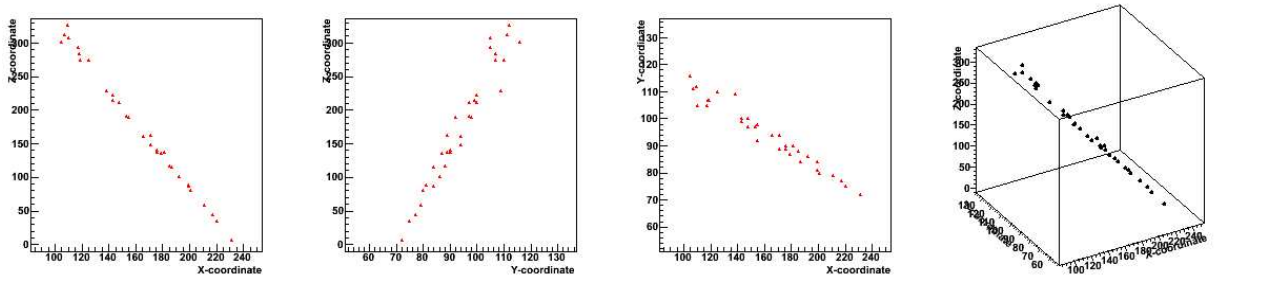

(d) Hits from the anodes and cathodes only when they coincide in a clock interval are used.

Figure 4.12: Tracks of cosmic muons. (a)(c)All hits are plotted in the X-Z and Y-Z plane. In the X-Y plane, hits from the anodes and cathodes when they coincide in two clocks interval are paired together and plotted. (b)(d)Hits from the anodes and cathodes only when they coincide in a clock interval are used (equivalent to TPC mode-I).

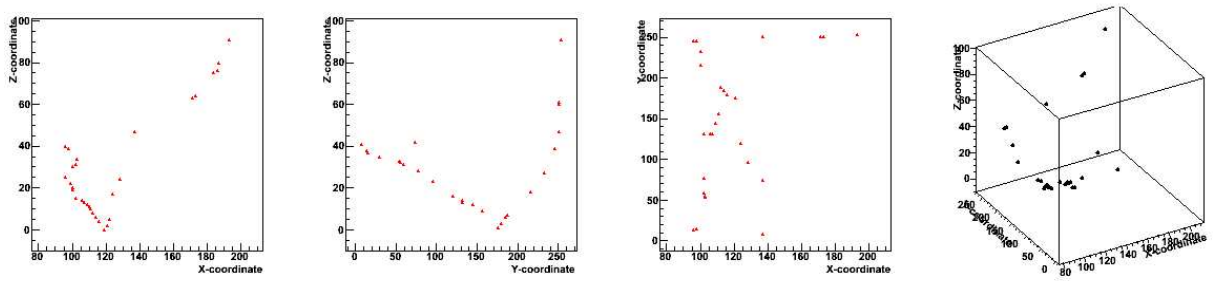

(a) All events are used.

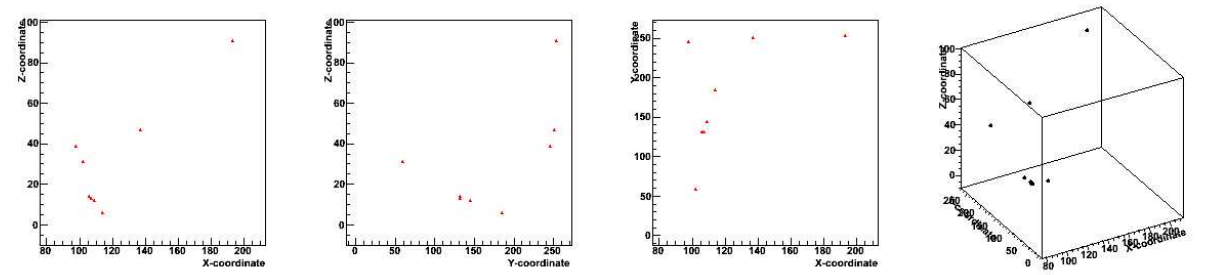

(b) Hits from the anodes and cathodes only when they coincide in a clock interval are used.

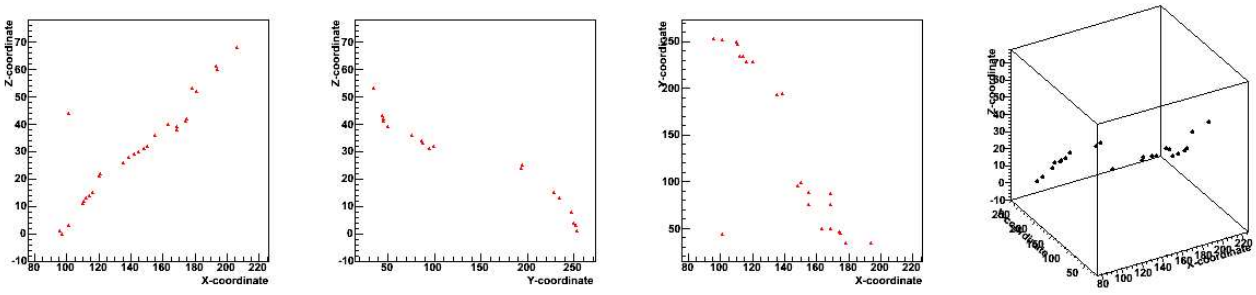

(c) All events are used.

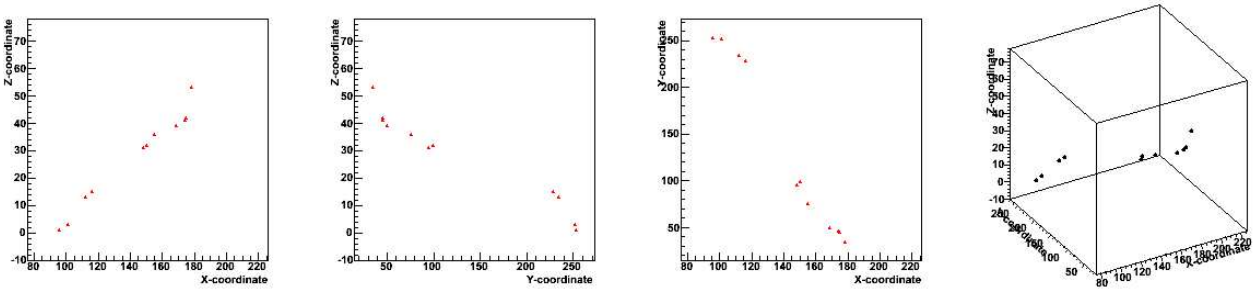

(d) Hits from the anodes and cathodes only when they coincide in a clock interval are used.

Figure 4.13: Tracks of recoil electrons. The detector was irradiated with ^{137}Cs. (a)(c)All hits are plotted in the X-Z and Y-Z plane. In the X-Y plane, hits from the anodes and cathodes when they coincide in two clocks interval are paired together and plotted. (b)(d)Hits from the anodes and cathodes only when they coincide in a clock interval are used (equivalent to TPC mode-I).

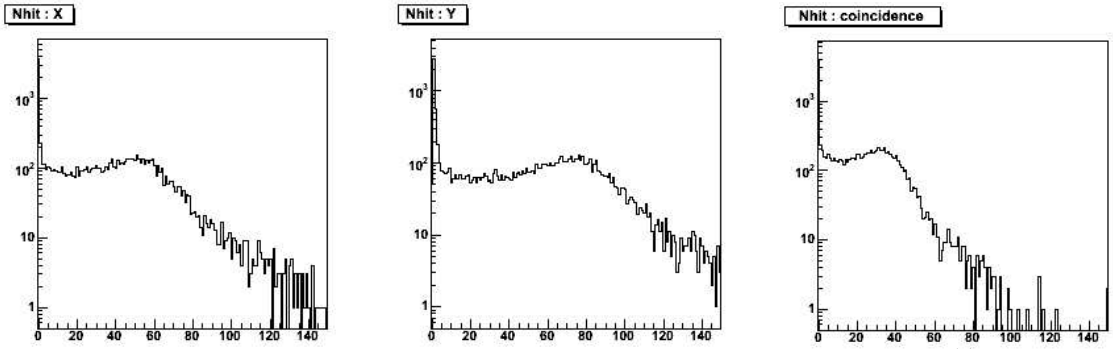

Figure 4.14: Number of hits per cosmic muon track. (a)Hits from the cathodes. (b)Hits from the anodes. (c)Hits from the anodes and the cathodes which coincided in one clocks interval.

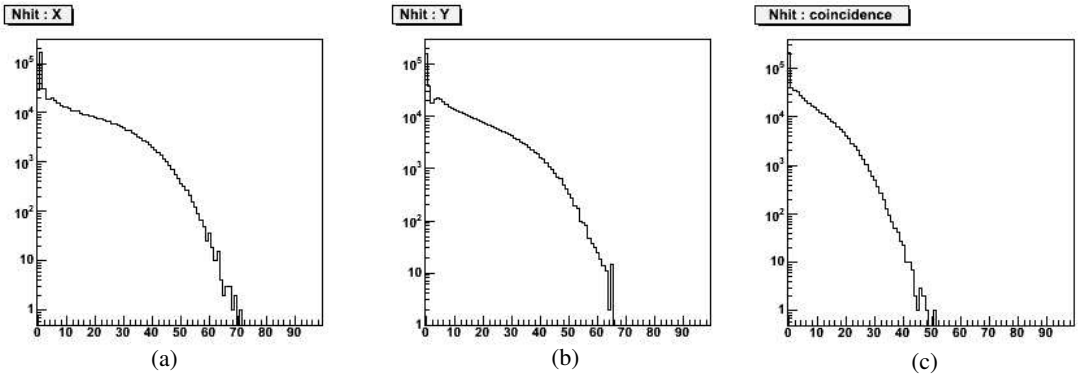

Figure 4.15: Number of hits per recoil electron track. The detector was irradiated with ^{137}Cs. (a)Hits from the cathodes. (b)Hits from the anodes. (c)Hits from the anodes and the cathodes which coincided in one clock interval.

escaped from the detector. The total gas gain was about 5×10^3 (the μ-PIC at 2×10^3, the GEM at 3). This encoding system cannot be triggered and thus an absolute height of the tracks are unknown. The tracks shown in Fig. 4.17 have a feature in at least one of X-Z and Y-Z plane: the widths on the right-hand or left-hand side are larger. When the electron crosses more anode strips than cathode ones, the feature is likely to be found in the X-Z plane (X refers to the strip numbers of the anodes) and vice versa. Then, one can determine which edge is the Compton-scattered point considering the widths in the plane and then in three-dimensional space. In this way, the TPC-modeIII system will enhance the ratio of events with the correct Compton points.

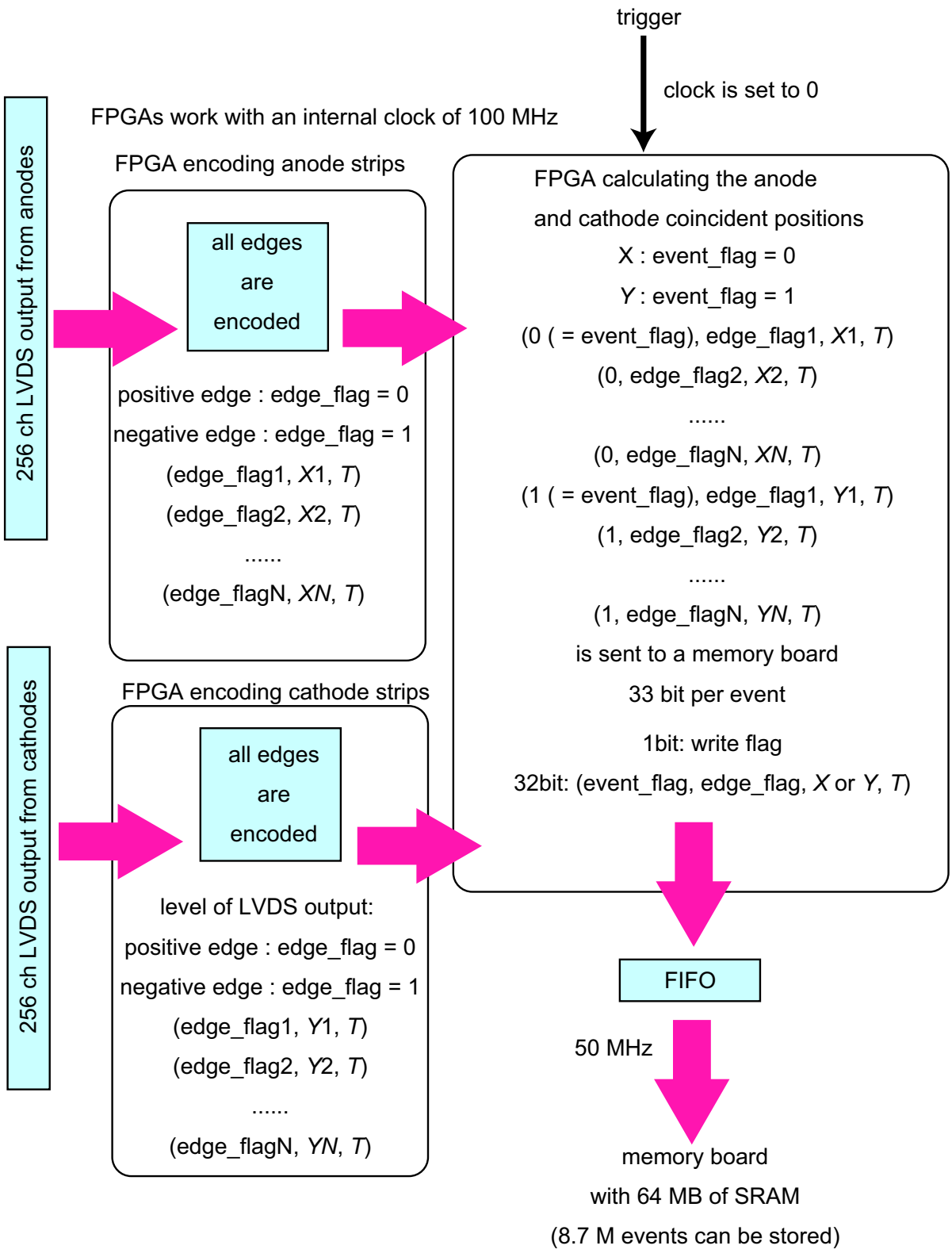

Figure 4.16: A block diagram of a new position encoding system for use of the micro-TPC, TPC-modeIII. The idea of the new system is similar to the mode-III encoding system for use of the X-ray area detector.

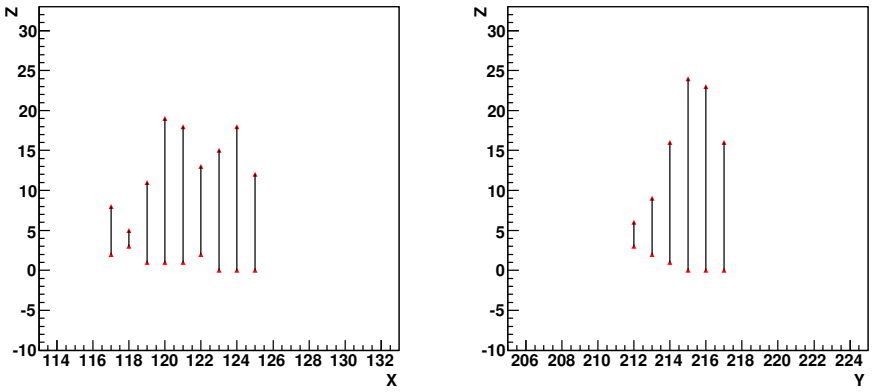

(a)

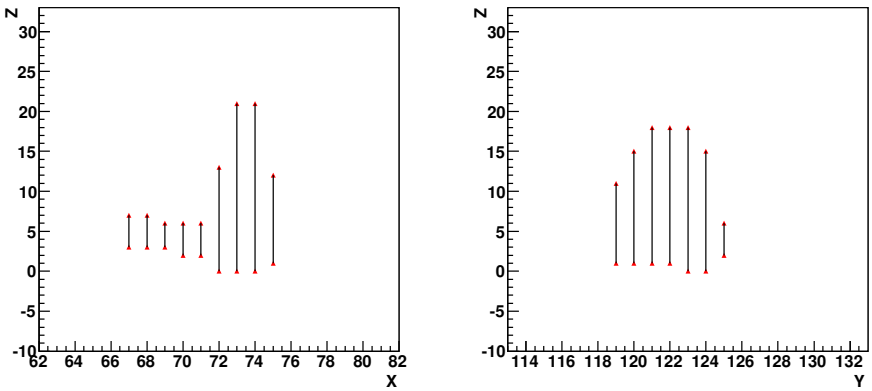

(b)

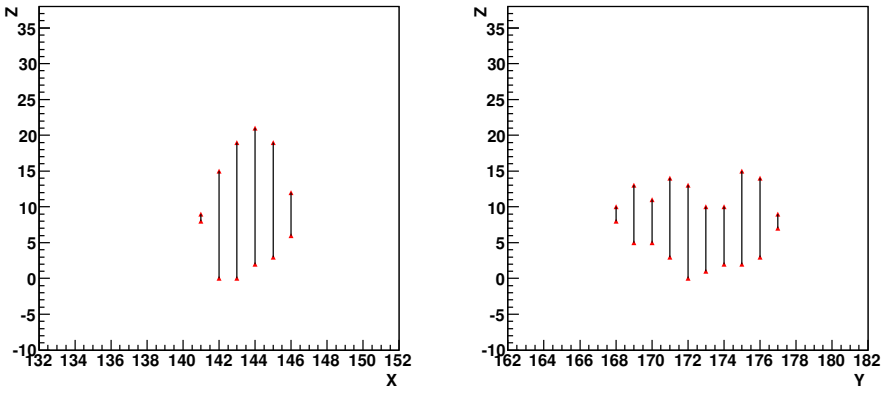

(c)

Figure 4.17: Signals generated by recoil electrons. The detector was irradiated with gamma rays of ^{137}Cs point source (662 keV). Digital output of the ASDs are monitored by the mode-III encoding system. Red-filled triangles displays timings of leading edges and falling edges while lines denotes clocks when the signals exceed the threshold.

Chapter 5

Application to small-angle neutron scattering

In this paper, we mainly discuss the gas detectors for small-angle X-ray scattering. An addition of gas ^{3}He enables for gaseous detectors to detect neutrons. Using a ^{3}He-mixed gas, the μ-PIC detector system functions as a two-dimensional neutron imaging detector. In this chapter, we will briefly summarize motivations for developing the two-dimensional thermal neutron imaging detector and then refer to the first observation of thermal-neutron scattering using the μ-PIC at JRR-3, Japan.

5.1 Small-angle neutron scattering (SANS)

Small-angle neutron scattering (SANS) probes structure in samples on almost the same scale as SAXS, 1 nm to 1 μm scale. Since X-rays interact with electron clouds, their scattering cross section is proportional to an atomic number Z. On the other hand, the neutrons interact with nuclei and thus their scattering cross section is totally different from X-rays. SANS probes the distributions of nucleus in samples while SAXS probes the distributions of electron clouds there. Therefore, they are complementary to each other and provide useful information about structure determination.

Table 5.1 shows the scattering lengths and cross sections for various elements. It should be noted that most of the neutron scattering cross sections shown in Tab. 5.1 have the same scale though their atomic numbers vary in the wide range. Since neutrons are uncharged, they interact much more strongly with the atomic nuclei rather than the electrons. Thus, neutron scattering is suitable to observe the positions of light atoms with few electrons. In the case of SAXS, it is hard to separate scattering from heavy elements and hydrogen because the X-rays interact weakly with light atoms.

The key feature of the neutron scattering is that the cross section of hydrogen is distinct from that of deuterium. Because the chemical properties of hydrogen and deuterium are almost the same, deuterium can be easily exchanged with hydrogen and the resultant sample maintains the original chemical property. Their differential scatter is applied to the technique of contrast variation that is useful for structure determination of materials dissolved in water. Exchanging a part of H_2O with D_2O in a solvent at certain ratios of H_2O to D_2O, the scatter length density from a component of the solute can be the same as that of the solvent. After subtracting the solution scattering from the solvent scattering, components of which scattering length density differ from that of the solvent are observed. In addition, neutrons have magnetic moments and thus they can probe magnetic structure in samples.

As mentioned in section 1.2, the size of 1-100 nm corresponds to the angular region up to $2\theta = 0.8 - 8$ degrees at wavelength $\lambda = 1.54$ Å. Therefore, a sample is irradiated with thermal neutrons with wavelength of Å scale to observe SANS.

Table 5.1: Neutron scattering lengths and cross sections [36]. b_c, b_i, σ_c, σ_i and σ_a represent a coherent scattering length, an incoherent scattering length, a coherent cross section, an incoherent cross section, and an absorption cross section, respectively.

Element	b_c [10^{-13}cm]	b_i [10^{-13}cm]	σ_c [10^{-24}cm^2]	σ_i [10^{-24}cm^2]	σ_a [10^{-24}cm^2]
^{1}**H**	-3.739	25.278	1.757	80.30	0.333
^{2}**H(D)**	6.671	4.04	5.592	2.05	0.000
^{12}**C**	6.646	0	5.550	0.001	0.003
^{14}**N**	9.36	2.0	11.01	0.50	1.90
^{16}**O**	5.803	0	4.232	0.000	0.000
^{19}**F**	5.654	0	4.232	0.001	0.000
^{23}**Na**	3.63	3.59	1.66	1.62	0.530

Now neutrons generated by nuclear fission reactors are mainly used for SANS experiments. Due to absence of fine converging neutron guides, the reactor-based sources produce much lower-intensity flux in comparison with synchrotron sources. Thus, samples irradiating with the reactor-based sources must be large. This is a serious disadvantage to some kinds of samples such as biological materials.

Another neutron sources available are high-energy particle accelerators developed recently. A proton accelerator, J-PARC in Japan, has neutron beamlines where the world highest intensity pulsed neutron will be produced. The estimate of time-integrated intensity and peak intensity with 1 meV neutron is roughly 10^{14} n/cm^2/s/sr/eV and 10^{16} n/cm^2/s/pulse/sr/eV at 1 MW. A repetition rate is 25 Hz [37]. To conduct high-intensity SANS, an area detector working in high-counting rate environments is desired. The pulsed neutron source produces neutrons with a certain range of energy. The energy of the neutrons is measured by Time-of-flight (TOF) on a scale of μs. Therefore, a counting-type area detector with the time resolution of several μs allows one to obtain wavelength dependence of scattering patterns.

Other requests to the detector is low sensitivity to gamma-rays which could be background, and a wide dynamic-range. IPs and MWPCs widely used for SANS have a narrow dynamic range of up to 10^4. A detector consisting of scintillators located in the middle of the detection area surrounded by MWPCs has the widest dynamic range of 10^6. Similar to SAXS measurements, wider dynamic range is required for high-precision experiments. Counting-type detectors are superior to integrated-type ones in terms of a dynamic range because counting-type detectors are free from noises proportional to an integration time. Since the high-energy particle accelerators produces a gamma-ray background, an ability to discriminate against gamma-rays is important. Our goal is to achieve a dynamic range of more than 10^7 and thus sensitivity to gamma-rays must be less than 10^{-6} sensitivity to neutrons.

5.2 Neutron detector based on μ-PIC

5.2.1 ^{3}He(n, p) Reaction

The ^{3}He is used as a detection medium for thermal and thermal neutrons. A ^{3}He(n, p) reaction converts a neutron to detectable particles. The reaction may be written

$$^{3}_{2}\mathrm{He} + ^{1}_{0}\mathrm{n} \rightarrow ^{3}_{1}\mathrm{H} + ^{1}_{1}\mathrm{p}$$

$$Q\text{-value} = 0.764 \ \mathrm{MeV}$$

The Q-value of 764 keV is converted to kinematic energies of reaction products oppositely directed.

$$E_{\mathrm{p}} = 0.573\,\mathrm{MeV}$$

$$E_{^3\mathrm{He}} = 0.191\,\mathrm{MeV}$$

The neutron cross section with a wavelength of 1.8 Å is 5333 barn, and its value falls off with a $1/\lambda$ dependence. Figure 5.1 shows an energy deposit along the proton and triton tracks in 1 atm Ar-C_2H_6-^{3}He (>99 : 10 : <1) mixture gas. The values were calculated by GEANT4 (ver 5.0 patch-01) [38]. The conversions of 25 meV-thermal neutrons were assumed. The proton have a longer track length so that one can separate tracks of two reaction-products and derive the conversion point. In the case of a gas with a bigger ratio of ^{3}He, the track length is longer because $\mathrm{d}E/\mathrm{d}x$ is proportional to atomic number Z.

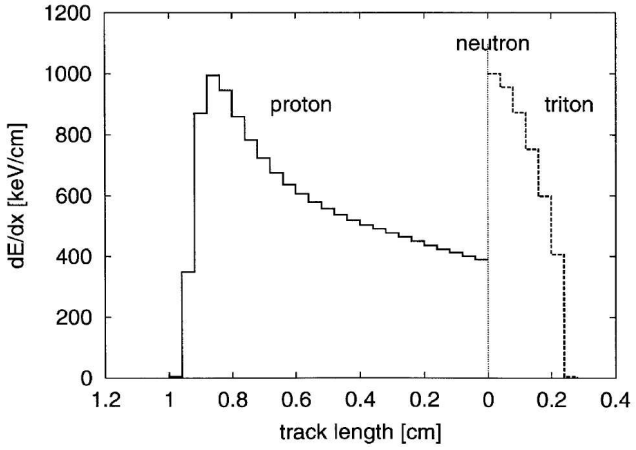

Figure 5.1: Energy deposit along the proton and triton tracks in 1 atm Ar-C_2H_6-^{3}He (>99 : 10 : <1) mixutre gas. The values were calculated by GEANT4 (ver 5.0 patch-01) [38].

5.2.2 Advantage of neutron detector based on μ-PIC

The area detector based on the μ-PIC has been developed for purpose of practical use at third-generation synchrotron radiation sources. The detector system suitable for high-counting rate environments has being developed and is expected to be applied to high-counting rate SANS.

Considering the requirements for pulsed neutron sources, the μ-PIC detector is suitable because of the fine time resolution of 10 ns for incoming particles. Moreover, the μ-PIC is free from dead time if one prepares a large memory to store data from the position encoder. Data obtained by integrated-type area detectors cannot be combined with TOF information. The μ-PIC detector has shown the wide-dynamic range of the solute scattering using the third-synchrotron radiation source.

The energy of the gamma-rays, which are found with neutrons, is transferred to recoil electrons through Compton-scattering. $\mathrm{d}E/\mathrm{d}x$ of the recoil electrons is small and thus their track lengths are long. On contrary, $\mathrm{d}E/\mathrm{d}x$ of protons and tritium is quite large and their track lengths are short. Since one can measure three-dimensional tracks of charged particles using the position encoding module, it is easy to separate signals generated by the neutrons and background. Using the mode-III encoding system described in section 3.5, one can also measure pulse widths and obtain an approximate value of $\mathrm{d}E/\mathrm{d}x$. It could be a strong background rejection unique to a detector system based on a TPC.

A position resolution of less than 1 mm is desired for neutron detectors while currently available neutron detectors have a position resolution of up to a few mm. Now we are considering two ways

to enhance the position resolution of the neutron detector based on the μ-PIC . One way is to raise a gas pressure to about 10 atm and then the short track lengths of the reaction products lead to a better position resolution. Other way is to obtain fine tracks of the reaction products at a moderate-gas pressure using the mode-III system. Since a detection efficiency of at least 20 - 30 % is required, there is a need of a thick gas layer in this case. The detector is aiming at small-angle scattering measurements. Thus it is unnecessary to take into account parallax even if the gas layer is thick and heights of the conversion points are unknown. With the approximate value of $\mathrm{d}E/\mathrm{d}x$, one could determine directions of the reaction products, which are oppositely directed. Since their kinematic energies are known, the conversion point can be calculated.

5.3 Overview on study of neutron time-resolved imaging

We studied a TPC based on the μ-PIC for a time-resolved neutron imaging detector [39]. The TPC was irradiated with neutrons produced by the fission decay of ^{252}Cf (about 2 MBq). Since gamma-rays emitted from the decay were detected by Yttrium Aluminum Perovskite (YAP) scintillator for the neutron trigger, one can measure the absolute height of the conversion points. In addition, every 32-ch analog outputs from the ASDs were summed and sampled by a 100 MHz flash ADC (FADC) in spite of measuring the widths of the digital output. Referring to the waveform of the analog output, one can observe the Bragg curves and deduce the directions of the reaction products. This method solves the parallax problem. However, the neutron beam does not have the simultaneous signals and thus this method is unavailable.

Now we will briefly summarize the performances of the time-resolved neutron imaging detector. In this experiment, the vessel containing the TPC with a detection volume of 10 cm $\times$ 10 cm $\times$ 10 cm was filled with an Ar-CF_4-^{3}He (78:20:2) mixture gas at 1.1 atm. We used a ^{252}Cf source mainly emitting fast neutrons. Polyethylene blocks were arranged next to the source and thermalizes the fast neutrons. We chose a CF_4 having a small cross section of fast neutrons in elastic scattering. The TPC mode-I position encoding system shown in Fig. 2.19 was applied to this experiment. Figure 5.2 shows tracks of charged particles generated by ^{3}He(n, p) reactions. The double-peaked Bragg curve can be clearly seen in every event. Through this measurement, we proved that the μ-PIC has an ability to detect tracks of the reaction products and determine the conversion points. Instead of the TPC mode-I encoding system, we will use the mode-III encoding system, which provides the pulse widths. The mode-III system provides approximate pulse heights without the FADC and continuous measurements. We are planning to conduct neutron scattering experiment with the mode-III system.

5.4 Thermal neutron imaging

To prove an ability to thermal neutron imaging, we conducted SANS experiments at NOP beamline, JRR-3, Japan. Since a detector for neutron imaging was under construction at that time, we used the detector for X-ray imaging. Thus, the gas layer of 4 mm is so thin that most reaction products penetrate the detection volume. Since the vessel containing the detector was designed to withstand a gas pressure of about 1 atm, we filled a ^{3}He-Ar-C_2H_6 (11.1 : 80.0 : 8.9) mixed gas with a pressure of 1.08 atm. The low gas gain of $< 10^3$ was applied in order to discriminate against the gamma-rays. We removed the GEM because the μ-PIC maintains stable amplifications at a gas gain of 10^3. To enhance the intensity, we removed a slit and a monochrometer in front of a sample. In consequence, the beam had a broad wavelength distribution. The thermal-neutron beam had an average wavelength of 7.6 Å. The counting rate was 5.9×10^3 cps and the beam size was about ϕ25 mm at the detection area without a collimator. The mode-II position encoding system was employed because the mode-III system had not been suggested at that time. The possibility of the conversions in the detection volume was 2.96×10^{-2} at a wavelength of 7.6 Å. An actual counting

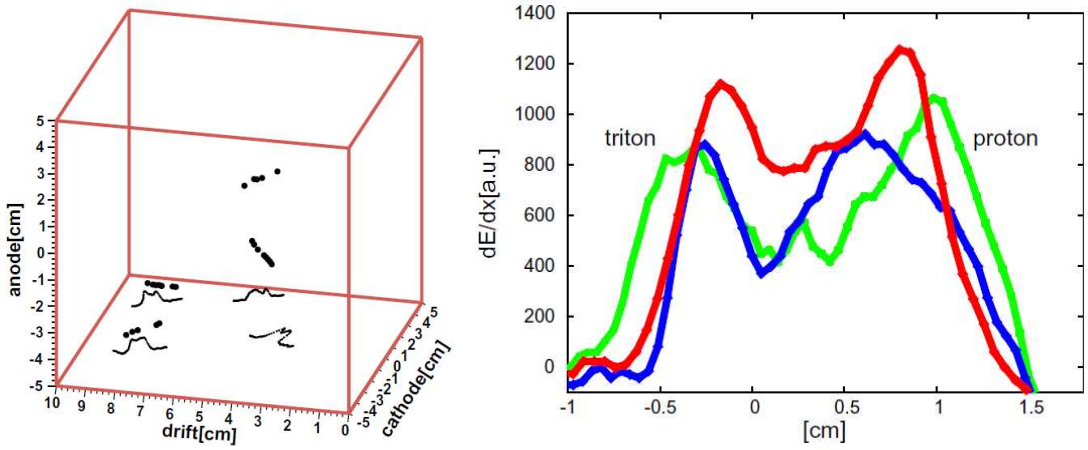

(a) Three-dimensional tracks of tritons and protons and their waveforms.

(b) Waveform of protons and tritons.

Figure 5.2: Tracks of charged particles generated by ^{3}He(n, p) reactions.

rate was found to be smaller by two orders of magnitude than this value. Because most of the reaction products penetrate the gas layer, they deposit a small fraction of its initial energies within the gas. Therefore, reaction products which happen to deposit most of their energy in the gas volume might be detected.

Figure 5.3(b)(c) display images of a cadmium test chart irradiated with a large absorption cross section. The exposure time was 7.4×10^4 seconds. To enhance a signal-to-noise ratio, events with more than 5 hits (32 bits $\times$ 5) were used. The image yielded by an integration of the reaction products tracks shown in Fig. 5.3(b) broadens and the structure of the test chart is smeared due to the bad position resolution. The track length of the reaction products including penetrating ones ranges from approximately 2 mm to 7 mm. Some of the products penetrate the thin detection region and lead to the wide range of the track length. Each bright line in Fig. 5.3(b) corresponds to a noisy ASD channel. The low intensity and detection efficiency emphasis the contribution of the noise. The image yielded by an integration of the averaged positions of the reaction products tracks is shown in Fig. 5.3(c). The noisy ASD channels were removed and then the averaged positions of the tracks were calculated. Since the tracks of two reaction products are on the same line, the difference between the conversion point and the averaged position must be smaller than that between the conversion point and hits close to the end of the tracks. Thus, the position resolution was drastically improved.

5.4.1 Position resolution

We conducted the knife edge test to evaluate the position resolution of the image yield by the integration of the averaged positions. Figure 5.4 shows an image of a cadmium slit with a 8-mm hole. The exposure time was 4.6×10^4 seconds. Since a uniform neutron beam with a large-cross section was unavailable, we used a region where the beam intensity is approximately uniform, shown in the sector in Fig. 5.4(a). Figure 5.4(b) shows a projection along the edge of the hole fitted by $a_1 + a_2 \mathrm{erf}((x - a_3)/(\sqrt{2}\sigma))$. The parameter σ was 0.956 mm, corresponding to the position resolution. Irradiating with a uniform beam, the position resolution would be better than this value. The parameter a_3 was 3.992 mm, which agrees with the radius of the hole. Neutrons scattered by the vessel walls and the μ-PIC are supposed to produce the long tail in Fig. 5.4(b). Therefore, the background estimation and reduction are important to enhance a wide-dynamic range. A thicker

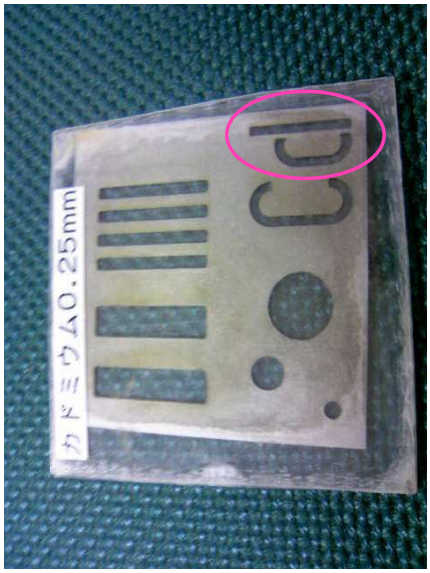

(a) Circled region was irradiated with a neutron beam.

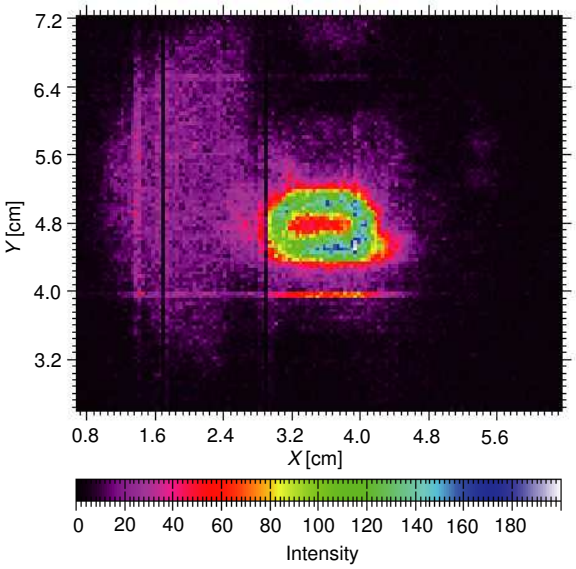

(b) Integration of reaction products tracks

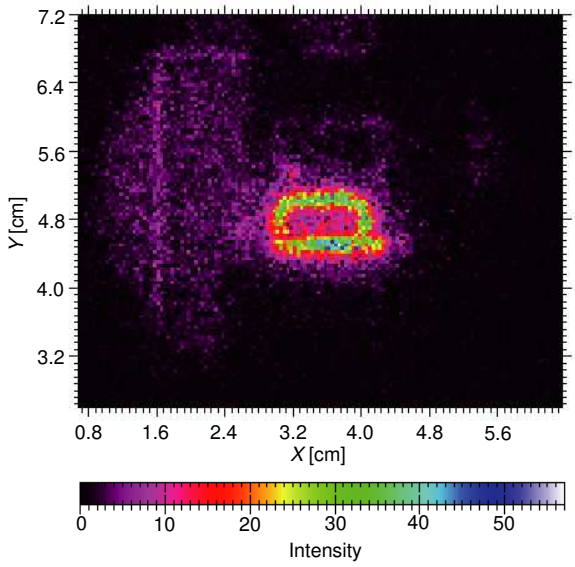

(c) Integration of the averaged positions of reaction products tracks

Figure 5.3: Images of a cadmium test chart irradiated with thermal neutrons (7.6 Å).

gas layer avoids penetration of the reaction products and the mode-III encoding system would provide more accurate conversion points. With these improvements the position resolution could be enhanced.

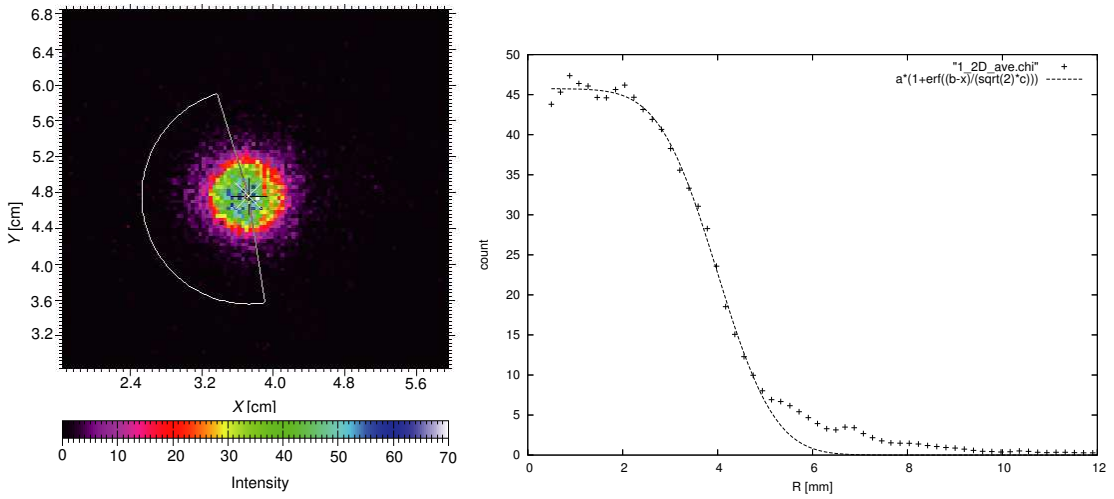

(a) Image of a cadmium slit; a 8-mm hole is arranged.

(b) A region defined by a sector shown in (a) is integrated.

Figure 5.4: Images of a cadmium test chart irradiated with thermal neutrons (7.6 Å). The edge of the hole is at $R = 4$ [mm].

5.4.2 Bragg curve

We observed a diffraction pattern from a 4-mm thick $F_{12}H_{20}$ crystal, shown in Fig. 5.5. The distance between the sample and the drift plane 4.5 mm in front of the μ-PIC was 2.3×10^2 mm. The exposure time was 1.8×10^5 seconds. A black line refers to a diffraction curve observed by the μ-PIC ; a red line to one observed by a neutron scintillator (ZnS/^{6}LiF) as a reference. The positions of the first Bragg peak observed by the μ-PIC and the scintillator agree. According to Fig. 5.5, counts per pixel are less than 1 at the Bragg peak due to the low-detection efficiency. It leads to the bad signal-to-noise ratio and thus the Bragg peak observed by the μ-PIC was less clear. A detector with a thicker-gas layer could improve the signal-to-noise ratio and provide a clear Bragg peak.

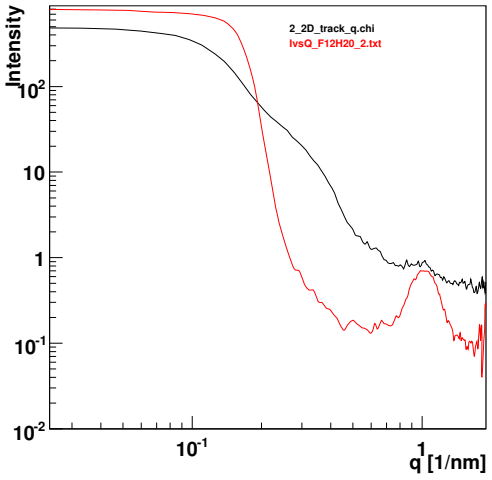

Figure 5.5: Diffraction curve of $F_{12}H_{20}$. A black line refers to a diffraction curve observed by the μ-PIC ; a red line to one observed by a neutron scintillator (ZnS/^{6}LiF) as a reference. The intensity of the reference is an arbitrary unit. The curve measured by the μ-PIC shows counts per pixel. A Bragg peak of q =1.02 nm^{-1} can be recognized.

Chapter 6

Summary

We have successfully shown the advantages of photon-counting type detectors to SAXS measurements, especially the wide dynamic range, using the gaseous area detector based on the μ-PIC .

Since the μ-PIC has the strip structure, the positions of incident X-rays are reconstructed by the position encoding module. The mode-I position encoding system is the oldest one: it records hits from the anodes and cathodes only when they coincide in a clock interval. Using the mode-I position encoding system, the μ-PIC detector had showed the fine performances for time-resolved experiments and the CRP method. However, the performance of the detector, especially of the position encoding system, was insufficient to achieve high-precision SAXS measurements in terms of linearity, uniformity, accidental coincidence, and counting loss. The solution scattering curves of Apo-Ferritin measured by the mode-I system and the IP were compared. Then, the positions of the valleys and the peaks did not agree. Therefore, we developed the new position encoding systems, mode-II and mode-III. The performance of the improved system was studied at the RIKEN structural biology beamline (BL45XU-SAXS station) at SPring-8, Japan.

The mode-II system recording all hits from anodes and cathodes solved the counting-loss problem due to the propagation delay at the digital outputs of the ASDs. Instead of integrating all hits, we used the averaged positions of them to yield two-dimensional images. Then, the effect of the non-uniformity of the gas gain and the ASD gain were eliminated and the images became quite uniform. When the arrival time difference between two X-rays is less than 200 ns, they are likely to pile up and thus removed in the off-line analysis. This cut, called a pile-up cut, was used to remove the ghost images produced by hits from the anodes and the cathodes when they accidentally coincide. The resultant scattering curve of Apo-Ferritin was consistent with that measured by the IP. The important value of gyration obtained by the μ-PIC was 5.320 ± 0.031 nm while that obtained by the IP was 5.357 ± 0.006. Considering the errors, these two values seem consistent. This result proves that the curves in the very small-angle region measured by them agree with each other.

The dynamic range of the μ-PIC detector was investigated using the solution scattering from SiO_2 nano particles. In theory, the scattering curve of the particles approximated by a solid sphere follows the power law of q^{-4}. The intensity clearly followed the power law, and the dynamic range of the solute scatterings was widened to $> 10^6$. This is the widest linearity in solution scattering observed by X-ray area detectors. This wide dynamic range was attained because the detector is free from the internal background and the statistical uncertainty is dominant. In this way, the μ-PIC detector proved that it has the key features of the photon-counting detectors. The detector will provide high-precision measurements and more accurate structure determination. Using the detector, structure of materials containing light elements would be revealed by SAXS measurements. Many experiments carried out on high-flux and high-brilliance third generation synchrotron X-ray sources have been limited by the performance of imaging detectors. A new photon-counting imaging device such as the μ-PIC will enhance some of those experiments.

To perform more accurate position calculations, the mode-III position system was designed.

The system can measure pulse widths of the hits and allows one to find a centroid of the charge distribution. The position resolution was improved using mode-III. The position resolution of $\sigma = 93.6$ μm was determined by holes with 500 μm diameter. We also used a diffraction pattern of chicken collagen to evaluate mode-III and succeeded in separating the first peak. The position resolution of the peak recorded by the mode-III was compared with that by the mode-II system. Then, it became two times better when the mode-III system was used. The diffraction curve of the collagen was compared with that observed by an imaging plate for reference, and these two curves agreed well. The pixel pitch of the IP was 100 μm. The solution scattering from SiO_2 nano particles was also observed by these detectors. The resultant scattering curves agreed well.

There is a need for improvements in terms of the gain stability, the aging behavior in high-counting rate environment and the DAR. In principle, gaseous detectors including the μ-PIC detector have the gain variation, which is especially large within a time-frame of several hours after a high voltage is applied. At the current gain flactuation of the μ-PIC detector and the common threshold applied to the ASDs, the detection efficiency of charges generated by the X-rays is not 100% and thus is effected by the gain fluctuation. The electronic noise reduction is necessary to lower the threshold level and then the the detection efficiency for the charges will be 100%. Therefore, we are developing a new extension board and will place readout circuits closer to the μ-PIC . The noise reduction will also compensate the small drop in the gain due to the aging behavior. Another solution to the aging is to remove the ethane gas and use another kind of a quencher gas such as CO_2.

Our goal is to operate the μ-PIC under the high-counting rates where the IPs are used. Using mode-II, we successfully measured the solution scattering in such an environment and achieved the dynamic range of $> 10^6$. However, mode-III is more complex and has achieved the DAR of only 2 MHz. For use in the high-counting rate environment, the renewal of the system is required.

These mode-II and -III position encoding systems were applied to the Compton camera consisting of a TPC with readout of the u-PIC and a scintillation camera. Using mode-I, the camera had successfully produced two-dimensional images of gamma-ray sources. However, this system also had the counting loss problem similar to the X-ray area detector, because hits from the anodes and the cathodes were recorded when they coincide in a clock interval. Thus, we developed TPC-modeII based on mode-II that allows one to record all hits. As consequent, the number of hits was doubled and the fine three-dimensional tracks of muons and recoil electrons were obtained. Now the angular resolution of SPD is much worse than ARM because of the multiple-scattering of the recoil electrons. Thus, the more precise tracks would be able to determine the initial momentum vectors of the recoil electrons more precisely.

Furthermore, the widths of the hits were measured by the TPC-modeIII encoding system. The key concept of TPC-modeIII is the same as that of mode-III. Then, we showed that Compton points would be determined by the widths and thereby $\mathrm{d}E/\mathrm{d}x$. Another main reason for deteriorating SPD is the incorrect Compton points determined by only the positions of the hits. The GEANT4 simulation shown that the criterion gives 60% recoil electrons correct directions. It is slightly better than a random selection. Therefore, TPC-modeIII will improve the situation drastically.

Using mode-II, we also showed that the area detector can detect thermal neutron scattering. It was the first observation of the thermal neutrons using the μ-PIC detector and was conducted SANS experiments at NOP beamline, JRR-3, Japan. We obtained the two-dimensional image of the test chart and position resolution of 1 mm using the knife edge test. Currently available neutron imaging detectors have a position resolution of up to a few mm. Thus the μ-PIC detector would provide high-resolution measurements. The first Bragg curve of the $F_{12}H_{20}$ crystal was observed at the correct position. In this way, we proved that the μ-PIC detector functioned as a two-dimensional neutron imaging detector. The pulsed neutron sources produced by high-energy particle accelerators need detectors with the time resolution of several μs to measure the energy of the neutrons. The μ-PIC detector with time resolution of 10 ns is promising for the application. We are developing a detector with a thicker gas layer of 5 cm and will operate it at a higher pressure

of about 2 atm. Then, the detection efficiency of the thermal neutrons would be 20-30 % that is sufficient for the practical use. The detector with the thicker gas layer will provide the whole tracks of the neutrons. Moreover, the track length will be short at the high pressure. The thick gas layer and the short tracks are expected to improve the position resolution to a few 100 μm.

Bibliography

[1] Y. Amemiya and Y. Shinohara, *Journal of the Japanese Society for Synchrotron Radiation Research*, **19** (2006) 338.

[2] L. A. Feigin and D. I. Svergun, *Structure Analysis by Small-Angle X-ray and Neutron Scattering*, Plenum Press, New York(1987).

[3] G. C. Smith, *J. Synchrotron Rad.* **13** (2006) 172.

[4] R. P. Phizackerley, *Nucl. Instr. and Meth. A* **246** (1986) 579.

[5] Y. Amemiya, *J. Synchrotron Rad.* **2** (1995) 13.

[6] Y. Amemiya et al., *Rev. Sci. Instrum.* **66** (1995) 2290.

[7] J. Drenth, *Principles of Protein X-ray Crystallography*, Springer-Verlag, New York(1994).

[8] S. M. Gruner, et al., *Rev. Sci. Instrum.* **73** (2002) 2815.

[9] A. Oed, *Nucl. Instr. and Meth. A* **263** (1988) 351.

[10] T. Tanimori et al., *Nucl. Instr. and Meth. A* **381** (1996) 280.

[11] Y. Giomataris et al., *Nucl. Instr. and Meth. A* **376** (1996) 29.

[12] R. A. Lewis et al., *Nucl. Instr. and Meth. A* **392** (1997) 32.

[13] A. Berry et al., *Nucl. Instr. and Meth. A* **513** (2003) 260.

[14] Ch. Broennimann et al., *J. Synchrotron Rad.* **13** (2006) 120.

[15] G. Hülsen, Ph. D. Thesis, University of Erlangen - Nürnberg (2005).

[16] C. J. Hall et al., *Nucl. Phys. B* (Proc. Suppl.) **44** (1995) 242.

[17] H. Toyokawa et al., *Nucl. Instr. and Meth. A* **467-468** (2001) 1144.

[18] H. Sakurai et al., *Nucl. Instr. and Meth. A* **374** (1996) 341.

[19] F. Sauli, *Nucl. Instr. and Meth. A* **386** (1997) 531.

[20] A. Ochi et al., *Nucl. Instr. and Meth. A* **471** (2001) 264.

[21] A. Ochi et al., *Nucl. Instr. and Meth. A* **478** (2002) 196.

[22] T. Nagayoshi et al., *Nucl. Instr. and Meth. A* **513** (2003) 277.

[23] T. Nagayoshi et al., *Nucl. Instr. and Meth. A* **525** (2004) 20.

[24] M. Bouianov et al., *Nucl. Instr. and Meth. A* **540** (2005) 266.

[25] A. Takada., Ph. D. Thesis, Kyoto Univerity (2007).

[26] A. Takeda et al., *IEEE Trans. Nucl. Sci.* **NS-51** (2004) 2140.

[27] R. Orito et al., *IEEE Trans. Nucl. Sci.* **51** Issue 4, Part1 (2004) 1337.

[28] H. Kubo et al., *Nuclear Science Symposium Conference Record 2005 IEEE* **1** (2005) 371.

[29] A. Hammersley, http://www.esrf.eu/computing/scientific/FIT2D

[30] N. Yagi et al., *J. Synchrotron Rad.* **11** (2004) 456.

[31] T. Tanimori et al., *J. Synchrotron Rad.* **5** (1998) 256.

[32] A. Ochi et al., *Nucl. Instr. and Meth. A* **467-468** (2001) 1148.

[33] V. Schoenfelder et al., Astroph. J. Suppl. Series. 86 (1993) 657.

[34] R. Orito et al., *Nucl. Instr. and Meth. A* **513** (2003) 408.

[35] T. Tanimori et al., *New Astron. Rev.* **517** (2004) 241.

[36] *NIST Center for Neutron Research* http://www.ncnr.nist.gov/

[37] *J-PARC Materials and Life Science Facility* http://j-parc.jp/MatLife/ja/index.html

[38] K. Miuchi et al., *Nucl. Instr. and Meth. A* **517** (2004) 219.

[39] T. Tanimori et al., *Nucl. Instr. and Meth. A* **529** (2004) 373.

Acknowledgements

The work was conducted with lots of support given by a large number of people. I am particularly indebted to my supervisor Prof. Dr. T. Tanimori for his guidance, support and valuable discussion. Special thanks to my former colleagues, Dr. K. Tsuchiya and Y. Okada(Tsuchiya) who used to do this work and helped me when I started this work.

I am deeply grateful to the collaborators of this work: Dr. H. Kubo, Dr. K. Miuchi, Dr. S. Kabuki, Dr. J. D. Parker, H. Nishimura, K. Ueno, S. Kurosawa, C. Ida, and M. Takahashi. I also would like to thank other members at my laboratory for their funny talks and creative jokes. Particular thanks to Dr. Parker and C. Ida who helped SAXS measurements at SPring-8. Dr. Parker proofread a part of this paper and gave useful advice. After I graduate, he will do this work in place of me. I am looking forward to see how he improves the detector in the near future. I am grateful to Dr. Kubo who helped improvements on the position encoding module and gave lots of advice on not only this work but lots of other things. VHDL programs for the encoding module were written by ARKUS.Ltd, in Japan.

I thank SPring-8 staff for the operation of SPring-8 and the support for this work. I am particularly indebted to Dr. K. Ito (RIKEN Harima Institute/SPring-8) for lots of support during experiments at SPring-8, valuable advice, and significant discussion. I am also grateful to Dr. M. Takata (RIKEN Harima Institute/SPring-8, JASRI, The University of Tokyo) for giving us valuable advice. I also thank Prof. Hideki Seto (Kyoto University) for his support of SAXS using an X-ray generator. I am very grateful to Prof. Yoshiyuki Amemiya (The University of Tokyo) for significant advice. Our appreciation is extended to RIGAKU co. Ltd for supporting the X-ray generator.

I thank JRR-3 staff, particularly T. Oku for the operation of SPring-8 and the support for this work. I am grateful to Prof. H. Shimizu for valuable advice on SANS experiments.

This work was supported by KEK Renkei, a Grant-in-Aid for the 21st Century COE "Centre for Diversity and Universality in Physics", and a Grant-in-Aid for the Global COE Program "The Next Generation of Physics, Spun from Universality and Emergence"; Grant-in-Aids in Scientific Research of the Ministry of Education, Culture, Sports, Science and Technology (MEXT). The author is supported by Japan Society for the Promotion of Science Research Fellowship for Young Scinentists. The synchrotron radiation experiments were performed at BL45XU in SPring-8 with the approval of the Japan Synchrotron Radiation Research Institute (JASRI) (Proposals No. 2007A1630, 2007B1407, and 2008A1532).